Shocked single crystals studied via nanosecond Laue diffraction and Molecular Dynamics



Matthew J. Suggit

University College

University of Oxford

A thesis submitted for the degree of

Doctor of Philosophy

Michaelmas 2012

For my parents

Acknowledgements

There are a great many people to whom I owe my thanks. First and foremost, I would like to thank my supervisor, Justin Wark, for giving me this opportunity and for his patient guidance in the start of my graduate career. I would like to thank all members, past and present, of the Wark group with whom I have worked. In particular, Andy Higginbotham, for innumerable discussions, help, and encouragement over the last four years, and Giles Kimminau, for taking me along for my first experiment at Janus, which formed the basis for the work in this thesis. A big nod goes to Nigel Park and AWE for funding my research and continuing support.

This work would not have been possible without numerous collaborators. I thank Jim Hawreliak, for his huge contribution to the experimental work described in this thesis, and many others at LLNL; Bruce Remington, Hye-sook Park, Brian Maddox, to name only a few. The staff of the Jupiter Laser Facility. Damien Hicks for his VISAR analysis code. Paula Rosen, John Foster, Steve Rothman, Andy Comley, Nick Bazin, and many others at AWE. Chris Spindloe and the Target Fabrication group at RAL. I would also like to thank Eduardo Bringa for sharing some of his knowledge and for his guidance in the computer simulation work presented. I would like to thank my undergraduate tutors Robin Nicholas and Patrick Baird for sticking with me and putting up with my time spent rowing.

Last and certainly not least, I thank my family and friends. My parents, for being great and providing me with so many opportunities, and Kate, for keeping me sane.

Abstract

Under shock compression it is believed that crystalline materials undergo complex, rapid, micro-structural changes to relieve the large applied shear stresses. The mechanisms involved, such as dislocation flow and deformation twinning, under the generated high strain rates are not fully understood and *in situ* measurements of defects have proven elusive. This work presents the development of a nanosecond x-ray diffraction technique based on the white-light Laue method, and its first use in studying shock compressed copper. Observations of diffuse scattering are interpreted as stress-dependent lattice rotations due to dislocation glide. The results are compared with MD simulations of shocks in copper which are shown not to agree. Simulations of tantalum, shocked along the [001] axis, are demonstrated to undergo deformation twinning. A novel order parameter for identifying twin variants is developed and the deformation twinning mechanism under shock compression is identified.

Contents

Contents **iv**

List of Figures **vii**

Nomenclature **xi**

1 Introduction **1**

1.1 Historical context 1

1.2 Thesis layout and role of the author 4

2 Background Theory **6**

2.1 Crystal structure 6

2.1.1 Lattices 6

2.1.2 Directions and planes 9

2.1.3 The Reciprocal lattice 11

2.1.4 Stress and strain 12

2.1.4.1 Stress 12

2.1.4.2 Strain 14

2.1.5 Elasticity and plasticity 16

2.1.6 Crystal defects 18

2.1.6.1 Dislocations 18

2.1.6.2 Stacking faults 22

2.1.6.3 Twinning 24

2.2 X-ray diffraction 26

2.2.1 Bragg's law 26

2.2.2 The Laue condition 27

2.2.3 Atomic form factor 29

2.2.4 Structure factor 30
2.2.5 Dynamical diffraction 32
2.2.6 Experimental diffraction geometries 34
2.2.6.1 The Laue method 34
2.2.6.2 Powder diffraction 35
2.2.7 The Ewald sphere 35
2.3 Shock waves 36
2.3.1 Rankine-Hugoniot equations 38
2.3.2 The Hugoniot 40
2.3.3 Shock waves in solids 41
2.3.4 Dislocation models 43
2.4 Molecular dynamics simulations 45
2.4.1 Potentials 46
2.4.2 The LAMMPS code 48
2.4.2.1 Centro-symmetry parameter 50
2.4.3 Simulating diffraction from MD 50

3 Nanosecond white-light Laue technique 51
3.1 Background 51
3.2 The JANUS laser 53
3.3 Experimental design and development 54
3.3.1 X-ray source 54
3.3.2 Target design 59
3.3.3 Image plate and filtering 60
3.3.4 Experimental set-up 62
3.4 VISAR 66
3.5 Fitting code 75
3.5.1 Algorithm 79
3.5.2 Simulated diffraction from MD 81

4 *In situ* x-ray diffraction from silicon and copper 84
4.1 X-ray source 84
4.1.1 Spectrum calibration 85
4.1.2 Source optimisation 88
4.1.3 Comparison with an implosion x-ray source 91

4.2 Shocked silicon . . . 93
4.3 Copper . . . 98
4.3.1 Copper target characterisation . . . 100
4.3.2 Drive pressure . . . 101
4.3.3 Diffraction data . . . 102
4.3.4 MD simulations . . . 109
4.3.5 Lattice rotations . . . 112
4.4 Summary . . . 118

5 Twinning in MD simulations of shocked tantalum 119
5.1 Background . . . 119
5.2 Simulations . . . 122
5.2.1 Fourier transform analysis . . . 125
5.2.2 Per atom structure factor . . . 127
5.3 Results . . . 132
5.3.1 Mechanism . . . 134
5.4 Omega diffraction experiments . . . 139
5.5 Conclusions . . . 140

6 Summary and Future work 142
6.1 Summary . . . 142
6.2 Future work . . . 144

Appendix A 146
A.1 Lattice rotation under large strains . . . 146
A.1.1 Single glide . . . 146
A.1.2 Double glide . . . 150

References 155

List of Figures

2.1 Primitive lattice vectors. 7
2.2 Conventional unit cells for cubic lattices. 8
2.3 Illustration of how crystal planes are defined using Miller indices. 10
2.4 Three dimensional stress tensor components. 13
2.5 Illustration of pure strain and rotation components of e_{ij}. 15
2.6 Illustration of an edge dislocation and a Burgers circuit. 19
2.7 Plastic deformation by glide of an edge dislocation. 20
2.8 Illustration of the Schmid factor. 21
2.9 Stacking fault in fcc metal showing close-packed (111) planes and a single Shockley partial dislocation. 23
2.10 Frank stacking faults. 24
2.11 Twinning in fcc structure by shearing on the (111) plane. 25
2.12 Twinning in bcc structure by shearing on the (112) plane. 26
2.13 Illustration of Bragg's law of diffraction. 27
2.14 Illustration of von Laue formulation of x-ray diffraction. 28
2.15 Dynamical diffraction, interference of reflected rays. 32
2.16 Imperfect 'mosaic' crystal. 33
2.17 Laue method (a) in back-reflection (b) in transmission. 35
2.18 Powder diffraction geometry. 36
2.19 Ewald sphere constructions. 37
2.20 Schematic of shock wave propagation. 38
2.21 Schematic of Hugoniot curve. 41
2.22 Shock Hugoniot in a solid. 42
2.23 Shock dislocation models. 44
2.24 The Lennard-Jones potential. 47

3.1 Target area 1. 55
3.2 Schematic diagram of the flat crystal spectrometer. 58
3.3 10 μm single crystal Cu and 'thick' single crystal Cu targets. . . . 60
3.4 Top down view of the experimental set-up. 63
3.5 The Janus chamber as set up for white-light Laue experiments. . . 63
3.6 Image plate and target holder. 64
3.7 Schematic diagram of the nanosecond white-light Laue set-up. . . 65
3.8 Simplified schematic of the twin bed VISAR system used at Janus. 68
3.9 VISAR raw data. 71
3.10 Copper-NaCl interface particle velocity-time profile.] 72
3.11 Hugoniot plots for copper and NaCl. 74
3.12 Fitting code interface for crystal parameters. 76
3.13 Fitting code interface for image plate. 78
3.14 Example of simulated diffraction plot. 81
3.15 Ray tracing principle. 82

4.1 Crystal spectrometer raw data. 85
4.2 Calibration curve for (111) silicon crystal spectrometer. 86
4.3 Typical backlighter x-ray spectrum after energy calibration. . . . 87
4.4 X-ray spectra for a range of laser irradiances. 89
4.5 Plot of x-ray yield against laser irradiance. 90
4.6 Fluorescence background subtraction. 92
4.7 Plot of x-ray fluence against energy. 92
4.8 Diffraction pattern from unshocked, 50μm thick silicon. 94
4.9 Lineouts through several diffraction peaks. 95
4.10 Diffraction from shocked silicon. 96
4.11 Silicon pressure against V/V_0 plot. 97
4.12 Stacking faults in MD and resulting FT. 99
4.13 Copper single crystal characterisation. 101
4.14 Plot of peak pressure versus incident drive intensity. 102
4.15 Typical diffraction data from copper shocked along the [001] axis. 104
4.16 Elimination of drive orientation as the source of the extra peaks. . 106
4.17 Twin positions. 108
4.18 MD simulation for shocks along [001] in Cu (Mishin potential). . . 110
4.19 Stacking fault densities and rotation angles for MD simulations. . 111

4.20 (002) diffraction peaks for six shots over a range of different pressures. 112
4.21 Plot of lattice rotation angle against peak pressure. 113
4.22 Slip rotation under confined strain 114
4.23 Stereographic projection for cubic crystals. 115

5.1 Hugoniot for Ta EFS potential and experimental data. 124
5.2 Wave profiles for shock along [001]. 126
5.3 Fourier transforms of twinned region. 128
5.4 Atoms coloured by PASF method. 131
5.5 3D pair correlation function. 135
5.6 3D pair correlation function for idealised shear and shuffle mechanism. 136
5.7 Effect of initial uniaxial strain on twinning atomic displacements. 137
5.8 Twinning mechanism. 138
5.9 Relative displacements for a small region of one twin variant. . . . 139

1 Geometry and parameters for lattice rotation during glide. 147

Nomenclature

Greek Symbols

ρ_d	Dislocation density
ω_{ij}	Rotation tensor
ϵ	Strain
ϵ_{ij}	Pure strain tensor
σ	Stress

Other Symbols

c	Compliance
d_{hkl}	Inter-planar spacing
$\perp$	Dislocation
e	Engineering strain
e_{ij}	Relative displacement tensor
$\mathbf{G}_{hkl}$	Reciprocal lattice vector
$\mathbf{k}$	Wavevector
$\mathbf{R}$	Lattice translation vector
s	Stiffness
U_p	Particle velocity

U_z Shock velocity

Acronyms

bcc Body Centred Cubic

cd Cubic Diamond

CSP Centro-symmetry parameter

EOS Equation of state.

EPD Enthought Python Distribution

fcc Face Centred Cubic

HEL Hugoniot Elastic Limit

IP Image plate.

LAMMPS Large-scale Atomic Molecular Massively Parallel Simulator

LJ Lennard-Jones

LLE Laboratory for Laser Energetics (Rochester, NY).

LLNL Lawrence Livermore National Laboratory.

MD Molecular dynamics

PSL Photo-stimulated luminescence.

RAL Rutherford Appleton Laboratory, UK.

TA1 Target area 1.

TEM Transmission electron microscopy

TXRD Time-resolved X-ray diffraction.

VISAR Velocity Interferometer System for Any Reflector.

VPF Velocity per fringe.

Chapter 1

Introduction

1.1 Historical context

The field of shock wave research arguably originated in the work of Rankine and Hugoniot in the late 19th century. They independently derived the set of conservation equations, subsequently known as the Rankine-Hugoniot equations, which describe the propagation of a shock wave [1, 2, 3]. Hugoniot also lends his name to the locus of states (of pressure, density, temperature) which a material can jump under shock compression, known simply as the Hugoniot. Experimentally, the field took off during the 1940s and 50s when the behaviour of materials under explosively driven shock wave compression became of interest. Shock waves became a tool for accessing high pressure states which were not attainable using the static techniques of the day. Materials at extreme pressures were and are of interest in a number of areas. For example, generating high pressure states in the laboratory allows the study of materials in the conditions found in planetary cores, which are understandably difficult to study *in situ*, where a material's structure and properties often differ from the ambient state.

The development of the field is perhaps typified by the α-ϵ phase transition in iron. Iron was popular in early high pressure work due to its geophysical importance as the main constituent of the Earth's core. In the 1950s, iron shock wave profile measurements by Walsh and also Bancroft indicated a structural phase transition at 13 GPa [4, 5]. The phase change was later observed in static compression by Jamieson and Lawson, and identified by x-ray diffraction as the α-ϵ transition[1], demonstrating that high pressure work through shock loading could inform static pressure research [6]. The same transition was later observed via *in situ* x-ray diffraction experiments confirming the phase transition was the same as in the static case [7, 8], and also in large-scale molecular dynamics (MD) simulations [9], which are both themes of this thesis.

The early dynamic loading experiments utilised explosives and explosively driven flyer plates to generate a shock. Later development used gas guns to reach flyer velocities up to $5\,\mathrm{kms}^{-1}$, and later two-stage gas guns with flyer velocities up to $15\,\mathrm{kms}^{-1}$. By measuring the shock velocity and particle velocity (estimated using the rear surface velocity), the Hugoniot data for a vast array of materials were generated with these techniques [10]. The 1960s saw the development of high power lasers and laser ablation used to drive a shock wave into targets[2]. The invention of the laser also saw developments in experimental diagnostics. The Velocity System for Any Reflector (VISAR) was developed for improved velocity profile measurements and has been a key diagnostic for shock experiments ever since [11].

Not only were high power lasers proving useful for driving the compression, they also provided a means for generating ultra-short, high intensity x-ray pulses

[1] ϵ denoting hexagonal close-packed.

[2] Many of these high power laser systems were developed for inertial confinement fusion research.

which could be used to probe the shocked state. Earlier work had used flash x-ray sources and it was the work of Johnson in 1970, that demonstrated the insight gained by time-resolved X-ray diffraction (TXRD) techniques, producing the first evidence that crystals remained crystalline under shock compression [12, 13]. The combined use of the laser for both shock drive and x-ray source was demonstrated by Wark in the late 1980s [14, 15]. These studies predominantly used the Bragg geometry and the quasi-monochromatic line emission of a laser-plasma, focusing on the shifts of single diffraction lines as the lattice plane spacing changed under compression. The technique was augmented by introducing a wide angle detector, to record multiple reflections, by Kalantar and collaborators [7, 8].

Although, as described earlier for iron, static and shock compression can probe the same high pressure states, the dynamic nature of the shock wave makes comparison between the two difficult in many cases. Planar shock waves often produce different behaviour in different crystallographic directions as the compression is uniaxial rather than hydrostatic. It is well known that for many simple metals the Hugoniot closely follows the pressure-volume curve for hydrostatic compression. For this to occur, the large shear stresses must be relieved, it is thought by the generation of defects and their subsequent shear-stress driven motion.

Along with developments in high power laser technologies and diagnostics, there has been huge development in computational power. Large-scale molecular dynamics simulations have been used to investigate the lattice level dynamics of shocks for several decades. Early work by Mogilevskii explored shock waves in two dimensional systems, with simple atomic potentials showing complex behaviour [16]. Pioneering work by Holian and co-workers showed that large numbers of stacking faults were generated in fcc crystals using the relatively simple Lennard-Jones potential [17]. MD simulations of iron showed the α-ϵ phase transition

[9]. The defect densities observed in these multi-million atom simulations are consistent with the classic Orowan equation of plasticity [18].

Despite the insight gained to date, by *in situ* x-ray diffraction and large-scale MD simulations, direct experimental evidence for the expected high defect densities during the shock does not yet exist. Broadening of diffraction peaks observed in both shocked copper [19], aluminium [20] and LiF [21] are consistent with large defect densities but do not provide any information about the orientation or type of generated defects. Measurement of defect density during the shock wave remains an elusive and important result in the field.

1.2 Thesis layout and role of the author

Chapter 2 reviews some of the relevant background theory. The theory is broken down into sections on: Crystal structure, X-ray diffraction, Shock waves, and Molecular dynamics simulations. This chapter is clearly by no means exhaustive and only really serves to define some of the terminology used later in this thesis. This background theory is drawn from a variety of sources and as such can be found in the relevant text books and given references.

Chapter 3 describes the design and development of a nanosecond white-light Laue technique. The x-ray source, target design, and diagnostics are described. The VISAR analysis technique and Laue diffraction fitting code are detailed. The white-light Laue technique was conceived by Giles Kimminau and Justin Wark. The first development experiment was performed by James Hawreliak, Giles Kimminau and the author. Analysis of the first experiment was by Giles Kimminau and the author. The fitting code is the work of the author. This work is published in Review of Scientific Instruments, reference [22].

Chapter 4 presents the results for the elastic shock compression of silicon and the plastic compression of copper, using the nanosecond white-light Laue technique. An interpretation is given for the observed diffuse scattering for single crystal copper shocked along the [001] axis. These results were gained over two experimental runs performed with the aid of many people: James Hawreliak, Andrew Higginbotham, Gabriele Mogni, Andrew Comley, Patrick Dunne, Amy Lazicki, to name a few. Both experiments were planned and lead by the author in liaison with James Hawreliak at LLNL. The analysis of the x-ray spectrum, VISAR velocity profiles, and diffraction data is the work of the author. This work is published in Nature Communications, reference [23].

Chapter 5 details MD simulations of shocked single crystal tantalum. The data are analysed using Fourier transforms and a new order parameter (PASF) is developed for identifying individual twins. The twinning mechanism observed in the simulation is deduced. The work presented in this chapter is the work of the author and Andrew Higginbotham. The MD simulations were performed by the author. The code used to perform the PASF analysis was written by Andrew Higginbotham. The identification of the twinning mechanism is the work of the author. This work is in the late stage of preparation for submission to Phys. Rev. B.

Chapter 6 gives a brief summary of the results and outlines future work.

Chapter 2

Background Theory

This chapter gives a brief overview of the theory relevant to the work in this thesis. It is divided into four main sections; crystal structure, x-ray diffraction, shock waves, and molecular dynamics simulations. The notation and terms used in later chapters are introduced.

2.1 Crystal structure

2.1.1 Lattices

A crystal is made up of units of atoms or molecules which are repeated on a periodic array of points known as a lattice. In three dimensions a lattice can be constructed using a translation vector

$$\mathbf{R} = m_1\mathbf{a}_1 + m_2\mathbf{a}_2 + m_3\mathbf{a}_3 \tag{2.1}$$

where m_1, m_2, and m_3 are integers through all values (including zero and negative integers) [24]. The three vectors $\mathbf{a}_1$, $\mathbf{a}_2$, and $\mathbf{a}_3$ must not be coplanar and are called

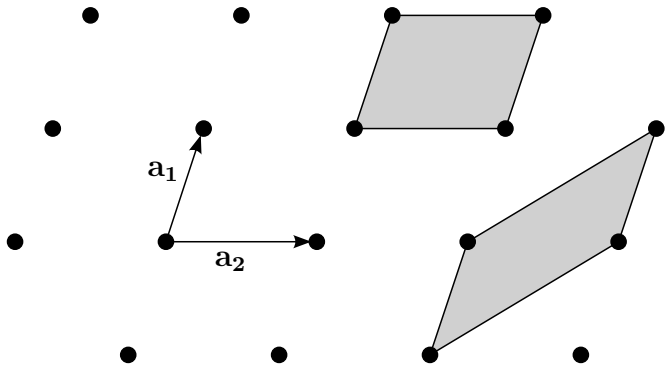


Figure 2.1: Two dimensional lattice with primitive lattice vectors $\mathbf{a}_1$ and $\mathbf{a}_2$. Two potential primitive unit cells are shown.

primitive vectors. Each lattice point is equivalent and the lattice appears the same if the origin is placed at any lattice point. The primitive vectors form the edges of a parallelepiped which fills all space without overlapping when translated to all lattice points and is called a primitive unit cell. This parallelepiped is the most obvious primitive unit cell but in fact, any volume which has this behaviour is a primitive unit cell. Primitive unit cells contain only one lattice point and have a volume given by $v = \mathbf{a}_1 \cdot \mathbf{a}_2 \times \mathbf{a}_3$ which is the smallest volume that will fill the lattice when repeated at each lattice point. It is often more convenient to use a larger unit cell, known as the conventional unit cell, which also fills the lattice when translated to a subset of the lattice vectors.

In general, the lengths of the vectors and the angles between them can be arbitrary. If $\mathbf{a}_1$, $\mathbf{a}_2$, and $\mathbf{a}_3$ have the same magnitude and are orthogonal then the lattice is cubic. If $a_1 \neq a_2 \neq a_3$ and $\alpha \neq \beta \neq \gamma$ (the angles between the vectors) then the lattice is called triclinic. In three dimensions there are seven possible lattice systems. Additional lattices can be made by adding points to the unit cell at the body centre or on the faces. There are six possible lattice centrings; primitive, body centred, face centred, and three base centred centrings. Therefore, there are $7 \times 6 = 42$ combinations of system and centring. By choice

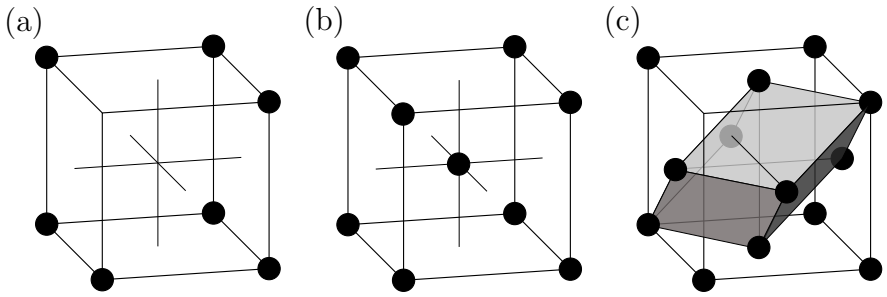


Figure 2.2: Conventional unit cells for cubic lattices, (a) simple cubic, (b) body centred cubic, and (c) face centred cubic. The primitive unit cell for the fcc lattice is also shown.

of axes, many of these combinations are equivalent and in total there are fourteen distinct lattices, first identified by Auguste Bravais, and known as Bravais lattices.

A large number of materials have a cubic lattice where the primitive lattice vectors are equal in magnitude and orthogonal. There are three cubic Bravais lattices, simple cubic, body centred cubic (bcc), and face centred cubic (fcc). The work in this thesis focuses on two materials, copper and tantalum, which are fcc and bcc respectively in their natural state. The conventional unit cell for a bcc lattice is formed by adding a lattice point at the centre of a cubic unit cell and contains two lattice points. The conventional unit cell for a fcc lattice is formed by additional points on each face of the cube and contains four lattice points. Figure 2.2 shows the conventional unit cells for cubic lattices.

The positions of the atoms or molecules within the unit cell, relative to the lattice point, are described by the basis. If the atoms labelled $1, 2, \ldots, n$ have positions $\mathbf{r}_1, \mathbf{r}_2, \ldots, \mathbf{r}_n$ within the unit cell, the positions of all the atoms of type n in the crystal are given by

$$\mathbf{R}^n = m_1\mathbf{a}_1 + m_2\mathbf{a}_2 + m_3\mathbf{a}_3 + \mathbf{r}_n \tag{2.2}$$

For materials with a one-atom basis, i.e. an atom at each lattice point, the crystal

structure is often abbreviated to the lattice type without stating the basis. For example, one might say that copper has an fcc structure.

The bcc and fcc lattices can also be thought of as a simple cubic lattice with a basis.

$$\mathbf{r}_1 = \mathbf{0}, \quad \mathbf{r}_2 = \frac{1}{2}(\mathbf{a}_1 + \mathbf{a}_2 + \mathbf{a}_3) \quad \text{(bcc)} \tag{2.3}$$

$$\mathbf{r}_1 = \mathbf{0}, \quad \mathbf{r}_2 = \frac{1}{2}(\mathbf{a}_1 + \mathbf{a}_2), \quad \mathbf{r}_3 = \frac{1}{2}(\mathbf{a}_2 + \mathbf{a}_3), \quad \mathbf{r}_4 = \frac{1}{2}(\mathbf{a}_3 + \mathbf{a}_1) \quad \text{(fcc)} \tag{2.4}$$

Another common structure is cubic diamond (cd). It comprises a fcc lattice with a two atom basis

$$\mathbf{r}_1 = \mathbf{0}, \quad \mathbf{r}_2 = \frac{1}{4}(\mathbf{A}_1 + \mathbf{A}_2 + \mathbf{A}_3) \quad \text{(cd)} \tag{2.5}$$

where $\mathbf{A}_1$,$\mathbf{A}_2$, and $\mathbf{A}_3$ are the conventional unit cell lattice vectors. The cubic diamond lattice has four lattice points and eight atoms per conventional unit cell.

2.1.2 Directions and planes

It is often necessary to define specific lattice directions and planes of atoms, and there are several conventions. Lattice directions are specified by the integers m_1, m_2, and m_3 and are given in square brackets without separating commas such as $[m_1 m_2 m_3]$. Negative values are written with a bar, $\bar{m}$, rather than $-m$ to avoid confusion. Multiple equivalent directions due to the symmetry of the lattice are written as a family of directions using angled brackets e.g. $[100], [010], [001], [\bar{1}00], \ldots$ is written as $\langle 100 \rangle$.

Three lattice points which are non-collinear define a lattice plane, and due to the translational symmetry of the lattice, a family of lattice planes which are parallel and equidistant in the perpendicular direction. The convention is that one

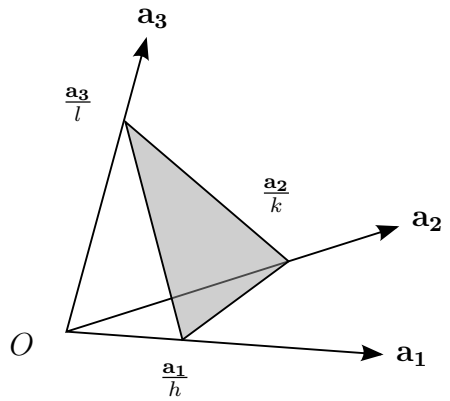


Figure 2.3: Illustration of how crystal planes are defined using Miller indices.

	Notation	Example
Lattice direction	Square brackets	[111]
Family of lattice directions	Angled brackets	$\langle 111 \rangle$
Lattice plane	Parentheses	(111)
Family of lattice planes	Curly brackets	{111}

Table 2.1: Summary of notation for lattice directions and planes.

lattice plane passes through the origin and nearest lattice plane makes intercepts with the lattice axes at a_1/h, a_2/k, and a_3/l, where h,k, and l are called Miller indices, as illustrated in figure 2.3. To differentiate from the notation for lattice directions, lattice planes are given in round brackets (hkl). In a similar manner to lattice directions, families of planes which are equivalent due to symmetry are indicated by curly brackets, e.g. $(100), (010), (\bar{1}00), \ldots$ is represented as $\{100\}$. Table 2.1 summarises the notation.

Another related concept is that of the zone axis. If two planes intersect, the direction parallel to the intersection is called the zone axis. If the plane normal is $[hkl]$ then the zone axis $[uvw]$ will satisfy $uh + vk + wl = 0$. Three planes will

have a common zone axis if the determinant of their miller indices is zero.

$$\begin{vmatrix} h_1 & k_1 & l_1 \\ h_2 & k_2 & l_2 \\ h_3 & k_3 & l_3 \end{vmatrix} = 0 \tag{2.6}$$

2.1.3 The Reciprocal lattice

For a three dimensional set of lattice vectors $\mathbf{a}_1$, $\mathbf{a}_2$, $\mathbf{a}_3$ a reciprocal lattice can be constructed using reciprocal lattice vectors $\mathbf{b}_1$, $\mathbf{b}_2$, $\mathbf{b}_3$ given by

$$\mathbf{b}_1 = 2\pi \frac{\mathbf{a}_2 \times \mathbf{a}_3}{\mathbf{a}_1 \cdot (\mathbf{a}_2 \times \mathbf{a}_3)} \tag{2.7}$$

$$\mathbf{b}_2 = 2\pi \frac{\mathbf{a}_3 \times \mathbf{a}_1}{\mathbf{a}_2 \cdot (\mathbf{a}_3 \times \mathbf{a}_1)} \tag{2.8}$$

$$\mathbf{b}_3 = 2\pi \frac{\mathbf{a}_1 \times \mathbf{a}_2}{\mathbf{a}_3 \cdot (\mathbf{a}_1 \times \mathbf{a}_2)} \tag{2.9}$$

The reciprocal lattice points are defined by the translation vector as earlier for the real lattice

$$\mathbf{G}_{hkl} = h\mathbf{b}_1 + k\mathbf{b}_2 + l\mathbf{b}_3 \tag{2.10}$$

The use of hkl similar to the Miller indices described in section 2.1.1 is deliberate. Looking at figure 2.3, the vectors $(\mathbf{a}_2/k - \mathbf{a}_1/h)$ and $(\mathbf{a}_3/l - \mathbf{a}_1/h)$ are in the plane (hkl). Taking the dot product with $\mathbf{G}_{hkl}$

$$\left(\frac{\mathbf{a}_2}{k} - \frac{\mathbf{a}_1}{h}\right) \cdot (h\mathbf{b}_1 + k\mathbf{b}_2 + l\mathbf{b}_3) = 1 - 1 = 0 \tag{2.11}$$

$$\left(\frac{\mathbf{a}_3}{l} - \frac{\mathbf{a}_1}{h}\right) \cdot (h\mathbf{b}_1 + k\mathbf{b}_2 + l\mathbf{b}_3) = 1 - 1 = 0 \tag{2.12}$$

demonstrates that $\mathbf{G}_{hkl}$ is perpendicular to the lattice planes.[1] Since $\mathbf{G}_{hkl}$ is perpendicular to the plane (hkl), the perpendicular separation of the planes d_{hkl} is given by

$$d_{hkl} = \frac{\mathbf{a}_1}{h} \cdot \frac{(h\mathbf{b}_1 + k\mathbf{b}_2 + l\mathbf{b}_3)}{|\mathbf{G}_{hkl}|} = \frac{2\pi}{|\mathbf{G}_{hkl}|} \tag{2.13}$$

This quantity, the interplanar spacing, is useful in the theory of crystal diffraction. For a cubic lattice it is simply

$$d_{hkl} = \frac{a}{\sqrt{h^2 + k^2 + l^2}} \tag{2.14}$$

2.1.4 Stress and strain

Shock waves generate states with high stresses and large strains. These physical quantities are introduced here.

2.1.4.1 Stress

Stress is defined as the force per unit area acting on a body. In the simple case of a bar, with cross-section A, loaded axially with a force F, the stress σ is given by $\sigma = F/A$. In three dimensions, the stress at any point is defined by nine components, each representing a surface area and the direction of the force acting upon it. These components are given by the second rank tensor

$$\sigma = \begin{pmatrix} \sigma_{11} & \sigma_{12} & \sigma_{13} \\ \sigma_{21} & \sigma_{22} & \sigma_{23} \\ \sigma_{31} & \sigma_{32} & \sigma_{33} \end{pmatrix} \tag{2.15}$$

[1] The factor of 2π comes from an alternative derivation of the reciprocal lattice. If a plane wave $e^{i\mathbf{G}\cdot\mathbf{r}}$ has the same periodicity as the lattice, then $e^{i\mathbf{G}\cdot(\mathbf{r}+\mathbf{R})} = e^{i\mathbf{G}\cdot\mathbf{r}}$. The solution introduces the factor 2π.

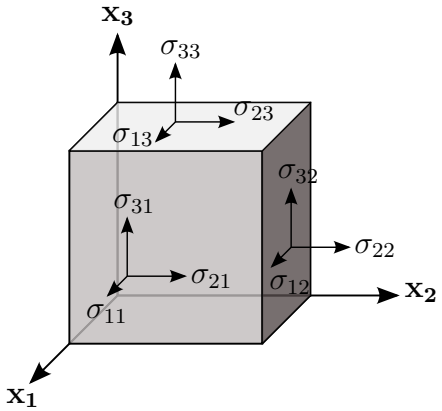


Figure 2.4: Three dimensional stress tensor components.

where each element σ_{ij} represents a force acting along the x_i axis on a surface with a normal parallel to the x_j axis, as summarised in figure 2.4. The diagonal elements $\sigma_{11}, \sigma_{22}, \sigma_{33}$ are called normal stresses, where the forces act perpendicular to the surfaces. The off-diagonal elements are called shear stresses, where the forces act parallel to the respective surfaces. To conserve angular momentum in equilibrium, the stress tensor must be symmetric, i.e.

$$\sigma_{12} = \sigma_{21},\ \sigma_{13} = \sigma_{31},\ \sigma_{23} = \sigma_{32}. \tag{2.16}$$

hence there are six independent stress components, three normal stresses and three shear stresses.

The sign convention is that the forces represent the external force acting on the body, hence a positive normal stress indicates tension and the negative indicates compression. The total pressure, P, is given by the negative of the trace of the stress tensor.

$$P = -\frac{1}{3}(\sigma_{11} + \sigma_{22} + \sigma_{33}) \tag{2.17}$$

2.1.4.2 Strain

Strain is a measure of the deformation produced by stress. In one dimension, the strain is usually defined as the change in length over the original length.

$$d\epsilon = \frac{dl}{l} \tag{2.18}$$

which upon integration gives

$$\epsilon = \ln \frac{l}{l_0} \tag{2.19}$$

which is the *true* strain. Often a simplified form is used, called the engineering strain, which is given by

$$e = \frac{\Delta l}{l_0} = \frac{l_1}{l_0} - 1 \tag{2.20}$$

$$l_1 = l_0(1 + e) \tag{2.21}$$

In two and three dimensions we can describe the strain in terms of the displacement of each point in the material from its position in the undeformed state. In two dimensions, let the point P in the unstrained state move to point P' in the deformed state. P is at the co-ordinates (x_1, x_2) and P' is at $(x_1 + u_1, x_2 + u_2)$. For a point at co-ordinates $(x_1 + dx_1, x_2 + dx_2)$ the displacement is given by the vector $(u_1 + du_1, u_2 + du_2)$ where:

$$du_1 = \frac{\partial u_1}{\partial x_1} dx_1 + \frac{\partial u_1}{\partial x_2} dx_2 \tag{2.22}$$

$$du_2 = \frac{\partial u_2}{\partial x_1} dx_1 + \frac{\partial u_2}{\partial x_2} dx_2 \tag{2.23}$$

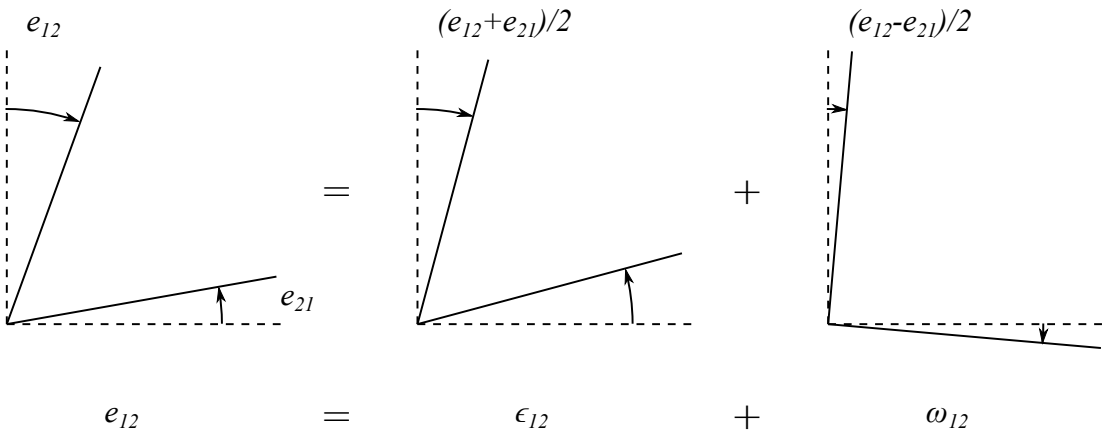


Figure 2.5: Illustration of pure strain and rotation components of e_{ij}.

These equations can be written compactly as:

$$du_i = e_{ij} dx_j \tag{2.24}$$

$$e_{11} = \frac{\partial u_1}{\partial x_1}, \quad e_{12} = \frac{\partial u_1}{\partial x_2}, \quad e_{22} = \frac{\partial u_2}{\partial x_2}, \quad e_{21} = \frac{\partial u_2}{\partial x_1} \tag{2.25}$$

The tensor e_{ij} is the relative displacement tensor. If we set $dx_x = 0$, then $du_1 = e_{11} dx_1$ and $du_2 = e_{21} dx_1$, showing that e_{11} is extension ratio along x_1 and e_{21} is a measure of the anti-clockwise rotation. Similarly, e_{22} is the extension per unit length along x_2 and e_{12} is the clockwise rotation. The tensor e_{ij} can be decomposed into symmetrical and anti-symmetrical tensors ϵ_{ij} and ω_{ij}.

$$e_{ij} = \epsilon_{ij} + \omega_{ij} \tag{2.26}$$

$$\epsilon_{ij} = \frac{1}{2}(e_{ij} + e_{ji}) \tag{2.27}$$

$$\omega_{ij} = \frac{1}{2}(e_{ij} - e_{ji}) \tag{2.28}$$

The tensor ϵ_{ij} is the *pure* strain and the tensor ω_{ij} is the rotation. The separation of the strain and rotation components is illustrated in figure 2.5.

In three dimensions the strain tensor is therefore given by:

$$\epsilon_{ij} = \begin{pmatrix} \epsilon_{11} & \epsilon_{12} & \epsilon_{13} \\ \epsilon_{21} & \epsilon_{22} & \epsilon_{23} \\ \epsilon_{31} & \epsilon_{32} & \epsilon_{33} \end{pmatrix} = \begin{pmatrix} e_{11} & \frac{1}{2}(e_{12}+e_{21}) & \frac{1}{2}(e_{13}+e_{31}) \\ \frac{1}{2}(e_{21}+e_{12}) & e_{22} & \frac{1}{2}(e_{23}+e_{32}) \\ \frac{1}{2}(e_{31}+e_{13}) & \frac{1}{2}(e_{32}+e_{23}) & e_{33} \end{pmatrix}. \quad (2.29)$$

The diagonal components are the extension per unit length and are called the normal strains. The off-diagonal components are called shear strains in the same way as the shear stresses described earlier. The symmetric nature of the strain tensor means that like the stress tensor, there are six independent components of strain. It also means that certain axes can be chosen such that the shear strains are zero and only the normal strains are left. These axes are known as the principle axes and the resulting normal strains are the principle strains.

2.1.5 Elasticity and plasticity

For small strains the relationship between stress and strain is linear; this is Hooke's law. In one dimension the stress and strain are related by the compliance c or the stiffness s, its reciprocal.

$$\sigma = c\epsilon, \quad \epsilon = s\sigma \quad (2.30)$$

In three dimensions this is extended to the full stress and strain tensors. Since these are second rank tensors the compliance and stiffness are represented by fourth rank tensors.

$$\sigma_{ij} = c_{ijkl}\epsilon_{kl} \quad (2.31)$$

$$\epsilon_{ij} = s_{ijkl}\sigma_{kl} \quad (2.32)$$

The symmetry of the stress and strain tensors lets us reduce the number components of c_{ijkl} and s_{ijkl} from the typical 81 components of a fourth rank tensor. For example, since $\epsilon_{12} = \epsilon_{21}$ the corresponding compliance components can be set to equal, $c_{ij12} = c_{ij21}$. Similar arguments apply, and depending on the symmetry class of the structure the number of components can be reduced to relatively few. For the cubic structure there are three independent components and the compliance can be represented by

$$\begin{pmatrix} c_{11} & c_{12} & c_{12} & 0 & 0 & 0 \\ c_{12} & c_{11} & c_{12} & 0 & 0 & 0 \\ c_{12} & c_{12} & c_{11} & 0 & 0 & 0 \\ 0 & 0 & 0 & c_{44} & 0 & 0 \\ 0 & 0 & 0 & 0 & c_{44} & 0 \\ 0 & 0 & 0 & 0 & 0 & c_{44} \end{pmatrix}. \tag{2.33}$$

where the notation is also reduced such that $c_{iijj} = c_{ij}$. These tensors are only really useful when dealing with single crystals. For polycrystalline materials, the potentially random orientation of the crystallites makes them inapplicable. The elastic properties of isotropic materials such as polycrystals are better described using a variety of constants or moduli. The Young's modulus E is simply the stress divided by the strain, as might be measured in a tension test. Poisson's ratio is the negative of the ratio between the strain transverse to the direction of the force and the strain parallel to the force.

As stated earlier, for small strains a crystal will deform elastically and when the force is removed, it will return to its original shape. If a sufficient stress is applied the crystal will deform plastically, and its shape will change irreversibly. The most common form of plastic deformation in metals is glide. This is the

translation of one region of the crystal over another. This form of plastic deformation is mediated by defects in the crystal lattice called dislocations which are discussed in the next section along with another form of plastic deformation called twinning.

2.1.6 Crystal defects

Crystals are generally not as perfectly ordered as the theory in section 2.1.1 would suggest. In reality they contain imperfections or defects which disturb the local arrangement of the atoms. There are many different types of defect but they can be grouped by dimension; point (0D), line (1D), planar (2D), and volume (3D) defects.

Point defects can be intrinsic or extrinsic. Intrinsic point defects occur when an atom is missing from a lattice site, a vacancy or where an atom is squeezed into a non-lattice site, known as an self-interstitial. Extrinsic point defects involve impurity atoms, either substituted in place of an atom of the parent material, or as an interstitial. Intrinsic point defects can be generated by plastic deformation but are also introduced simply due to thermal motion. Line defects, or dislocations, and a planar defect known as a stacking fault are covered in more detail in sections 2.1.6.1 and 2.1.6.2. Voids and precipitates are examples of volume defects.

2.1.6.1 Dislocations

The theory of dislocations was developed by Orowan, Polanyi, and Taylor, in the 1930-50s in an attempt to understand the difference between the theoretical critical shear stress and the experimentally observed stress required for plastic deformation [18, 25]. The theoretical critical shear stress is given by $\tau \approx G/2\pi$, where G is the shear modulus, typically of order 50GPa for metals, orders of

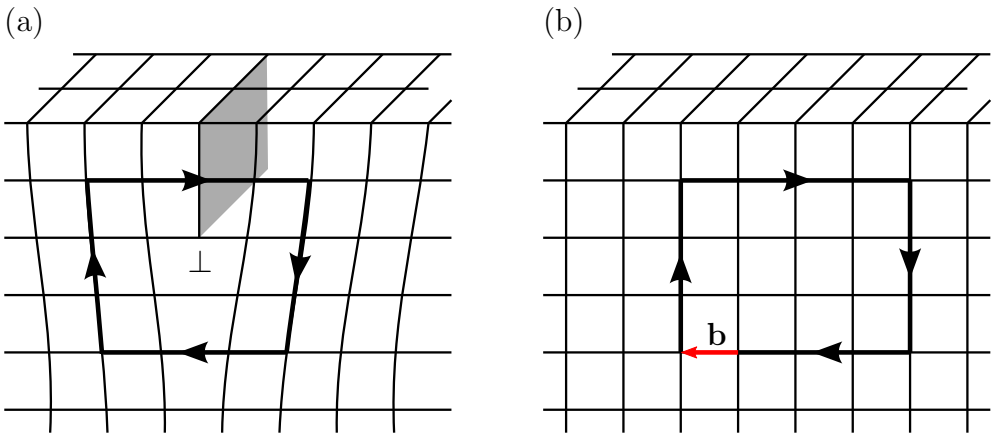


Figure 2.6: Illustration of an edge dislocation and a Burgers circuit. In (a) the grey plane represents an extra half-plane of atoms inserted into the lattice constructing an edge dislocation. The Burgers circuit is indicated in bold, and in (b) the same path is shown in the dislocation-free crystal. The Burgers vector **b**, which closes the circuit, is shown in red.

magnitude greater than the shear stress typically required for plastic deformation. For slip to occur, it was suggested that rather than all the atoms above the slip plane simultaneously slipping over the region below, that a line separated the regions where slip had and had not ocurred, which propagated in the slip plane. Experimental observations of dislocation were made by viewing etch pits formed where dislocations intersected the surface, and later via electron microscopy and other techniques [26].

The two main types of dislocation are edge dislocations and screw dislocations. Figure 2.6 shows model of an edge dislocation, which is labelled by the $\perp$ symbol, and also illustrates the concept of the Burgers circuit and Burgers vector. The Burgers circuit is an atom-to-atom path which encloses the dislocation, large enough that it passes through undisturbed crystal. If the same path is taken in a dislocation-free region it will not close, and the vector connecting the end to the start is the Burgers vector. This is a useful characteristic quantity for a dislocation. From figure 2.6 it can be seen that the Burgers vector for

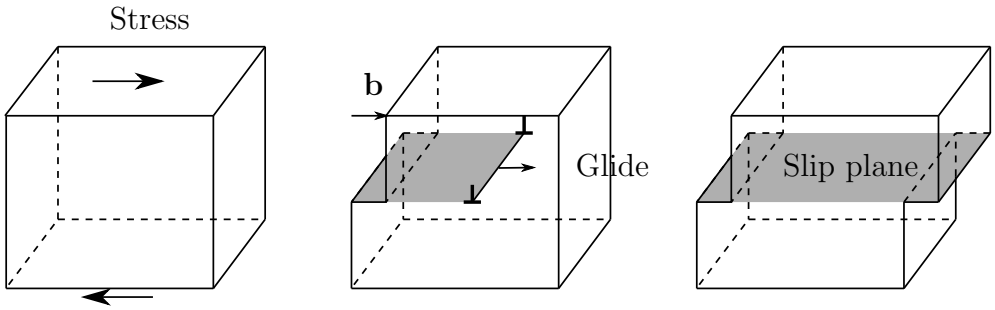


Figure 2.7: Plastic deformation by glide of an edge dislocation. The atoms either side of slip plane are displaced by the Burgers vector as the dislocation glides past. The slip direction is therefore parallel to the Burgers vector of the dislocation.

an edge dislocation is normal to the dislocation line. The Burgers vector for a screw dislocation is parallel to the dislocation line. Dislocations can be of mixed character with both edge and screw components and Burgers vector at an acute angle to the dislocation line.

The dislocation density ρ_d can be defined as the number of dislocations intersecting a unit area, or as the total line length per unit volume, given by

$$\rho_d = l/V \tag{2.34}$$

where l is the total length of dislocation line and V is the volume. It therefore has units of area, usually given in cm^{-2}. Typical dislocation densities in metals can vary from 10^6-$10^{10}\,\mathrm{cm}^{-2}$ depending on production method and annealing.

It is the lower stress required for dislocation motion that reconciles the difference discussed at the start of this section. If the dislocation moves within the plane containing the Burgers vector and the dislocation line, the motion is called glide. The result of dislocation glide is slip and the plane on which the glide occurs is the slip plane. The slip planes in a crystal are generally the planes with the highest density of atoms, for example in fcc metals the close-packed {111}

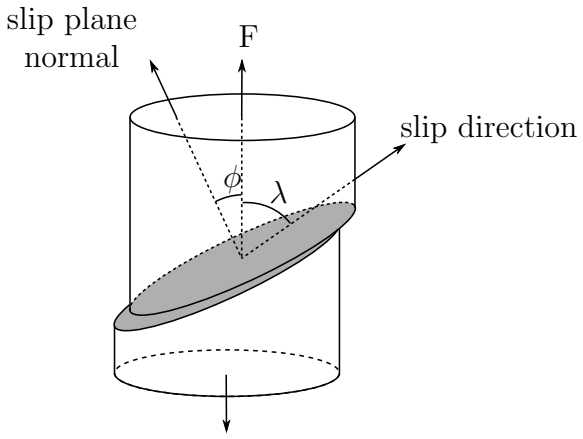


Figure 2.8: Illustration of the Schmid factor. The angles ϕ and λ used in the Schmid factor are the angles between the force and the slip plane normal and slip plane direction respectively [26].

planes are the typical slip planes. The Burgers vector of the dislocation producing the slip defines the direction of the slip (see figure 2.7), and is often the shortest lattice vector, i.e. $\langle 110 \rangle$ for fcc metals. The *slip system* is the combined slip plane and direction.

For slip to occur on a given slip system the resolved shear stress must be greater than a critical value. For an applied force F and cross-sectional area A, the shear stress resolved on a slip plane in the slip direction is given by

$$\tau = \frac{F}{A} \cos\phi \cos\lambda \tag{2.35}$$

where the angles are as shown in 2.8. The factor $\cos\phi\cos\lambda$ is known as the Schmid factor. Slip systems with the largest Schmid factor are the most likely to slip.

During glide, the plastic strain is directly related to the motion of the dislocations. The classic equation of plasticity, developed by Orowan is given by

$$\dot{\epsilon}_p = b\rho_m\langle v \rangle \tag{2.36}$$

where ρ_m is the density of mobile dislocations, b is the magnitude of the dislocations Burgers vector and $\langle v \rangle$ is their mean speed [18].

2.1.6.2 Stacking faults

The amount of energy stored by the distorted region around a dislocation is proportional to b^2 so we can write $E = Kb^2$ [26]. This is useful for determining if it is energetically favourable for two dislocations to combine to form a single dislocation or if a dislocation might dissociate into several. Although K depends on several factors such as the angles between the Burgers vectors, it is often the case that the values of b^2 are the determining factor. For example, if for three dislocations, $b_3^2 < b_1^2 + b_2^2$ then the dislocations with Burgers vectors $\mathbf{b_1}$ and $\mathbf{b_2}$ will combine to form $\mathbf{b_3}$. This is Frank's rule for predicting the stable dislocations for a given structure [27].

Frank's rule implies that a dislocation will dissociate into dislocations with smallest Burgers vectors. If the dislocation's Burgers vector is already the shortest lattice vector then dissociation into two dislocations would create a fault since the movement of the shorter dislocation would not leave behind an unperturbed crystal. The faulted region typically has high energy. If the crystal structure is such that this energy is low then it may still be energetically favourable to split into two dislocations. These dislocations, with b less than the shortest lattice vector, are called partial dislocations and the region between them is called a stacking fault. The partial dislocations separate until there is equilibrium between the strain energies of the dislocations and the fault energy. This is important for copper which is one such material where partial dislocations form.

For fcc metals, the shortest lattice vectors are in the $\langle 110 \rangle$ directions and slip is on the $\{111\}$ planes which are the close-packed planes. A stacking fault on the

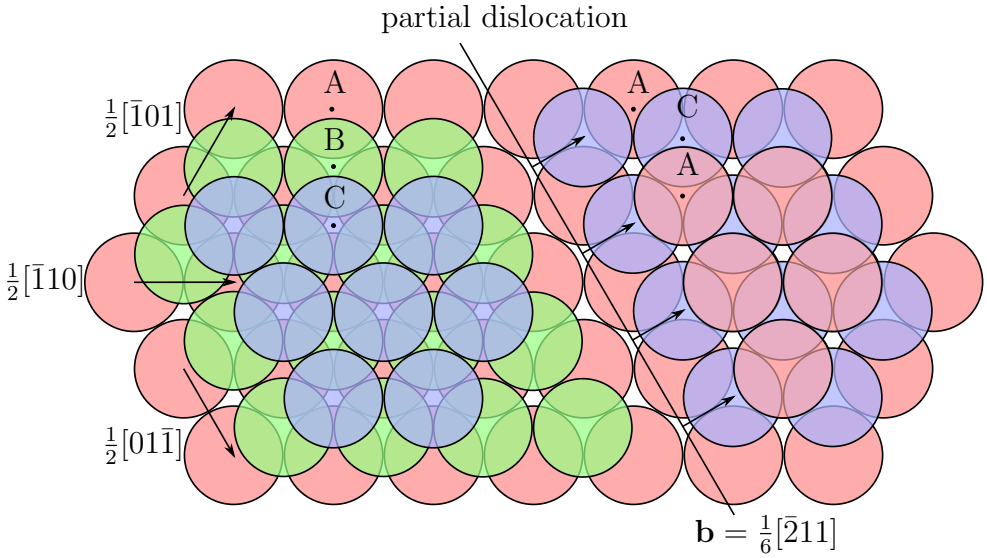


Figure 2.9: Stacking fault in fcc metal showing close-packed (111) planes and a single Shockley partial dislocation.

(111) plane is illustrated in figure 2.9. If we designate a chosen plane 'A', the next (111) plane can be in two positions 'B' or 'C'. Stacking the planes in the sequence ABCABCAB... generates the fcc structure, and stacking the planes ABABABAB... generates a hexagonal close-packed structure. For the sequence ABCABCAB, if the block above the A plane is shifted by $\frac{1}{6}[\bar{2}11]$ the stacking sequence becomes ABC**ACA**BC where the stacking fault is highlighted in bold.

As stated earlier, if the energy per unit area of the stacking fault is low enough, a full dislocation can separate into two partial dislocations with stacking fault between them. For fcc metals the $\frac{1}{2}\langle 110\rangle$ full dislocation separates into two $\frac{1}{6}\langle 211\rangle$ partial dislocations, which are known as Shockley partial dislocations. One partial dislocation is shown in figure 2.9 where a $\frac{1}{2}[\bar{1}01]$ has dissociated as follows:

$$\frac{1}{2}[\bar{1}01] \rightarrow \frac{1}{6}[\bar{2}11] + \frac{1}{6}[\bar{1}\bar{1}2] \tag{2.37}$$

Another partial dislocation which can bound a region of stacking fault is the

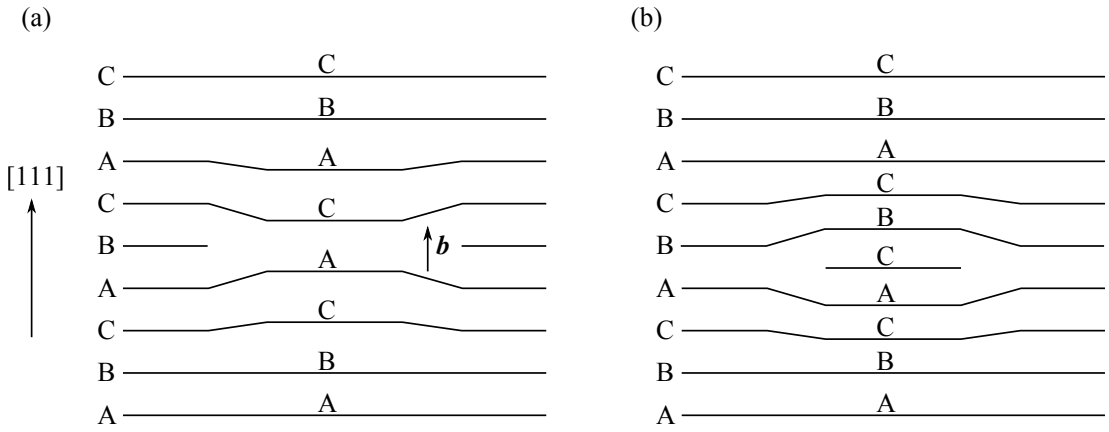


Figure 2.10: Frank stacking faults. (a) Intrinsic stacking fault (b) Extrinsic stacking fault. [27]

Frank partial dislocation. This type of dislocation occurs when a stacking fault is formed by inserting or removing a close-packed plane, for example when vacancies coalesce on a $\{111\}$ plane. Removing a plane results in the ABCACABC sequence creating an intrinsic stacking fault, and adding a plane produces an extrinsic stacking fault with ABCACBCABC. Both are shown in figure 2.10.

The Frank partial is an edge dislocation and as shown in figure 2.10 it has Burgers vector normal to the $\{111\}$ (i.e. it has Burgers vector $\frac{1}{3}\langle 111\rangle$). Since the Burgers vector is not in the $\{111\}$ slip plane the dislocation cannot glide and can only move by climb. A dislocation which cannot move by glide is known as a sessile dislocation.

2.1.6.3 Twinning

In the previous section a single fault was introduced into the stacking of close-packed planes. If the stacking order is instead reversed, producing ABCAB-CACBACB, the result will be two regions of crystal, with the same bulk structure, which are mirror images of each other. This is a form of crystal twinning. Formally, the symmetry operation does not necessarily have to be a mirror plane

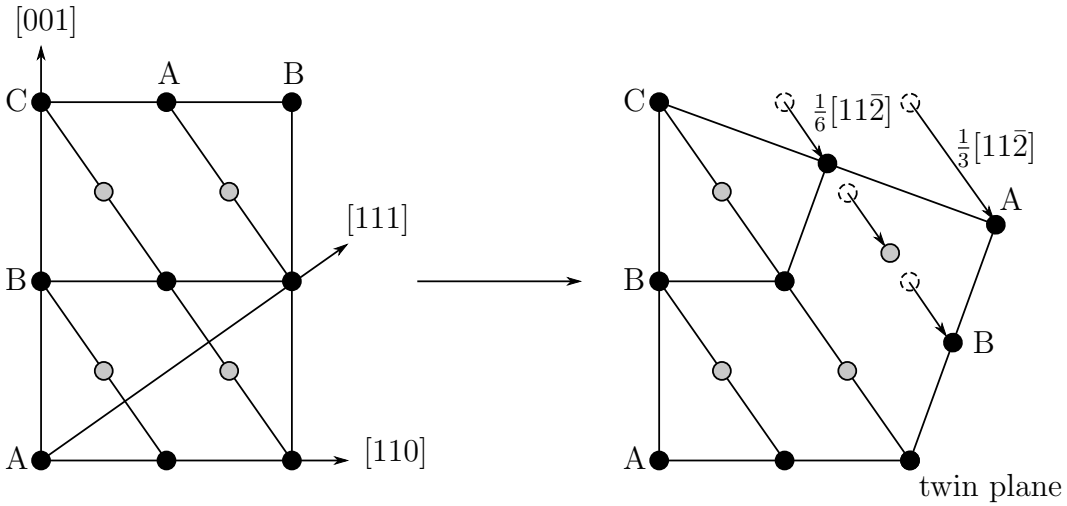


Figure 2.11: Twinning in fcc structure by shearing on the (111) plane. Black circles are in the plane and grey circles are above/below the plane.

but this is the most typical case. Crystal twins are often formed during crystal growth but are also an important deformation mechanism in some materials, especially metals with a bcc structure [28].

For fcc metals the stacking sequence idea used earlier provides a method for finding the displacements required for twinning. The plane that separates the twins is simply called the twin plane or twin boundary. If each plane above the twin plane is displaced by $\frac{n}{6}\langle 112\rangle$, where n is the separation in planes from the twin boundary, the stacking sequence is reversed, see figure 2.11.

For the bcc structure twinning occurs on the $\{112\}$ planes. For this plane there are six stacking positions before the sequence repeats, i.e. ABCDEFABCD.... Each plane above the twin plane is successively displaced by $\frac{1}{6}\langle 111\rangle$ to produce the twin as shown in figure 2.12.

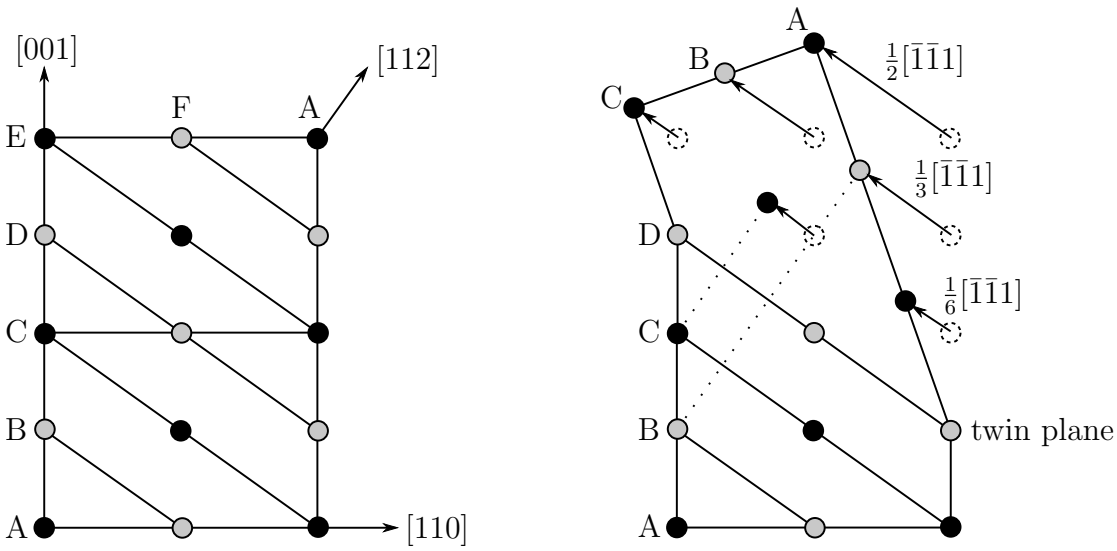


Figure 2.12: Twinning in bcc structure by shearing on the (112) plane. Black circles are in the plane and grey circles are above/below the plane.

2.2 X-ray diffraction

The typical interatomic spacings of solids are of the order of 10^{-10} m, an angstrom. X-rays, by definition, are electromagnetic radiation with energies in the range from 100 eV to 100 keV, which equates to wavelengths in the range from 0.01-10 nm, making them an ideal probe of the crystalline solids. This section outlines some of the basic theory used later in this work.

2.2.1 Bragg's law

Figure 2.13 shows two rays specularly reflected from two adjacent lattice planes. The planes are separated by d and the path difference between the two rays is given by $2d\sin(\theta)$ as shown in the figure.

For constructive interference between the two rays must be in phase and the path difference must be equal to the wavelength or a multiple of the wavelength.

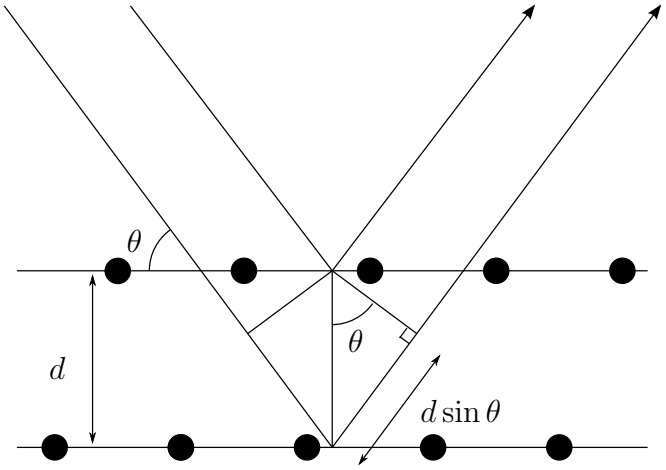


Figure 2.13: Illustration of Bragg's law of diffraction.

This leads to the condition known as Bragg's law:

$$n\lambda = 2d\sin(\theta) \tag{2.38}$$

This equation is of frequent use when using x-ray diffraction.

2.2.2 The Laue condition

A more general approach was developed around the same time by von Laue, and with this method, the connection with the reciprocal lattice described in section 2.1.3 is more apparent. The atoms in the lattice are considered as individual scatterers whose electrons elastically scatter the incident radiation in all directions. Again we calculate the condition for constructive interference. Figure 2.14 illustrates this for two atoms.

The wavevectors $\mathbf{k}$ have magnitude given by $\mathbf{k} = 2\pi/\lambda$. The vector from one atom to the other is $\mathbf{r}$ and the path difference is given by

$$r\cos\theta + rcos\theta' = \mathbf{r}\cdot(\hat{\mathbf{k}}' - \hat{\mathbf{k}}) \tag{2.39}$$

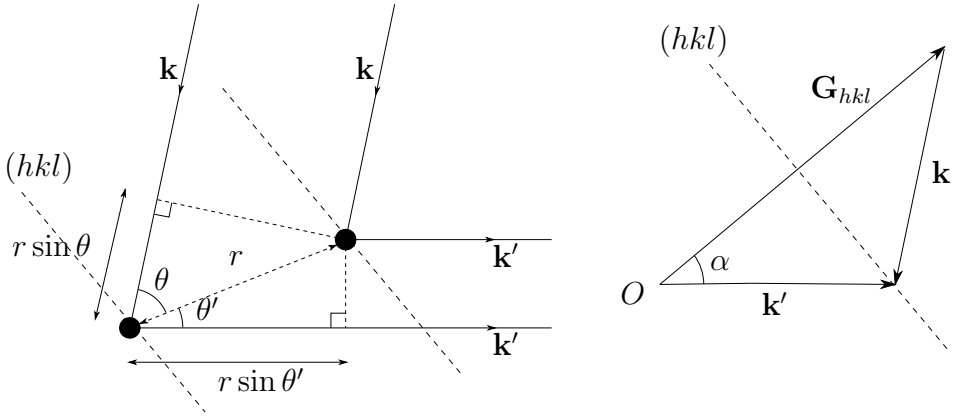


Figure 2.14: Illustration of von Laue formulation of x-ray diffraction. Right: the Laue condition.

For constructive interference the path difference is an integral number of wavelengths $m\lambda$, and multiplying by $2\pi/\lambda$ gives

$$\mathbf{r} \cdot (\mathbf{k}' - \mathbf{k}) = 2\pi m \tag{2.40}$$

Now we can substitute the lattice translation vector $\mathbf{R}$ for $\mathbf{r}$ to take into account the scattering from all the lattice points

$$\mathbf{R} \cdot (\mathbf{k}' - \mathbf{k}) = 2\pi m \tag{2.41}$$

Given the definition of the reciprocal lattice vector $\mathbf{G}$ and the reciprocal lattice vectors $\mathbf{b}_1$, $\mathbf{b}_2$, $\mathbf{b}_3$ we can see that $\mathbf{R} \cdot \mathbf{G} = 2\pi m$ and it follows that for constructive interference

$$\Delta\mathbf{k} = \mathbf{k} - \mathbf{k}' = \mathbf{G} \tag{2.42}$$

which is the Laue condition and is illustrated in figure 2.14. The equivalence between this and the Bragg condition by rearranging equation (2.42) and squaring

both sides

$$\mathbf{k}^2 = (\mathbf{k}' + \mathbf{G})^2 \tag{2.43}$$

and since the magnitudes of $\mathbf{k}$ and $\mathbf{k}'$ are equal

$$k^2 = k^2 + 2\mathbf{k}' \cdot \mathbf{G} + G^2 \tag{2.44}$$

$$2\mathbf{k}' \cdot \mathbf{G} = -G^2 \tag{2.45}$$

From equation (2.13) we know that $G = 2\pi/d_{hkl}$ or an integral multiple of $2\pi/d_{hkl}$. Looking at figure 2.14 we see that $2\mathbf{k}' \cdot \mathbf{G} = 2k\sin(\alpha)$ hence

$$2k\sin(\alpha) = \frac{2\pi m}{d_{hkl}} \tag{2.46}$$

Substituting $k = 2\pi/\lambda$ we arrive at Bragg's law

$$2d_{hkl}\sin(\alpha) = m\lambda \tag{2.47}$$

2.2.3 Atomic form factor

X-rays scatter from the electrons in an atom, and the scattering of a single atom is therefore determined by the electronic structure or charge distribution $\rho(\mathbf{r})$. The scattering factor for a single atom is known as the atomic form factor and it is defined by:

$$f(\mathbf{\Delta k}) = \int \rho(\mathbf{r}) e^{i\mathbf{\Delta k}\cdot\mathbf{r}} d^3\mathbf{r} \tag{2.48}$$

For a scattering angle of zero, $\mathbf{\Delta k} = 0$, and the atomic form factor is proportional to Z, the number of electrons in the atom. It is also evident that f is the Fourier transform of $\rho(\mathbf{r})$, the charge density.

2.2.4 Structure factor

We now calculate the scattering from a unit cell where the scattering from each atom may not necessarily constructively interfere. The phase difference between two atoms in the basis is $\boldsymbol{\Delta}\mathbf{k} \cdot (\mathbf{r}_i - \mathbf{r}_j)$ and the amplitudes of the incident ray at each atom will differ by a factor $e^{i\boldsymbol{\Delta}\mathbf{k}\cdot(\mathbf{r}_i - \mathbf{r}_j)}$. The sum of the amplitudes from all the atoms in the unit cell is called the structure factor $S(\boldsymbol{\Delta}\mathbf{k})$:

$$S(\boldsymbol{\Delta}\mathbf{k}) = \sum_j f_j e^{i\Delta\mathbf{k}\cdot\mathbf{r}_j} \tag{2.49}$$

In this way, the structure factor is the Fourier transform of the charge density for the whole unit cell. Since the atomic force factor is a Fourier transform, via the convolution theorem, this is the same as the product of the atomic force factor and the Fourier transform of delta functions at the positions given by the basis. Similarly the total scattered amplitude from the crystal is then the sum of the scattering from each unit cell at all the lattice point, and is given by

$$F(\Delta\mathbf{k}) = \sum_i S(\Delta\mathbf{k}) e^{i\Delta\mathbf{k}\cdot\mathbf{r}_i} \tag{2.50}$$

As with the basis, this is like convolving the structure factor and the Fourier transform of delta functions at each lattice point.

The total intensity is the square of the total amplitude and is therefore proportional to the square of the structure factor. The structure factor alone cannot be used to calculate the absolute intensity of the Bragg peak. If the structure has a single atom basis, then the reflections will have equal intensity proportional to the square of the structure factor. For a multi-atom basis, where $S(\mathbf{G}) = 0$ there is destructive interference between the atoms in the unit cell and the Bragg

Structure	Allowed	Forbidden
cubic	any h, k, l	none
bcc	$(h + k + l)$ even	$(h + k + l)$ odd
fcc	h, k, l all even, or all odd	h, k, l mixed odd/even
cd	h, k, l all odd, or all even with $(h + k + l) = 4n$	h, k, l mixed odd/even, or h, k, l all even and $(h + k + l) \neq 4n$

Table 2.2: Selection rules for Bragg reflection for conventional unit cells of some common structures.

reflection is 'forbidden'. For example, an fcc lattice with lattice parameter a has a basis given by equation (2.4) for the conventional unit cell. The structure factor is then

$$S(\mathbf{G}) = f(e^{i\mathbf{G}\cdot 0} + e^{i\mathbf{G}\cdot\frac{1}{2}a(\hat{\mathbf{x}}+\hat{\mathbf{y}})} + e^{i\mathbf{G}\cdot\frac{1}{2}a(\hat{\mathbf{y}}+\hat{\mathbf{z}})} + e^{i\mathbf{G}\cdot\frac{1}{2}a(\hat{\mathbf{z}}+\hat{\mathbf{x}})}) \tag{2.51}$$

Substituting in $\mathbf{G}$ from equation (2.10):

$$S(\mathbf{G}) = f(1 + e^{i\pi(h+k)} + e^{i\pi(k+l)} + e^{i\pi(h+l)}) \tag{2.52}$$

$$= f(1 + (-1)^{h+k} + (-1)^{k+l} + (-1)^{h+l}) \tag{2.53}$$

$$= \begin{cases} 2f & h, k, l \text{ all even or all odd} \\ 0 & h, k, l \text{ mixed even and odd} \end{cases} \tag{2.54}$$

So for mixed even and odd h, k, l there is no Bragg reflection. The same method can be applied to bcc and cd and the selection rules are given in table 2.2. These selection rules are important for calculating which reflections are seen in a Laue diffraction pattern, described in section 2.2.6.1 and in the experimental data in this thesis.

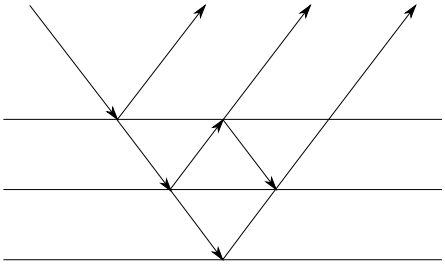


Figure 2.15: Dynamical diffraction, interference of reflected rays. The reflected ray at the Bragg angle θ makes the same angle with the next plane and will reflect again.

2.2.5 Dynamical diffraction

The x-ray diffraction theory presented thus far makes several assumptions. It is assumed that the refractive index of the crystal is very similar to the external environment. The absorption in the crystal is assumed to be negligible and that the intensity from the source is the same for each atom. The interference between the diffracted beams as illustrated in figure 2.15 is neglected. This theory is called the kinematic theory of diffraction and the full treatment which accounts for these effects is called the dynamical theory of diffraction, first developed by Darwin [29] and later by Ewald [30].

The second reflected beam in figure 2.15 has a small magnitude so it takes many layers for the effect to build up. This means that dynamical effects are most important for highly perfect single-crystals such as those used in the semiconductor industry. Most crystals are imperfect and can be thought of as a 'mosaic' structure of small crystals which have a slight variation in orientation as shown in figure 2.16. In reality the imperfection is due to defects such as the dislocations described earlier in section 2.1.6.1 so this is an oversimplification.

The mosaic blocks must be small enough for attenuation to be neglected and the kinematic theory applies. If the blocks are sufficiently mis-orientated then

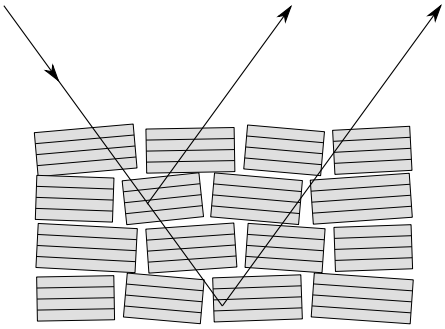


Figure 2.16: Imperfect 'mosaic' crystal.

the multiple interference effects between the blocks become negligible. Effectively the dynamical theory is only important for very large, near perfect single crystals and the kinematic theory is applicable in most cases.

The experimental work in this thesis is primarily focused on x-ray diffraction from single crystal copper. The initial dislocation densities for these single crystals were measured via TEM and found to be of order $10^8\,\mathrm{cm}^{-2}$. As described in section 2.3, during shock compression, the dislocation density and disorder in the crystal increases by orders of magnitude. Recovered samples of shocked copper, at similar pressures to those used in the experiment described in this thesis, were found to have dislocation densities of order $10^{10} - 10^{11}\,\mathrm{cm}^{-2}$ [31]. For these highly imperfect crystals we utilize the kinematic theory and neglect dynamical effects.

For the shock Laue experiment described in chapter 4, the absolute intensities of diffraction spots are not as important as their positions, and the non-ideal x-ray source would make any quantitative analysis of the absolute intensities difficult. The flat crystal spectrometer used to characterise the x-ray source uses silicon wafers which are highly perfect. The calculation of absolute intensity of the spectrum for comparison with other sources required use of the rocking curve for the crystal. This is the intensity versus angle curve for a perfect reflection.

2.2.6 Experimental diffraction geometries

Bragg's law states that if we have an x-ray of a given wavelength then diffraction (first order) is only observed at a particular angle of incidence. Therefore, to satisfy Bragg's law in an experiment, the angle must be varied at a fixed wavelength or the wavelength varied at a fixed angle. In the 'diverging beam' geometry, the wavelength is nominally fixed and the angle is varied by allowing a point source to diverge and hit the crystal at a range of angles. In the Laue method, the angle is fixed and the wavelength varied by using a polychromatic 'white-light' x-ray source.

2.2.6.1 The Laue method

This method was one of the earliest x-ray diffraction techniques, indeed, the early Laue diffraction patterns helped bear out the theories of crystal lattices as described earlier. The method is still regularly used in the laboratory, largely for orientating crystals along a desired crystallographic plane. The method is also applied to structure determination for example of protein crystals.

The Laue method is based on irradiating a stationary single crystal with a broadband x-ray source. The x-ray source is collimated and the diffracted x-rays recorded on a flat detector, typically perpendicular to the incident x-ray beam. For each (hkl) plane the spacing d_{hkl} and the angle are fixed, and the wavelength given by Bragg's law will diffract. The resulting pattern is an array of spots each at a different wavelength.

The diffraction pattern can be recorded in back-reflection or in transmission as shown in figure 2.17. The diffraction spots from planes in a zone form a cone around the zone axis which intersects the detector plane in an ellipse or hyperbola, as figure 2.17 attempts to show.

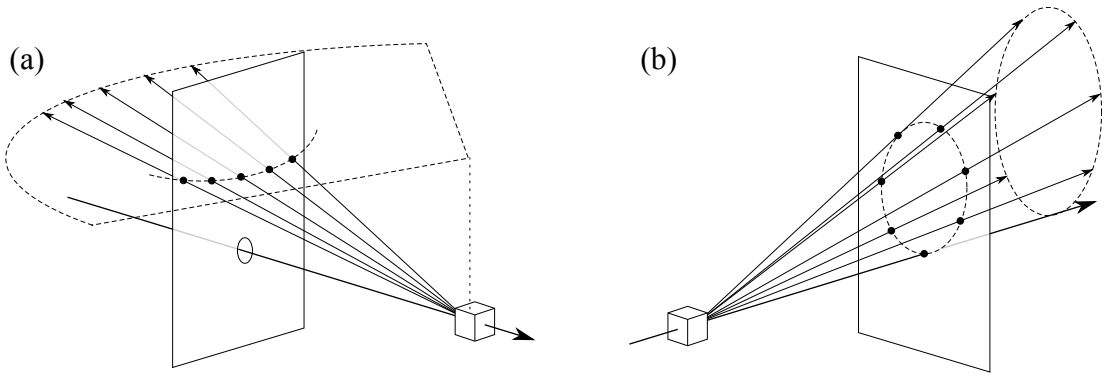


Figure 2.17: Laue method (a) in back-reflection (b) in transmission. [24]

2.2.6.2 Powder diffraction

It is worth discussing the powder diffraction method since the set-up is so similar to the Laue method already described. The powder diffraction method again uses a collimated source but this time it is monochromatic, or at least ideally monochromatic. The angle is varied by the sample itself, which is made up of randomly orientated crystallites, similar to the mosaic crystal in figure 2.16 but much more highly mis-orientated. In actual fact, most powders or polycrystals will have preferred orientations. For each lattice plane, with spacing d_{hkl}, there will be some crystallites with the correct orientation to satisfy Bragg's law and the diffraction from these planes forms a cone at an angle 2θ to the incident beam. The pattern is often recorded on a flat detector or a cylindrical film surrounding the powder sample, the recorded rings are known as Debye-Scherrer rings.

2.2.7 The Ewald sphere

It is sometimes useful to visualise the different geometries in terms of reciprocal space. The Ewald construction or Ewald sphere is the loci of points which fulfil the Laue condition and is illustrated in figure 2.19. Figure 2.19 (a) shows the Ewald construction for Bragg reflections. The sphere, or circle in 2d, has a radius

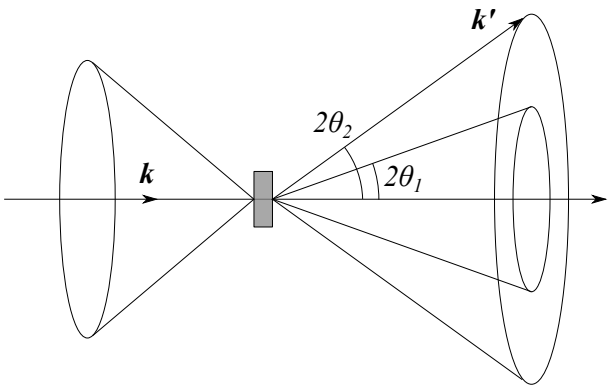


Figure 2.18: Powder diffraction geometry.

of k about $\mathbf{k}$ and intersects one lattice point, which is the only lattice point which will diffract for the incident $\mathbf{k}$ x-ray.

Figure 2.19 (b) shows the Ewald construction for the Laue method. The wavevectors $\mathbf{k}_0$ and $\mathbf{k}_1$ are the minimum and maximum wavevectors in the range provided by the x-ray source. The shaded area is the region of reciprocal space for which the Laue condition can be fulfilled and lattice points within this region produce Laue spots.

Figure 2.19 (c) is the Ewald construction for the powder diffraction geometry. The sphere is defined by the collimated monochromatic source. The random orientations of the powder produce shells in reciprocal space, effectively every orientation of the crystal at once. The intersection of the Ewald sphere with a shell is a cone and produces the Debye-Scherrer rings described in section 2.2.6.2.

2.3 Shock waves

A shock wave is usually defined as a propagating disturbance in a material, where there is a discontinuity in the pressure, density, and internal energy [32]. The discontinuity is called the shock front. In practice the shock front often has a

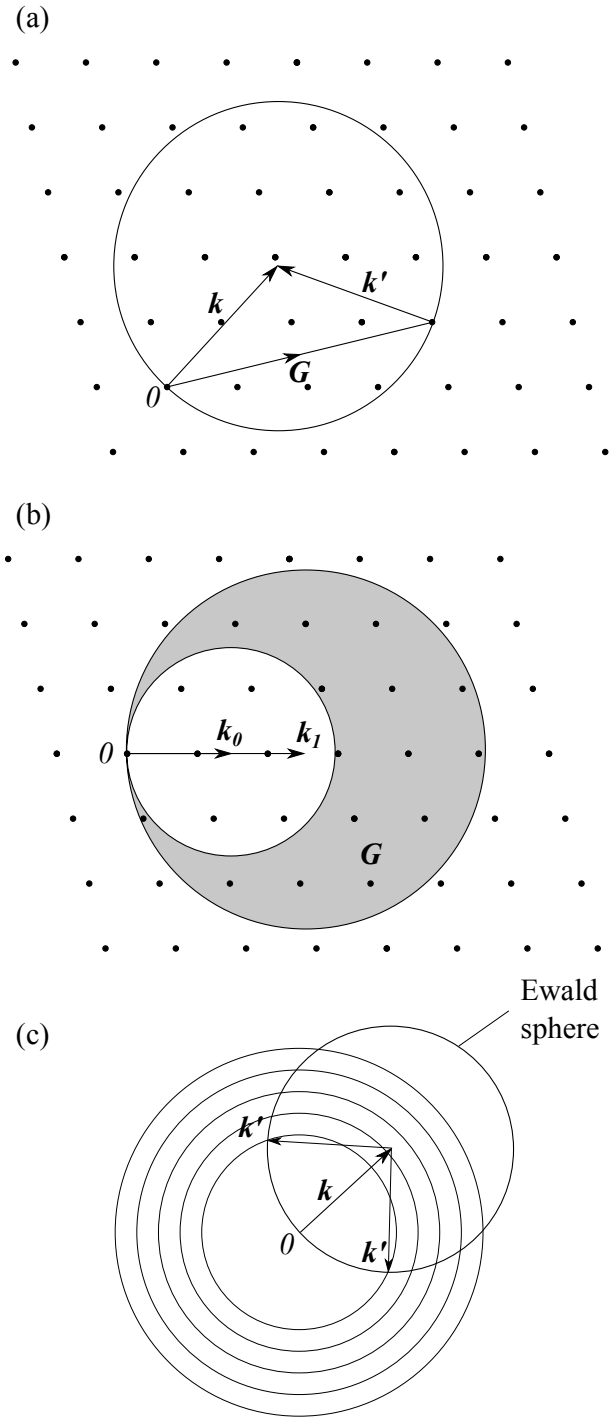


Figure 2.19: Ewald sphere constructions. (a) Bragg diffraction (b) the Laue method (c) Powder diffraction.

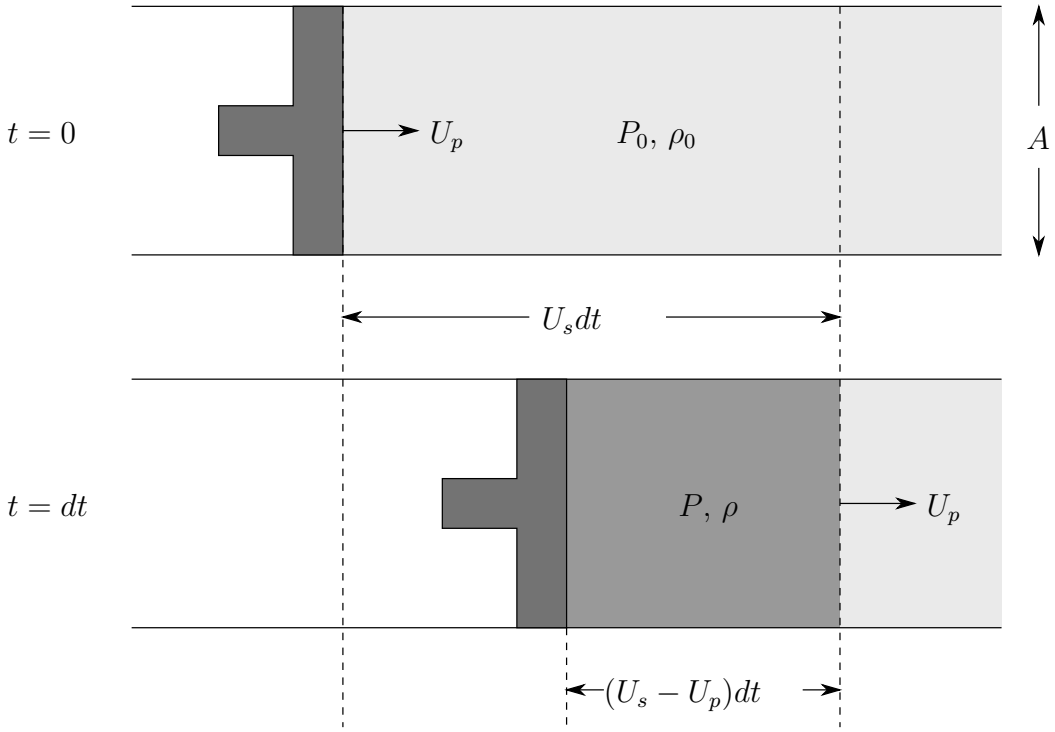


Figure 2.20: Schematic of shock wave propagation.

finite width and is not truely a discontinuity, so the precise definition of a shock is somewhat dependent on the application.

2.3.1 Rankine-Hugoniot equations

The basic equations of shock wave physics are the Rankine-Hugoniot equations [1, 2, 33]. These equations are valid for a fluid or solids where the yield strength is exceeded by the stress. They are derived by applying conservation of mass, momentum, and energy across the shock front.

If we imagine the shock being driven by a piston moving at velocity U_p and shock front having a velocity U_s as illustrated in figure 2.20. In a time interval dt, the piston moves $U_p dt$ and the shock front moves $U_s dt$. The volume of the shocked region increases by $A(U_s - U_p)dt$ and the volume of the unshocked region decreases

by $AU_s dt$, where A is the cross-sectional area. The density of the unshocked region is ρ_0 and the density of the shocked region is ρ, so for conservation of mass, after eliminating Adt

$$\rho_0 U_s = \rho(U_s - U_p) \tag{2.55}$$

Newton's second law states that the rate of change of momentum of a body is equal to the force acting on the body. In the time interval dt a mass of $A\rho_0 U_s dt$ is accelerated from zero velocity to the piston velocity U_p. The piston velocity is more generally known as the particle velocity. The impulse at the shock front is $A(P_1 - P_0)dt$ and therefore, after eliminating Adt,

$$P_1 - P_0 = \rho_0 U_s U_p \tag{2.56}$$

The work done by the piston is given by $P_1 A U_p dt$ and the kinetic energy of the shocked region is $(1/2)(A\rho_0 U_s dt)U_p^2$. If the change in internal energy is expressed as $(A\rho_0 U_s dt)(E_1 - E_0)$, where E is the internal energy per unit mass, then the conservation of energy leads to

$$P_1 A U_p dt = \frac{1}{2}(A\rho_0 U_s dt)U_p^2 + (A\rho_0 U_s dt)(E_1 - E_0) \tag{2.57}$$

$$P_1 U_p = \frac{1}{2}\rho_0 U_s U_p^2 + \rho_0 U_s (E_1 - E_0) \tag{2.58}$$

Substituting equations (2.56) and (2.55) into (2.58) and rearranging gives

$$E_1 - E_0 = \frac{1}{2}(P_1 + P_0)(V_0 - V_1) \tag{2.59}$$

where V is the specific volume given by $V = 1/\rho$. Equations (2.55), (2.56), and (2.59) are the Rankine-Hugoniot equations [34, 35] or Rankine-Hugoniot 'jump

conditions'.

2.3.2 The Hugoniot

If the form of E and E_0, i.e. the equation of state, is known then the final shocked state can be calculated using the Rankine-Hugoniot equations. For the simplest case of an ideal gas the equation of state is

$$E = \frac{PV}{\gamma - 1} \tag{2.60}$$

where γ is the ratio of specific heats at constant pressure and constant volume. Substituting into equation (2.59) and rearranging produces

$$P_1 = \frac{(\gamma + 1)V_0 - (\gamma - 1)V_1}{(\gamma + 1)V_1 - (\gamma - 1)V_0} P_0 \tag{2.61}$$

$$P_1 = H(P_0, V_0, V_1) \tag{2.62}$$

The curve defined by H is called the Hugoniot curve and is schematically shown in figure 2.21. The Hugoniot is a locus of possible shocked states, rather than the thermodynamic path taken in the P-V plane, so the material jumps from the initial state to the final state. If the material is initially at ambient pressure the Hugoniot is the principal Hugoniot. If the material is already in a shocked state then a secondary Hugoniot describes the 'reshocked' states. The line between the initial and final states is known as the Rayleigh line. Eliminating U_p from equation (2.55) and using the specific volume gives

$$U_s^2 = \frac{P_0 - P_1}{V_1 - V_0} V_0^2 \tag{2.63}$$

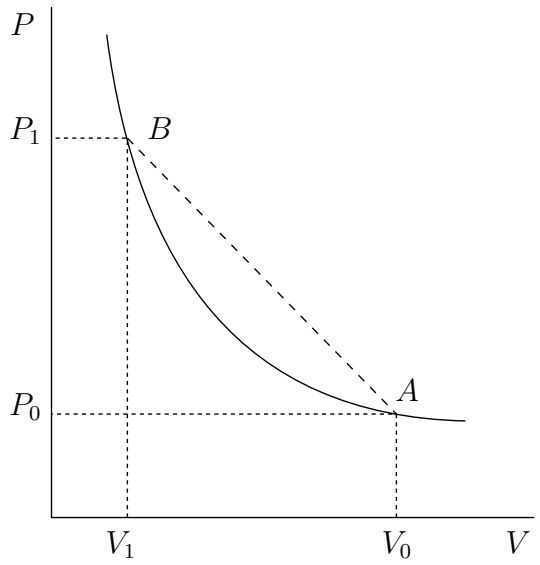


Figure 2.21: Schematic of Hugoniot curve. The initial and final states are indicated by A and B, joined by the dashed Rayleigh line. The gradient of the Rayleigh line is proportional to the square of the shock velocity U_s.

which shows how the negative of the gradient of the Rayleigh line, $(P_0 - P_1)/(V_1 - V_0)$ is related to the shock velocity U_s. Often plots of other variables, such as pressure versus U_p, are also described as Hugoniots.

2.3.3 Shock waves in solids

The Hugoniot curve in 2.21 is for a fluid. Fluids do not support shear stresses and compress hydrostatically. Solids can support shear stresses so for a shock in the z-direction, $\sigma_{zz} > \sigma_{xx}, \sigma_{yy}$. For shock waves with amplitudes below a certain threshold, the material will respond elastically, compressing uniaxially in the shock direction, then returning to the original state upon release. This threshold limit is the Hugoniot Elastic Limit (HEL).

For shocks above the HEL, the shear stresses are large enough for plastic flow and the material yields, moving from a uniaxially compressed state back towards hydrostatic compression. These shocks are often divided into two strengths,

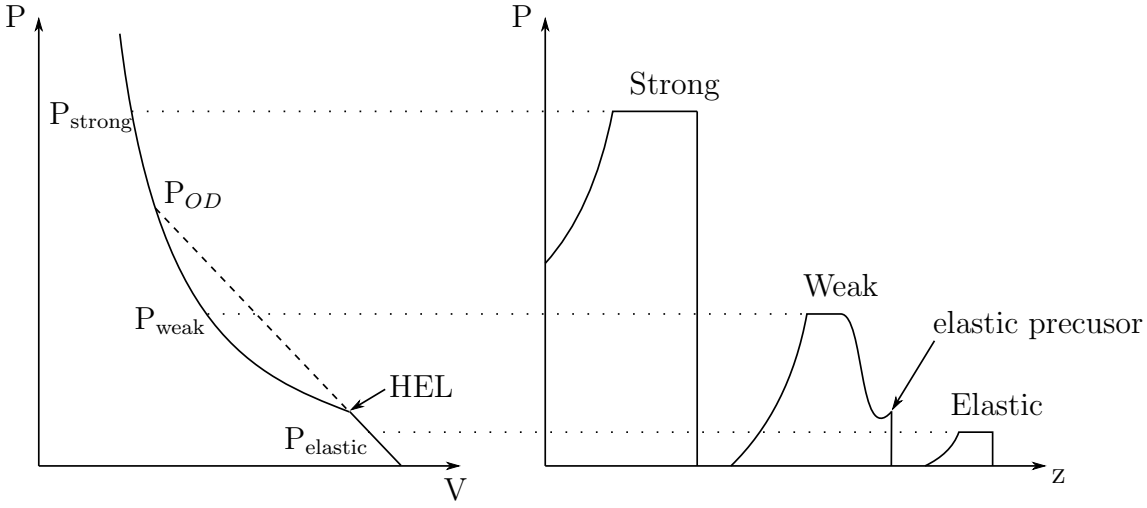


Figure 2.22: Shock Hugoniot in a solid from [36]. Idealised wave profiles for an elastic, weak, and strong shocks are shown in the right hand side, for pressure versus propagation distance. The Rayleigh line for P_{OD} has the same gradient as the elastic part of the Hugoniot and indicates the pressure above which the shock is overdriven.

'weak' and 'strong' (or overdriven). Weak shocks are characterised by a two wave structure where an elastic precursor wave, encompassing an elastically compressed region, is followed by the subsequent plastic wave as the material yields. In the strong shock case the elastically compressed region is so small that the material effectively jumps straight to the plastically deformed state. Figure 2.22 illustrates the transition from weak to strong shocks.

The wave profiles in figure 2.22 are somewhat idealised. In reality the HEL is often much lower than the typical shock pressures and can be difficult to pick out. In single crystals the HEL is dependent on the orientation of the crystal with respect to the shock direction and pre-existing defects act to lower the HEL as plastic deformation occurs more readily. The wave profiles have a finite lifetime. The length of the plateau at the highest pressure is dependent on the impact pulse length, which is related to the impactor width in plate impact experiments, or the laser pulse length in laser-driven shock experiments. When the pressure

is released, a rarefaction wave passes through the compressed material and the pressure reduces back to ambient.

The shock is described as 'steady' if the wave profile is time-independent, simply moving along at the shock velocity. For weak shocks the whole wave profile is often not steady as the elastic and plastic waves generally have different velocities. The elastic and plastic waves taken individually may be steady however.

2.3.4 Dislocation models

Plastic deformation at low strain rates occurs via the glide and multiplication of pre-existing dislocations in the crystal. Under the high strain rates involved in shock compression the large increase in dislocation density suggested by Orowan's equation (eq:orowan) requires the generation of new dislocations at or behind the shock front, which then flow and relieve the stress towards the hydrostat.

A number of theoretical models have been proposed for the mechanism by which dislocations are nucleated at the shock front. The first attempt, by Smith [37], depicted the shock front as a moving array of edge dislocations which accommodate the change in lattice parameter between the uncompressed and compressed regions, see figure 2.23. Smith's model was modified by Hornbogen [38], so that there are dislocation loops with edge components at the shock front, as in the Smith model, and screw components left behind in the compressed region.

One problem with these models is that since the dislocations are at some angle with respect to the shock direction they would have to travel at supersonic velocities. Meyers revised the model to address this issue, proposing that the dislocations nucleated at the front move at subsonic speeds and are left behind by the shock front. Then as the shock front propagates new arrays of dislocations are periodically generated [40], as shown in figure 2.23. The model proposed by

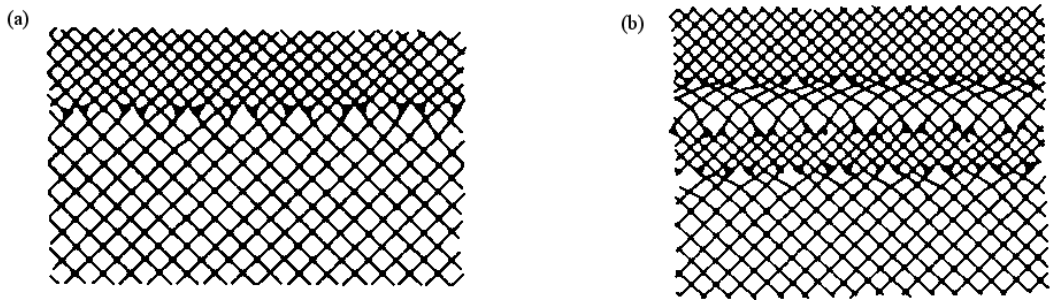


Figure 2.23: Shock dislocation models. (a) Smith and (b) Meyers models for dislocation generation at the shock front. Reproduced from [39]. The shock direction is down the page. The dislocations are edge dislocations and the planes are {111} type.

Weertman is a mixture of the Smith and Meyers models. Supersonic dislocations travel with the shock front and subsonic dislocations are periodically generated and left behind. The dependence on supersonic dislocation is based on theory that dislocations can be supersonic if they are created at those velocities [41].

An alternative model by Zaretsky is based on the generation of stacking faults and multiplication of the partial dislocations which bound them [42]. The model proposes that a segment of partial dislocation, that is pinned at two points, bows out under shear stress and rapidly emits new intrinsic stacking faults as described in section 2.1.6.2. This process with dislocation climb leads to a structure of stacking faults and thinned twinned regions, which have been observed in recovered shocked samples.

All of these models require dislocation densities which are several orders of magnitude greater than the observed dislocation densities in recovery experiments [43]. The Zaretsky and Meyers models attempt to address the discrepancy, proposing that the generated dislocations annihilate with each other under rarefaction when the sample is released. In the Meyers model, dislocations are created in pairs with equal and opposite Burgers vectors facilitating this annihi-

lation.

2.4 Molecular dynamics simulations

Molecular dynamics (MD) is a method of simulating atoms or molecules which has been around since the early days of computing [44]. As computing technology has advanced so has the ability to simulate larger and more realistic systems. The trajectories of all the atoms in a simulation are tracked and this lends itself to predicting x-ray diffraction patterns. It is a deterministic technique in that given the initial positions and velocities of the atoms, the final time evolution is in principle determined.

The principle behind MD is numerically solving the equations of motion for a number of particles and integrating over time. The equation of motion is given by Newton's second law.

$$\mathbf{F}_i(\mathbf{r}_1, \mathbf{r}_2, \ldots, \mathbf{r}_N) = m_i \frac{d^2\mathbf{r}_i}{dt^2} \tag{2.64}$$

The forces $\mathbf{F}_i$ between the particles are calculated using an inter-atomic potential[1], designed to mimic the properties of the material being simulated. The positions and velocities of the particles are then updated using a chosen numerical integration algorithm. The third ingredient required is the initial and boundary conditions.

Another constraint on a simulation is which quantities are conserved. The simulations in this thesis were carried out using the microcanonical ensemble, or NVE ensemble, where the number of particles (N), the volume (V), and total

[1] the forces can be calculated using quantum mechanics in so called Quantum MD (QMD), however this is much more computationally demanding

energy (E) are conserved. The other common ensembles are the NVT (number, volume, temperature) and the NPT (number, pressure, temperature) ensembles, where a thermostat and/or barostat is applied to add or remove energy to control the temperature and pressure. These ensembles are appropriate for simulating systems in equilibrium, for example where a larger heat bath dissipates energy. For this reason, simulations using the NVE ensemble are often referred to as non-equilibrium molecular dynamics (NEMD) simulations.

2.4.1 Potentials

As stated earlier, the inter-particle forces are calculated using a potential function, which is clearly crucial to behaviour of the simulation. The development of accurate potentials is an area of active research with increasingly sophisticated and complicated potentials being developed. The simplest potentials are based on pairwise interactions where the force is dependent only on the distance separating two particles. The resultant force on a particle is the sum of the pairwise forces between it and all the other particles. One of the oldest and most widely used potential of this sort is the Lennard-Jones (LJ) potential, given by

$$\phi_{LJ}(r) = 4\epsilon \left[\left(\frac{\sigma}{r}\right)^{12} - \left(\frac{\sigma}{r}\right)^{6} \right] \tag{2.65}$$

where r is the distance between two particles $|\mathbf{r}_1 - \mathbf{r}_2|$. The parameter ϵ controls the depth of the potential well and σ is the value of r at $\phi = 0$, and also controls the separation distance for the minimum, at $r_m = 2^{1/6}\sigma$. The potential is based on van der Waals forces, with the $(\sigma/r)^{12}$ repulsion term dominating at small distances, and the attractive $(\sigma/r)^6$ term dominating at large distances. This means that it will model closed shell systems such as the noble gases quite well.

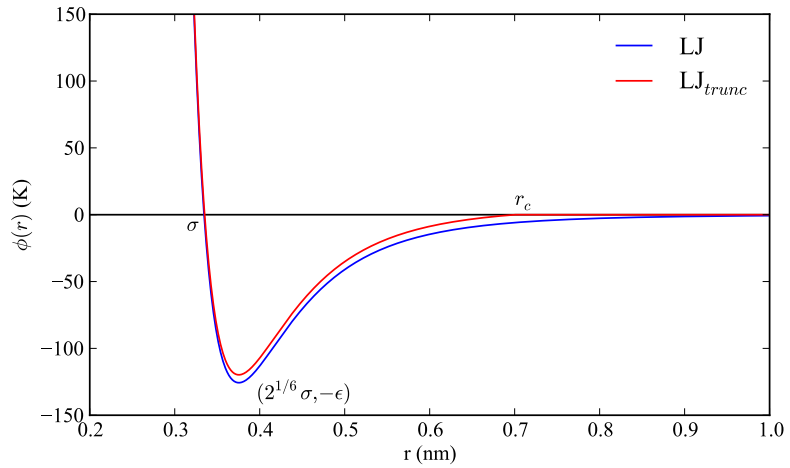


Figure 2.24: The Lennard-Jones potential. In this case, $\epsilon/k_\mathrm{B} = 125.7$, $\sigma = 0.3345\,\mathrm{nm}$, parameters for Argon [45]. The truncated form is also shown, with $r_c = 0.7\,\mathrm{nm}$.

The potential is often truncated such that the force on an atom is only dependent on its neighbours within a certain cut-off distance. To remove the discontinuity in the potential at the cut-off r_c, the potential is shifted such that

$$V_{LJ-trunc}(r) = \begin{cases} V_{LJ}(r) - V_{LJ}(r_c) & \text{for } r < r_c \\ 0 & \text{for } r \geq r_c \end{cases} \tag{2.66}$$

For metallic and covalently bonded materials, the two-body interaction used by the LJ potential is not sufficient, and although it will produce a close packed solid structure such as fcc, other structures such as bcc are energetically unfavourable. To model these systems, many-body effects must be incorporated. The embedded atom method (EAM) potential is one such many-body potential which is widely used for metallic systems [46]. The potential is of the form

$$V = \frac{1}{2}\sum_{i\neq j}^{N}\phi(r_{ij}) + \sum_{i=1}^{N}U(n_i) \tag{2.67}$$

where $\phi(r)$ is the pairwise component and $U(n)$ is the many-body part. The function U is called the embedding function and acts on n given by

$$n_i = \sum_{j \neq i}^{N} \rho(r_{ij}) \tag{2.68}$$

where $\rho(r)$ is the electron charge density summed from the neighbour atoms within a cut-off distance. The general effect is that when the density is higher the attractive (e.g. van der Waals) force becomes weaker. The added complexity of the calculation increases the compute time over more simple potentials like the LJ potential discussed earlier. The simulations of copper in this thesis make use of the EAM potential of Mishin *et al* [47], whilst for the tantalum simulations another many-body potential, the extended Finis-Sinclair (EFS) potential of Dai *et al* is used [48].

2.4.2 The LAMMPS code

The MD simulations in this thesis were carried out using the LAMMPS code (Large-scale Atomic/Molecular Massively Parallel Simulator) developed at Sandia National Laboratories [49]. As the name suggests, it is well developed for doing large scale simulations involving up to billions of atoms on large numbers of processors in parallel.

LAMMPS implements the velocity Verlet algorithm for time integration [50].

At each step the positions and velocities are calculated as follows

$$\mathbf{r}(t + \Delta t) = \mathbf{r}(t) + \mathbf{v}(t)\Delta t + \frac{1}{2}\mathbf{a}(t)\Delta t^2 \tag{2.69}$$

$$\mathbf{v}(t + \Delta t/2) = \mathbf{v}(t) + \frac{1}{2}\mathbf{a}(t)\Delta t \tag{2.70}$$

$$\mathbf{a}(t + \Delta t) = -(\nabla V/m)\mathbf{r}(t + \Delta t) \tag{2.71}$$

$$\mathbf{v}(t + \Delta t) = \mathbf{v}(t + \Delta t/2) + \frac{1}{2}\mathbf{a}(t + \Delta t)\Delta t \tag{2.72}$$

This is more memory efficient than the standard Verlet algorithm where the positions and velocities for each particle must be stored for two consecutive timesteps. The error is of order $O(\Delta t^4)$ and the timestep is chosen such that this error is small compared to the change in position, for our simulations this is typically a femtosecond.

The simulation parameters and initial conditions are specified in a script of commands. This includes the specification of the boundary conditions. Often MD simulations are run with periodic boundaries. The particles at the faces of the simulation box interact over the boundary with particles on the opposite face. The other standard boundary style is shrink-wrapped, i.e. the boundary is non-periodic and expanded to encompass the particles in that direction. MD simulations of shocks typically employ periodic boundaries in the directions transverse to the shock direction and a shrink-wrapped boundary in the shock direction.

At each time step, LAMMPS can compute any number of per atom or global quantities. One such per atom quantity which is regularly used for simulations where a crystal structure is present is the centro-symmetry parameter (CSP) as it is a measure of local lattice disorder.

2.4.2.1 Centro-symmetry parameter

The CSP is calculated using the formula given by Kelchner *et al* [51]

$$CSP = \sum_{i}^{N/2} |\mathbf{r}_i + \mathbf{r}_{i+N/2}|^2 \tag{2.73}$$

where there are N neighbour atoms and $\mathbf{r}_i$ and $\mathbf{r}_{i+N/2}$ are vectors from the central atom to two different neighbours. The value of $|\mathbf{r}_i + \mathbf{r}_{i+N/2}|^2$ is computed for all the neighbours and the $N/2$ lowest values summed. The number of neighbours N can be varied for different lattice types, for an fcc lattice N is set to twelve, and for bcc it is set to 8. For a perfect lattice the resulting CSP= 0.

2.4.3 Simulating diffraction from MD

At each time step in an MD simulation the positions of the atoms are well known, and it is then possible to post process the output to produce a diffraction pattern. Representing the atoms as delta functions the intensity at $\mathbf{q}$ is given by

$$|F(\mathbf{q})|^2 \propto \left| \sum_{j}^{N} \exp(i\mathbf{q} \cdot \mathbf{r}_j) \right|^2 \tag{2.74}$$

where $\mathbf{r}_j$ is the position of the jth atom, summed over N atoms. This is the discrete Fourier transform. The 'fast Fourier transform' technique can be applied to MD, but in the work shown here the discrete form is used, for more details see Kimminau *et al* [52].

Chapter 3

Nanosecond white-light Laue technique

This chapter describes the design and development of a nanosecond white-light Laue method for investigating *in situ* microstructure under shock compression.

3.1 Background

Time-resolved X-ray diffraction (TXRD) methods for studying shock waves were first developed in the 1980s and have been used succesfully to observe several phenomena in shock compressed materials [12, 14, 53, 54, 55]. The driving force behind the development of these techniques is to understand the lattice level dynamics during the shock compression of condensed matter. The timescales and extreme conditions involved make measurements difficult and despite several decades of research there is much remaining to discover.

Several different TXRD methods have been developed and employed in shock experiments, but perhaps the most successful has been the so-called diverging

beam geometry [54]. In this set-up, a monochromatic x-ray source is produced close to the driven target, which must be a single-crystal. The diverging x-rays diffract from multiple planes and are recorded on a large solid angle detector as diffraction arcs. Fitting the pattern gives a direct measurement of the lattice plane spacings during the shock as well as indicating potential phase changes with the appearance of new diffraction arcs. Another x-ray diffraction technique which has been applied to shock waves is the Debye-Scherrer method for polycrystalline materials [56]. It has also been demonstrated that a quasi-white beam ($\Delta\lambda/\lambda \approx 0.15$) can be used at a high photon energy to produce Laue patterns of shocked single crystals [57].

The different geometries provide different information. For the diverging beam technique the Bragg condition is satisfied for the diffracting planes in different regions of the crystal. As the lattice undergoes elastic and plastic deformation the plane separations are altered and a different curve on the crystal satisfies the Bragg condition, resulting in the shift of the peak. In the Laue technique a large region of reciprocal space is interrogated, see the Ewald sphere in section 2.2.7. In the Laue method the diffracting region is the same throughout and the energy of the diffracting x-ray changes to satisfy the Bragg condition. It is therefore sensitive to changes in orientation of the reciprocal lattice vectors and directional broadening of the peaks in reciprocal space, due to defects in the lattice [24, 58, 59]. Despite the fact that this technique has proven successful in the analysis of dislocation structures [60, 61], especially using x-ray microbeams and static samples, there have been few attempts at making *in situ* measurements in the shock regime [22, 57, 62]. In the diverging beam geometry the peaks are swept into a line and the directional information about the defects is lost. The disadvantage of the Laue method is that it fails to directly determine the inter-

Wavelength	1053 nm	527 nm
Pulse duration	0.35-20 ns	0.35-20 ns
Energy	Up to 1 kJ	Up to 500 J
Spot size at best focus	20 μm	20 μm
Spot size with phase plates	200-1000 μm	200-1000 μm
Rep rate	2/hr	2/hr

Table 3.1: Nominal beam specification for the Janus laser for 1053 nm and when frequency doubling at 527 nm (jlf.llnl.gov)

planar spacing and hence the absolute strain which is a significant disadvantage.

3.2 The JANUS laser

Our development of the white-light Laue technique for shock experiments has predominantly taken place at the Jupiter Laser Facility at Lawrence Livermore National Laboratory in the US, using the Janus laser. Some preliminary shots were made using the Vulcan laser at the Rutherford Appleton Laboratory (RAL) in the UK, and subsequent shots have taken place on the Omega laser at the Laboratory for Laser Energetics (LLE) at Rochester NY.

The Janus laser is a two beam, Nd:YAG laser ($\lambda = 1053$ nm), with each beam nominally capable of 500J. The beams are independent with available pulse lengths between 1 ns and 20 ns with some limited pulse-shaping capability. The two beams are designated 'east' and 'west' although the east beam is on a rotatable arm allowing it to enter the chamber at a range of positions. The optimal beam parameters are listed in table 3.1. The repetition rate for the laser, limited by the cooling time, is approximately two shots per hour. In practice however, one of the beams is shared with the adjacent Titan target area, where it acts as the long-pulse beam, reducing the typical shot rate to one per hour at best.

The target areas, where the experiments are performed, are separated from

the laser system, which is controlled by facility staff. Our experiments were performed in Target Area 1 (TA1), shown in figure 3.1. The two beams enter the room through the ceiling and are periscoped down into the target vacuum chamber, which is cylindrical with a diameter of 80cm and 90cm in length. The west beam, as labelled in figure 3.1, is fixed in position, and in our set-up the east beam was positioned at port angled at 27° to the west beam. Prior to beam alignment and full experimental shots the chamber was pumped down to a pressure of order 10^{-4} Pa. The beam lines are maintained at vacuum and gate-valved to the target chamber. When everything is ready for the shot, a designated target area operator does a sweep, ensuring no one is left inside, and locks the area, before calling through to the laser bay and requesting the shot.

3.3 Experimental design and development

3.3.1 X-ray source

X-ray diffraction experiments investigating shocks have typically employed methods which require monochromatic x-ray sources [7, 54, 56, 63]. In laser generated shock experiments, the most widely used method is to irradiate a metal foil, known as a backlighter, with a high intensity pulse (e.g. $10^{16}\,\mathrm{Wcm^{-2}}$), to produce a highly ionised plasma. This plasma produces bright emission in spectrally well defined lines which can are then used as quasi-monochromatic sources. In most cases, the resonance emission from He-like ions, known as He-α, is used as the efficiency of conversion from optical to x-ray radiation is relatively high (of order 0.1%) [64]. The choice of backlighter element controls the energy of the source.

The Laue method requires a polychromatic or 'white' x-ray source. We used

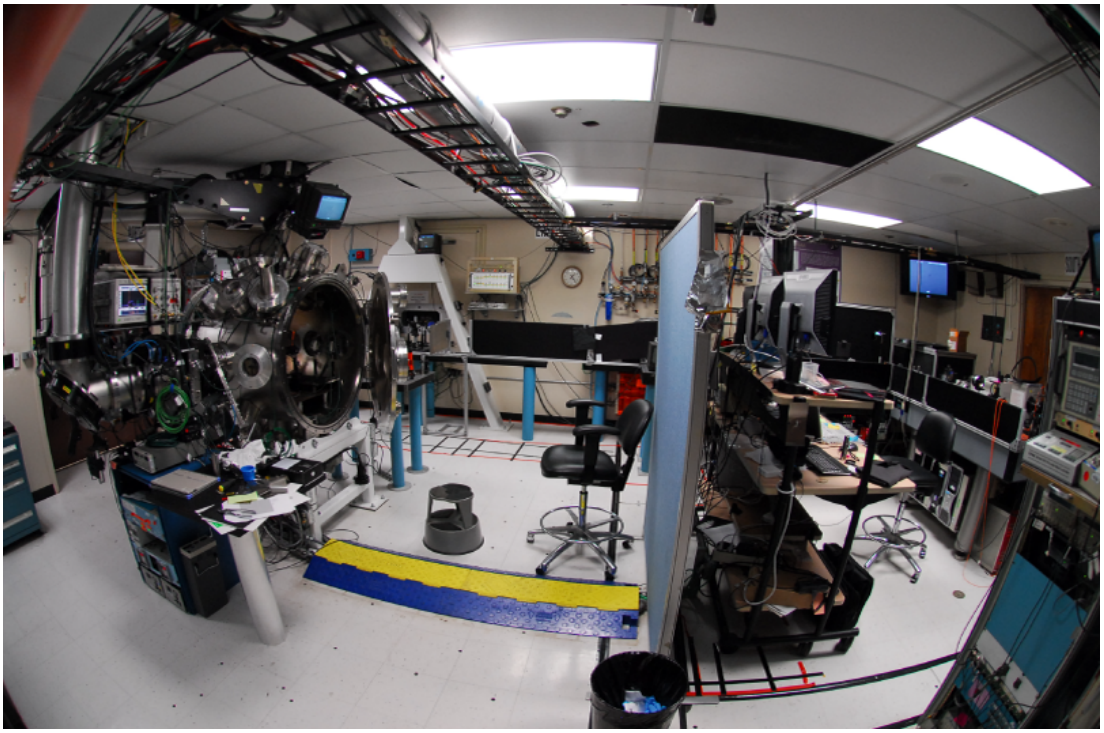


Figure 3.1: Target Area 1 (TA1), one of the target areas for the Janus laser at the Jupiter Laser Facility. To the left side of the image is the target vacuum chamber with the west beam line piping down from the ceiling. The area to right is used for setting up and controlling the experiment. The beam for the VISAR system enters through the wall on the far side of the chamber and passes to the VISAR which is in the far right corner of the room as seen in this image. The area is cleared of personnel during system shots. Image from jlf.llnl.gov

a multi-layered foil of different elements or compounds, the idea being to overlap the spectral lines and broad emission from each element and produce a quasi-white light source [62]. The foil was produced by coating 300 nm-thick layers onto a 10 μm plastic film which acts as a support[1]. The constituent elements were V^{23}, Ti^{22}, Pd^{46}, Ag^{47}, Sn^{50}, CsI, and Sm^{62}. As well as the K-shell, He-α, and Ly-α radiation described above, transitions from the L-shell and M-shell from the higher-Z elements produce broad-band radiation which smooths out the spectrum. The lower-Z elements, Ti and V, were designed to act as spectral traces to aid calibration of the spectrum, as they are expected to be stripped of all but one or two electrons and emit strongly in the He-α and Ly-α lines of known energy. The elements were coated with increasing Z, and the backlighter mounted with the plastic film support on the opposing side to the incident laser. The x-rays are collimated (details in section 3.3.4) on the plastic film side and x-rays from the top layer pass through the remainder of the foil before reaching the target crystal. Ordering the elements in this sequence was intended to reduce the absorption of x-rays from each layer by the remaining layers.

As with the more standard He-α backlighter, this mixture could be tailored, to some degree, for a given spectral range. For experiments on copper, a range from 3-8 keV is sufficient, but for higher-Z materials such as tantalum, higher energies may be required. The addition of more high-Z elements to the backlighter mixture would help with this. The coating properties of each element are a limitation, in our mixture it was found that Sn caused the foil to delaminate and disintegrate. This meant that great care had to be taken when cutting and mounting the backlighter. It was also a concern that the bits of the foil would flake off whilst the target chamber was pumping down.

[1]The backlighter foil was produced by the the Target Fabrication group at RAL

Using a laser-plasma as an x-ray source will always introduce added complexity in comparison to smoother, more ideal, polychromatic synchrotron source for example. The mixed metal foil produces a highly structured x-ray spectrum. It was important to characterise the spectrum for several reasons.

Initially, we needed to confirm that we were generating a quasi-white light source in the desired wavelength range, for copper and silicon we were aiming for energies in the 3-8 keV range, and ensure that there weren't too many 'holes' in the spectrum. Although it would not be possible to adapt the foils, and hence the x-ray source, during the experiment, additional layers could be added to the foil in future experiments to fill in any gaps, especially if there was a deficiency in x-rays at the energy corresponding to diffraction from an important peak. In addition to finding holes in the spectrum, interpreting the brightness of the diffraction peaks requires calibrating the spectrum. Since we are interested in the scattering around the peaks of the unshocked crystal, we need to know if that peak lies in a bright peak or broad region of the spectrum, and hence why we can or can't see diffuse scattering around that peak.

A spectrometer was required for assessing the x-ray yield on each shot. The x-ray yield was optimised by varying the spot size of the backlighter beam. It is difficult to control this parameter with a great degree of precision. Spot size is controlled by driving the focussing lens out of focus. The lens brought to best focus by viewing the spot of a 10Hz alignment beam on a monitor, and driving until the tightest spot is achieved. In our set-up, the backlighter foil is mounted on the diffraction box and cannot be positioned reproducibly with enough precision for the best focus position to be precisely maintained from shot-to-shot. This method of finding best-focus introduces significant human judgement and the great degree of uncertainty into the distance of defocussing and therefore the

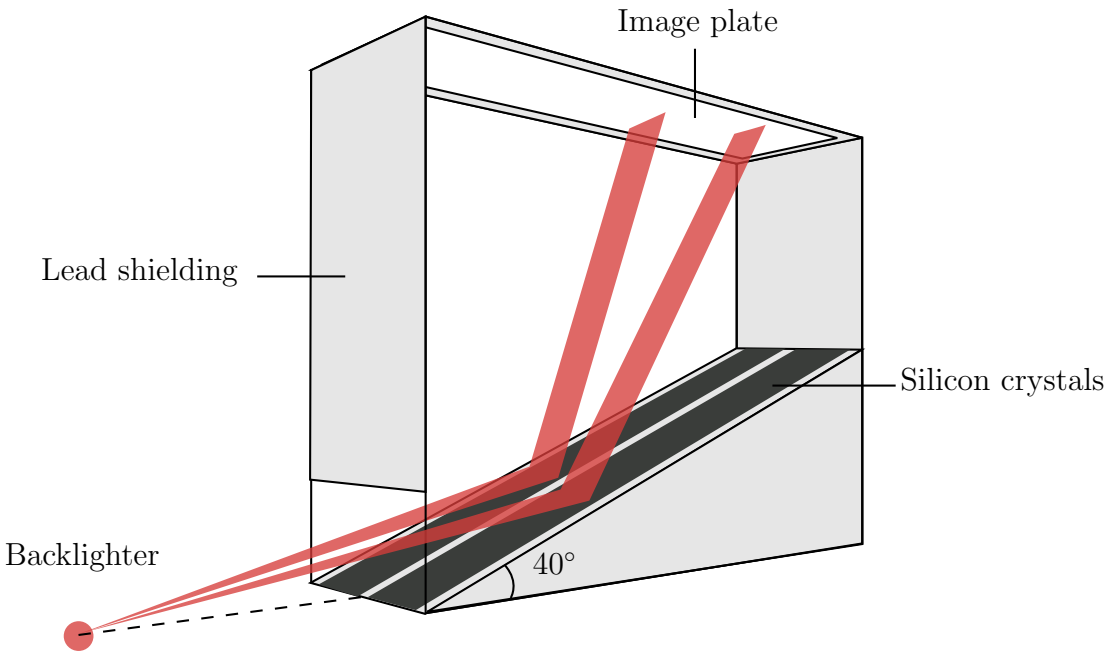


Figure 3.2: Schematic diagram of the flat crystal spectrometer used to record the x-ray source spectrum. The two silicon wafers were orientated with surface normals in the [111] and [220] crystal directions. The horizontal distance from the backlighter to the front edge of the crystal was 50 mm and the angle set at 40° giving a spectral range of 3 - 7 keV. There is some overlap between the spectral range of each crystal which allows the exact position of the source to be calculated for calibration.

spot size. In addition to this, there is some variability, of order 10-30 J, in the energy delivered by the laser relative to the requested energy.

The spectrometer was of fairly simple design, consisting of two silicon wafers angled at 40° to the horizontal with a strip of image plate detector (figure 3.2). The two silicon wafers had different surface normal orientations, [111] and [220], allowing a greater wavelength range to be recorded. The two reflected spectra can be used to calibrate the position of the spectrometer relative to source. The spectrometer was placed as close as possible to the backlighter to maximize the solid angle and therefore the spectral range. This distance was typically 50mm, any closer and the spectrometer box would impinge on the backlighter beam path.

3.3.2 Target design

The Laue technique is only applicable to single crystals. In order to use VISAR it is necessary to use 'thin' crystals, typically 5-50 μm thick as the shock wave decays as it propagates through the crystal. The copper crystals used in these experiments are grown to $\sim$10 μm thick via vapour deposition, this is much thicker than crystals normally grown using this method [1]. The crystals are grown on a $\sim$ 2 mm thick NaCl substrate, which can be removed simply by dissolving, however, the thin crystals tend to curl up when detached ruining them. The substrate was not removed for the majority of shots for this reason. For thicker crystals, a single crystal is slowly drawn from molten metal to produce a rod, known as the Czochralski method[2]. The rod is then cut using spark erosion into discs of $\sim$ 2 mm thickness, which are then electro-polished.

The copper crystals were coated with an ablation layer of parylene-N plastic

[1] Thin copper single crystals were grown by the thin film facility at the University of Aarhus, Denmark.

[2] single crystal copper rods were produced by Accumet materials

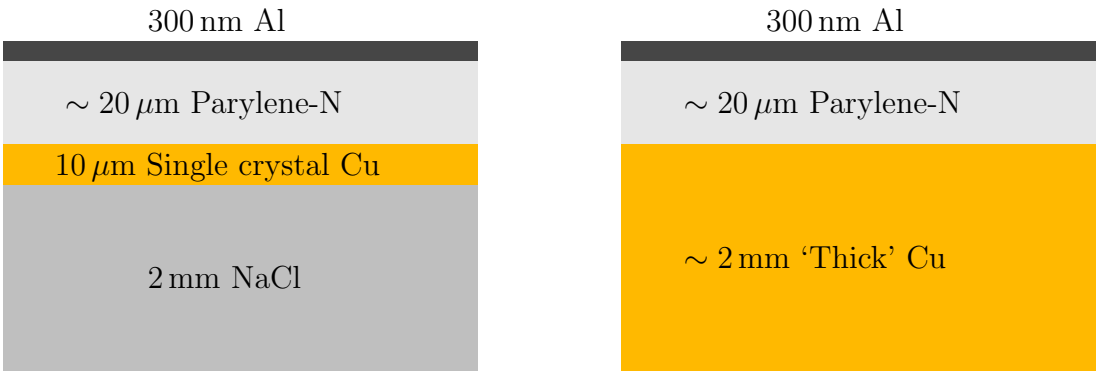


Figure 3.3: 10 μm single crystal Cu and 'thick' single crystal Cu targets.

(20 μm) and 300 nm coating of aluminium, see figure 3.3. The surface of this ablation coating is rapidly heated by the drive laser pulse, forming a plasma which expands, with the reaction force driving a shock wave into the remaining plastic. The shock wave steepens as it propagates through the plastic ideally forming a sharp planar shock front before reaching the single crystal. The aluminium flash coating is designed to absorb the laser pre-pulse and prevent preheating of the crystal before the plasma is formed. This method of 'direct drive' is well established and has been utilised in many laser-driven shock experiments [7].

3.3.3 Image plate and filtering

We used Fujifilm image plate as the detector for both the x-ray diffraction diagnostic and the crystal spectrometer. Image plate (IP) has largely replaced photographic film in laser-based x-ray experiments because of a number of advantages; it is reusable, it is not sensitive to light until exposed to x-rays, and it does not require chemical development. The ability to cover a large solid angle and to cut as required (i.e. beam apertures) are two advantages over the use of x-ray CCD cameras. For these experiments where each shot must be carefully prepared, the IP scanning time is not a limiting factor, unlike a synchrotron or

free electron laser experiment when a CCD is highly advantageous.

Fujifilm IP is based on photo-stimulated luminescence (PSL) from a layer of phosphor crystals BaF(Br,I):Eu^{2+}) contained by layers of plastic, mylar, and a magnetic backing layer. Absorbed X-rays ionise Eu^{2+} in the phosphor layer producing a metastable state. The image is read out using a flat bed scanner (FLA7000) which irradiates the IP with a red laser (632.8 nm) causing the reduction of Eu^{3+} back to Eu^{2+}, and the emission of blue light ($\sim$400 nm) which is collected by photo-multiplier tubes and recorded to produce a digital image [65].

Normal room light will erase the image so the plates are kept light-tight using Kapton film (polymer) and transferred to a light-tight box prior to scanning. Dark room conditions are not required as with photographic film. There is an associated fade rate for the IP which depends on several factors such as x-ray energy, temperature, scanner type with a two component exponential decay. There is an initial fast relaxation with a lifetime of order 20 minutes, after which fade time is of order 600 minutes [66]. For the diffraction diagnostic the absolute intensity was not of great importance, however for the crystal spectrometer, a calculation of x-ray yield was important for comparison with other x-ray sources. The plates were scanned close to 20 minutes after exposure, allowing time for the chamber to re-pressurise and the initial fast fade time.

The IP we use is designed for hospital radiography and comes in a standard size. The edges of each plate are pressed and heat sealed and the plates are not meant to be cut, however, this is a necessity for our experiments. The active layer is prone to leaking from the unsealed edges and can produce artefacts in the scanned image around cut edges. Damage to the plastic coating and debris from the shocked target also produces artefacts in the image and these will be evident in data presented later.

Selecting the correct filtering for the Laue method is arguably more difficult than for monochromatic experiments where the filter can be chosen with a K-edge close to but greater in energy than the desired He-α energy, filtering out the higher energy bremsstrahlung radiation. For the Laue method, the aim is to filter out the noise generated by the drive at the target without too much attenuation of the diffraction signal. The filter also acts as a debris shield and provides light-tightness. For copper crystals, the lowest energy diffraction spot was typically around 4 keV. Polycarbonate filtering has a low transmission for X-rays below 3 keV and thickness of 250 μm was predominantly used. An additional 25 μm layer of aluminized mylar was added for light-tightness.

3.3.4 Experimental set-up

The first experiment in this campaign made use of the polycrystalline camera described in Hawreliak *et al* [56, 67]. The camera was modified with a flat plate to support the image plate in direct back reflection rather than use the existing cylindrical holder, a schematic is shown in figure 3.4. For later experimental runs the target was completely enclosed, improving the shielding and reducing background noise.

The target crystals were mounted between two steel washers and held in purpose made target mount and goniometer stage, shown in figure 3.6. The mount could be reproducibly removed and replaced on the goniometer stage between shots. Small adjustments were made using the goniometer to normalise the rear surface to the VISAR beam, monitoring the image from the output beam splitter of one of the VISAR beds. Once the target was aligned the image plate box was lowered into position.

The backlighter foil was mounted on a copper aperture which was loaded

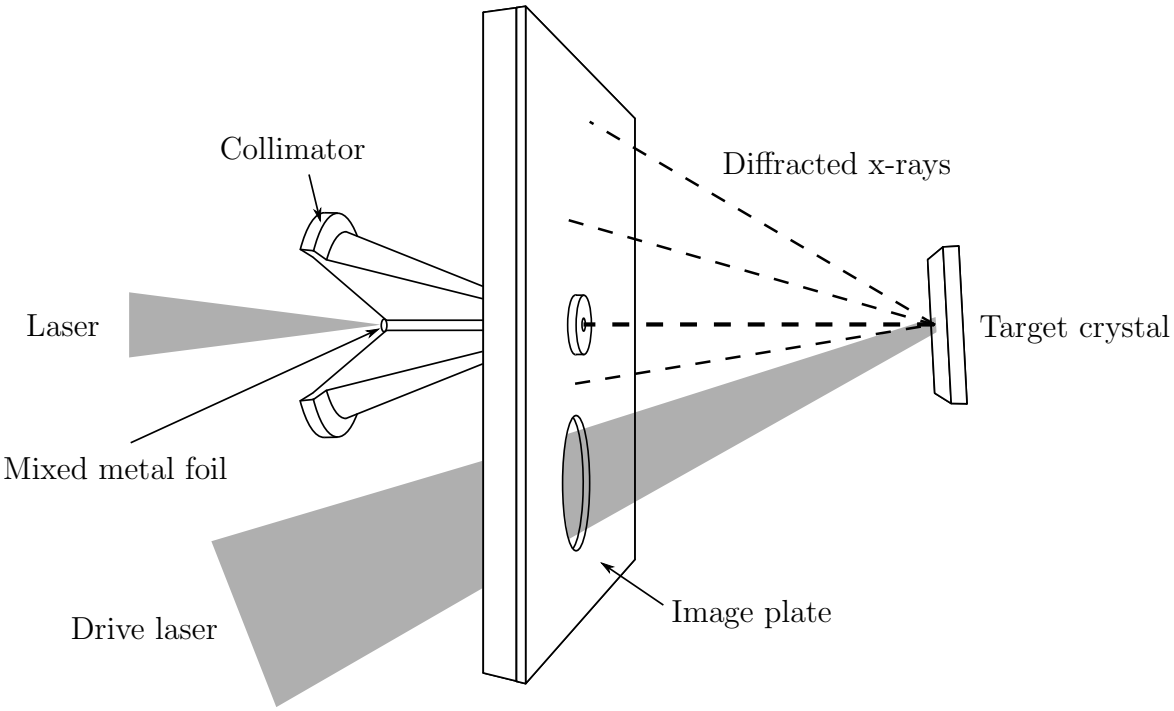


Figure 3.4: Top down view of the experimental set-up. Only the image plate in direct back reflection is shown. Figure is from [22].

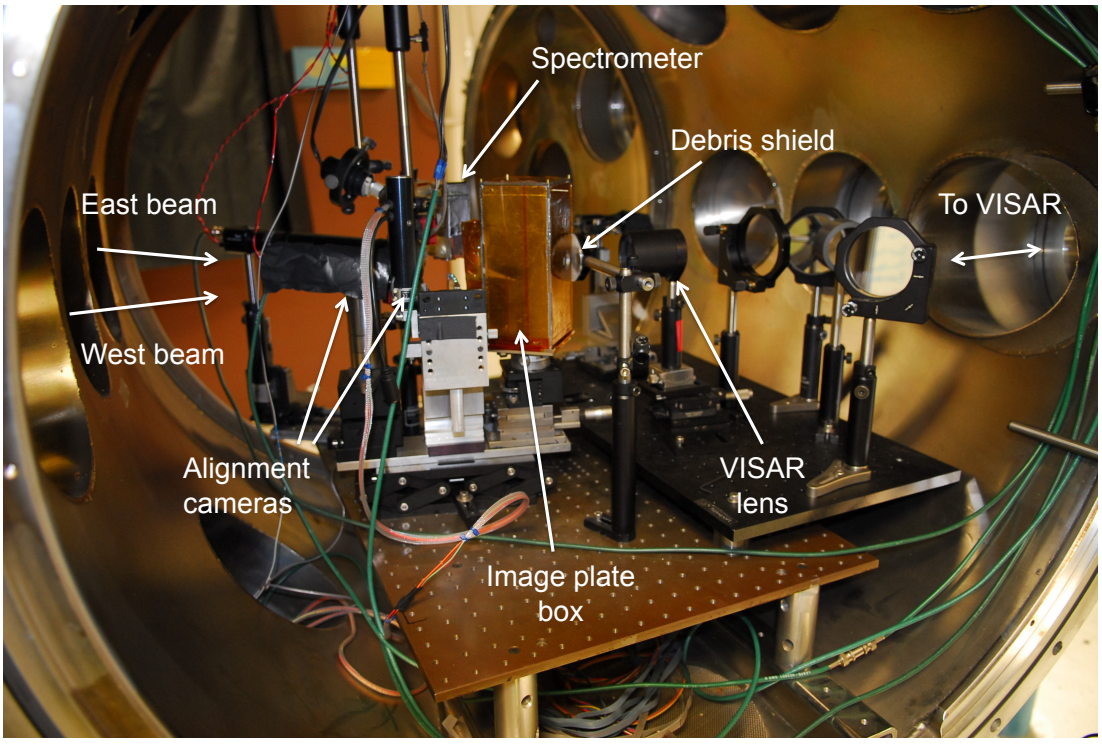


Figure 3.5: The Janus chamber as set up for white-light Laue experiments.

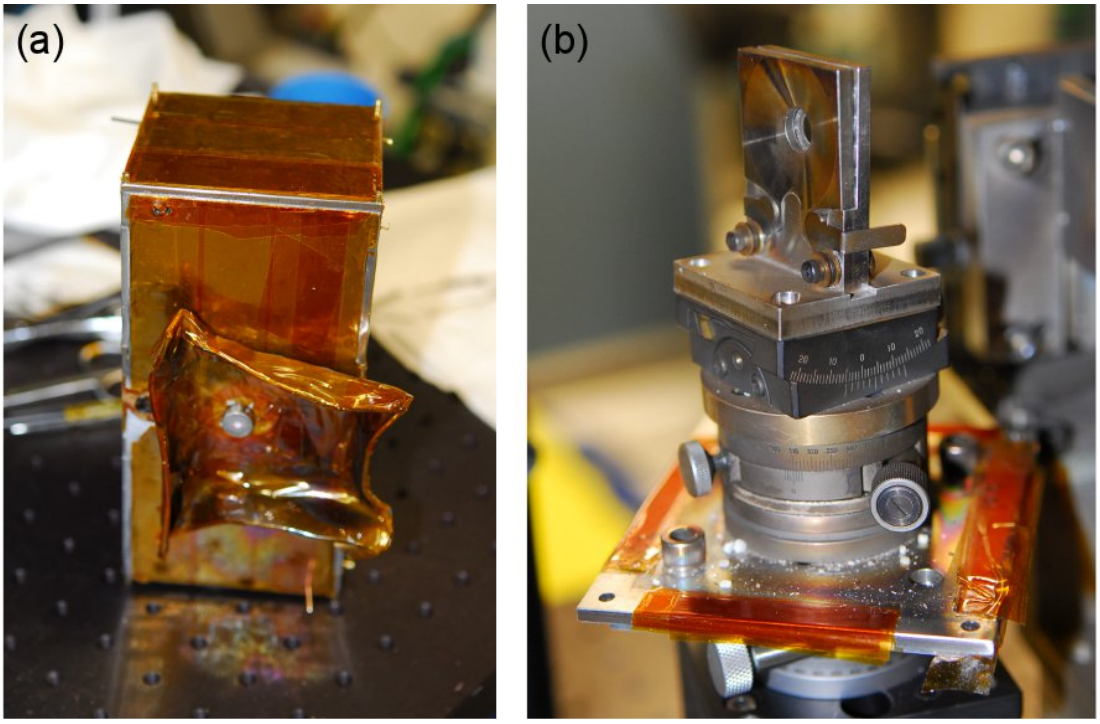


Figure 3.6: Image plate and target holder. (a) Shows the image plate box and shielding. Each side of the box holds image plates and filters. The outside is covered with a layer of lead and Kapton tape (giving it the orange colour). The backlighter foil is mounted at the end of the collimator and screwed in place with additional lead shielding. This box is then placed over the target mount which is shown in (b). The target crystal is sandwiched between two washers held by the mount which can be reproducibly removed and replaced on the goniometer using dowelled guides. The target is then normalised to the incoming VISAR beam using the goniometer stage.

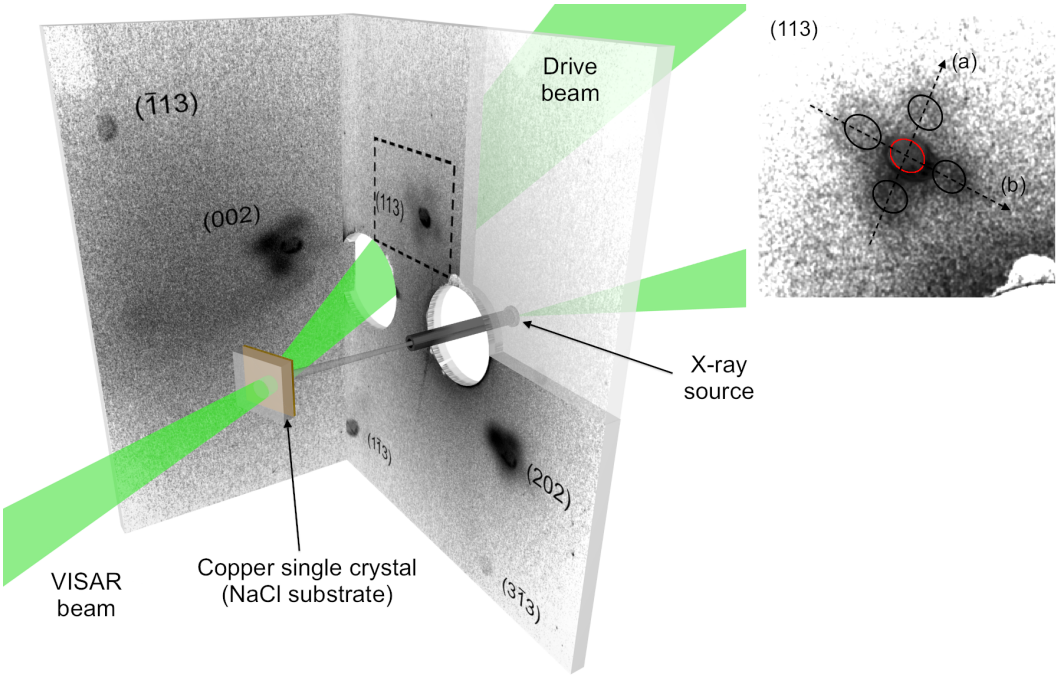


Figure 3.7: Schematic diagram of the nanosecond white-light Laue set-up. The target is mounted at the centre of an image plate lined box, with the necessary apertures for the drive, X-ray and VISAR beams. The diffraction pattern shown in the figure is data from copper shocked along [001] at approximately 30 GPa, with the corresponding lattice planes labelled (Two sides of the image plate box and the target and collimator supports have been removed for clarity). A close up of the (113) peak is inset. Figure is from [23].

into a collimating barrel that screwed into the image plate box, shown in figure 3.6(a). The barrel was 23 mm long with caps at each end to hold the backlighter and a gold aperture which could be varied in size. The available aperture sizes were 300 μm, 600 μm, and 1 mm, and the 1 mm was predominantly used in the experiment. The 1 mm aperture produces an approximately 2 mm diameter spot on target, which is larger than the 1 mm drive spot, this will be clear in the diffraction data discussed in chapter 4.

Since the collimator is fixed to the image plate box, the alignment of the collimator on target was not definitively checked on a shot-to-shot basis. The box

was positioned by shining a HeNe laser through a barrel with two gold apertures, aligning the beam to the center of the target mount. This process was repeated several times during the experiment to account for the gradual drift as the box was removed and replaced multiple times. The position of the backlighter foil, when aligned in this position, was imaged on a fixed camera which served as a reference from shot-to-shot and was used for focusing and aligning the backlighter beam.

The East alignment beam was focused on the outer area of the copper aperture holding the backlighter foil. This area was coated white to provide a better surface for focusing the beam than the backlighter foil itself which is too reflective. Between each shot the camera was refocused on this surface to account for small movements of the image plate box or collimator barrel. The 10Hz alignment beam was focused to produce the tightest possible spot, and then defocused by a variable amount to control the spot size.

The West (drive) beam spot was spatially smoothed using KPP phase plates, producing a 1×1 mm square spot on target. The 10 Hz alignment beam was focused and aligned onto the centre of the target mount and referenced by another camera using a removable mirror. The two beams were synchronized using the VISAR system. To do this, the beams were directed into the VISAR using a mirror at the target position and imaged on the streak camera, and the external triggers adjusted to synchronise the beams together.

3.4 VISAR

Velocity interferometry is crucial in most shock physics and other dynamic compression experiments. The measured velocity-vs-time profile can be used to deter-

mine the particle velocity which is an important variable in the Rankine-Hugoniot equations. Using equation of state (EOS) data it is possible to infer the pressure reached during the shock. If the shock velocity is measured along with the particle velocity the pressure can be directly inferred. Early techniques involved measuring the reflectivity of the rear surface, which generally decreases on shock breakout, to determine the shock velocity [68]. Other techniques measured the deflection of light from inclined mirrors [69]. The Velocity Interferometer System for Any Reflector (VISAR) was first developed in the 1960's and became the standard velocity diagnostic [11, 70, 71, 72, 73].

The VISAR system is based on interfering coherent light from the rear surface of the target with itself after a delay. A very simplified schematic of the VISAR used at Janus is shown in figure 3.8. Coherent light from the probe laser (in our case at $\lambda = 532\,\mathrm{nm}$) illuminates the rear surface of the target and the reflected light is collected and relayed to an interferometer. The light is split into equal parts and then recombined after passing one part through a delay leg. To allow the convenient change of delay, the delay leg contains a etalon of high index of refraction glass rather than simply a longer path. The recombined light generates an interference fringe pattern which is recorded with a streak camera. The streaked image has a horizontal axis corresponding to time and a vertical axis corresponding to length along the imaged line on the target surface. A change in the velocity of the surface produces a vertical shift of the fringes.

The interferometers used are in the Mach-Zehnder configuration as described in [74]. The incoming beam is focussed at the reflecting surface of the output beam splitter, the lower beam splitter in the interferometers shown in figure 3.8. The position of the etalon mirror is such that there is zero path delay with the

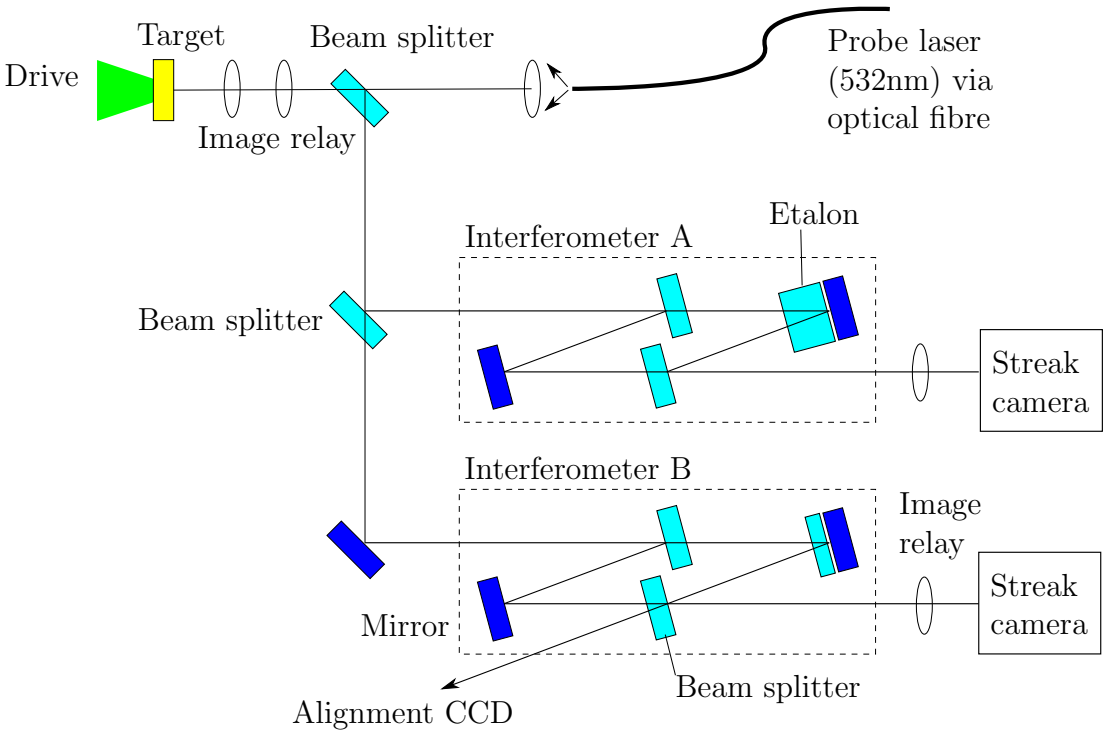


Figure 3.8: Simplified schematic of the twin bed VISAR system used at Janus. The etalons in each interferometer are chosen to provide a sensitive and unsensitive trace. The aim is that the velocity jump per fringe is much higher for the unsensitive bed, ensuring that the fringe jump is less than one, and several fringes for the sensitive bed, to provide greater resolution in the velocity profile.

Etalon (mm)	Delay τ (ns)	VPF (kms^{-1})	$\mathrm{VPF}_{\mathrm{NaCl}}$ (kms^{-1})
50.0	0.259	0.997	0.773
28.0	0.145	1.780	1.380
20.0	0.103	2.493	1.933
11.6	0.060	4.298	3.332

Table 3.2: VPF and delay values for the etalons used at Janus. Using two etalons of different length allows the discontinuous fringe shifts on shock breakout to be diagnosed unambiguously. The 50 mm and 20 mm were the typical configuration. The $\mathrm{VPF}_{\mathrm{NaCl}}$ are corrected for the change of refractive index in the shocked NaCl substrate.

etalon absent. The refractive delay introduced by the etalon is given by

$$\tau = \frac{2h}{c}\left(n - \frac{1}{n}\right) \tag{3.1}$$

where h is the etalon thickness, c is the speed of light, and n is the refractive index of the etalon. Typically the etalon is 10-50mm thick.

If the interferometer is perfectly aligned the output intensity is uniform as there is a single phase across the output beam splitter. The fringe pattern is produced by tilting the output beamsplitter which changes the path difference linearly across the output. The fringe spacing is adjusted by tilting the output beam splitter and the fringe contrast is controlled by slight tilting of one of the end mirrors.

Converting the fringe pattern to a velocity profile requires the velocity per fringe (VPF) [75]. The order of the interference in the combined beam is given by the difference in number of wavelengths in each leg

$$N = \frac{2h}{\lambda}\left(n - \frac{1}{n}\right) \tag{3.2}$$

and if the target surface moves with velocity $v(t)$, the wavelength λ_0 is Doppler

shifted, giving

$$\lambda(t) = \lambda_0 \left[1 - \frac{2v(t)}{c}\right] \tag{3.3}$$

The fringe count $F(t)$ is the difference between $N(t)$ and N_0

$$F(t) = N(t) - N_0 \tag{3.4}$$

$$F(t) = 2h\left(n - \frac{1}{n}\right)\left[\frac{1}{\lambda(t)} - \frac{1}{\lambda_0}\right] \tag{3.5}$$

Substituting equation 3.3 into 3.5, expanding, and neglecting higher order terms of $v(t)/c$ gives

$$F(t) = \frac{4hv(t)}{\lambda_0 c}\left(n - \frac{1}{n}\right) \tag{3.6}$$

$$F(t) = \frac{2\tau v(t)}{\lambda_0} \tag{3.7}$$

The VPF is therefore given by

$$\text{VPF} = \frac{v(t)}{F(t)} = \frac{\lambda_0}{2\tau} \tag{3.8}$$

An additional correction for the change in refractive index of the etalon due to the change in wavelength is

$$\text{VPF} = \frac{\lambda_0}{2\tau(1+\delta)} \tag{3.9}$$

shown in [75] where δ is given by

$$\delta = -\frac{n_0}{n_0^2 - 1}\lambda_0 \frac{dn}{d\lambda}\bigg|_{\lambda=\lambda_0} \tag{3.10}$$

For the fused silica etalons used in the experiment $\delta = 0.0318$ at 532 nm [74].

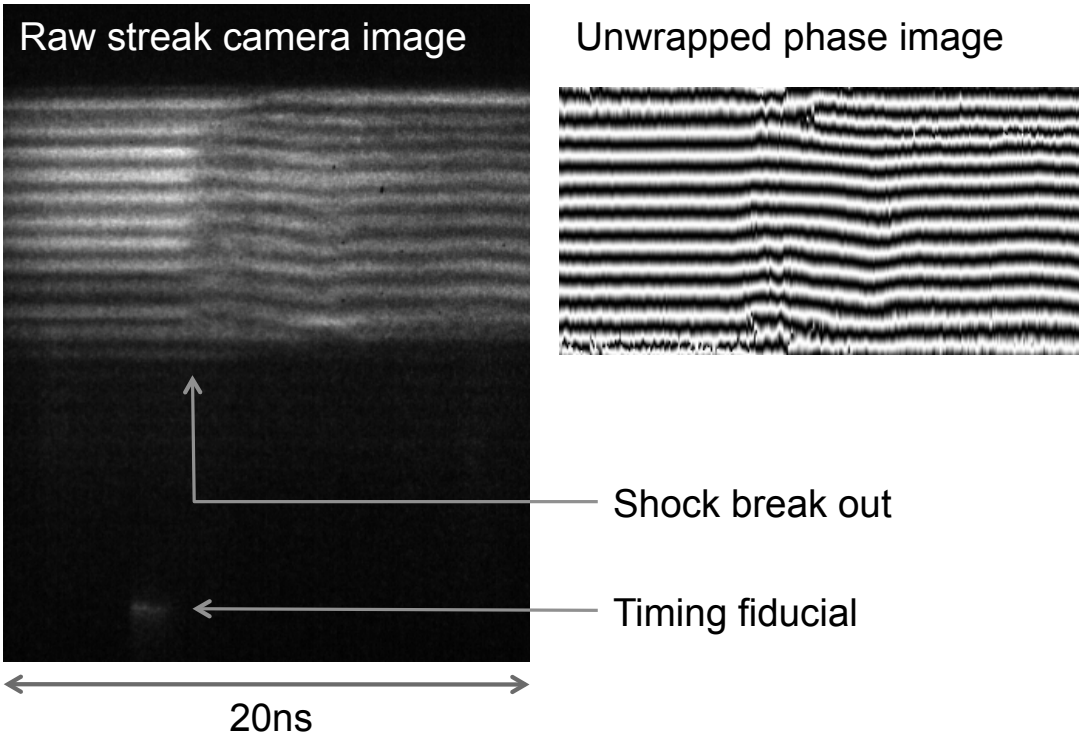


Figure 3.9: VISAR raw data. The left image shows the raw streak camera image for a shot on Cu [001]. The vertical axis is distance along a line on the rear surface of the shocked sample, the horizontal axis is time (ns). The shock break out time is indicated, where the fringe intensity decreases, and there is a discontinuity. The edges of the shocked region are visible at the top and bottom of the fringe pattern, where there is no discontinuity. The 'unwrapped' phase image to the right is produced after Fourier transforming at each time, filtering the background function, and inverse Fourier transforming. The phase-time profile for a selected region can then be calculated and converted into a velocity-time profile using the VPF.

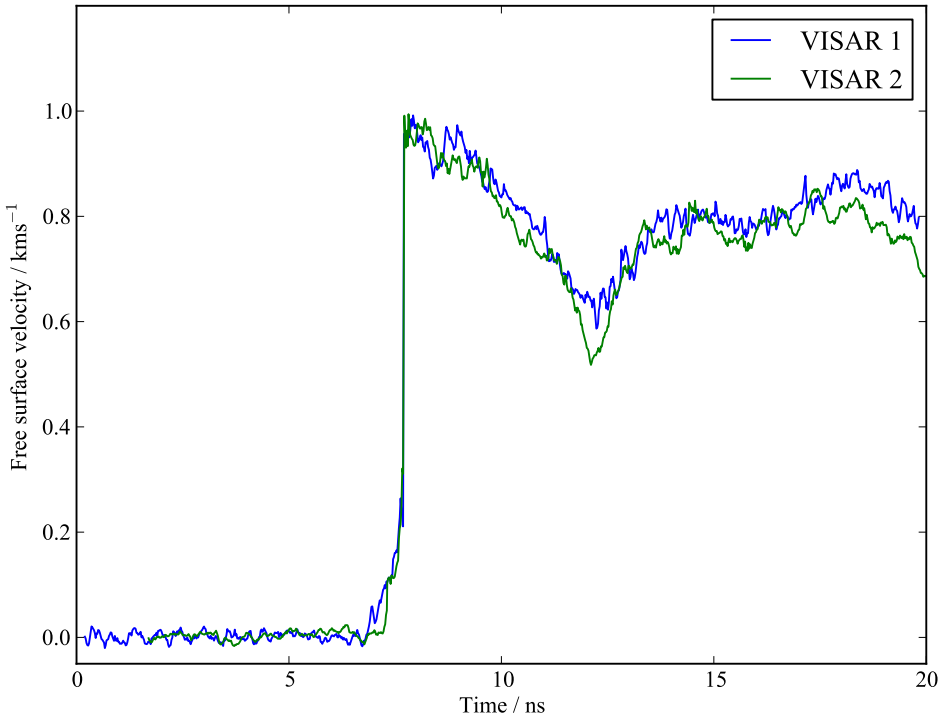


Figure 3.10: Copper-NaCl interface particle velocity-time profile for shock in [001] direction of single crystal copper. The two traces are from the individual VISAR beds for the same shot.

A typical raw streak camera image is shown in figure 3.9. The fringe phase as a function of time was extracted using the XVIS code produced by Damien Hicks at LLNL, which employs a Fourier transform method described in [74, 76]. The output is an 'unwrapped' phase image as shown in figure 3.9 and plot of phase against time. The profile is corrected for background drift of the fringes using a pre-shot image of the pattern from the static sample. The fringe shift ambiguities at shock break out are removed by comparing the traces from the two VISAR beds and adding integer fringe shifts until the profiles overlay as shown in figure 3.10. The VPF can then be applied to produce a velocity-time profile.

As described in section 3.3.2, the majority of the copper targets were not removed from the NaCl substrate. For these targets the VISAR is focused on the rear surface of the copper and the measured profile is the velocity of that interface. An additional correction factor must be applied to the VPF as the NaCl index of refraction changes with compression.

$$\mathrm{VPF}_{\mathrm{actual}} = \mathrm{VPF}_{\mathrm{measured}} \left(1 + \frac{\Delta v}{v_0}\right)^{-1} \tag{3.11}$$

where $\Delta v/v_0$ is the fractional velocity change for the shocked unshocked window. The measured $\Delta v/v_0$ value for NaCl is constant at 0.29 [77, 78].

For the copper targets with NaCl substrate, the velocity measured is not the particle velocity but rather the particle velocity at the interface between the copper and NaCl. This means that the data must be interpreted in the same way as a so-called impedance-matching experiment [34]. The shock impedance, Z is defined as:

$$Z = U_s \rho_0 \tag{3.12}$$

Where U_s is the shock velocity and ρ_0 is the initial density. In our case the

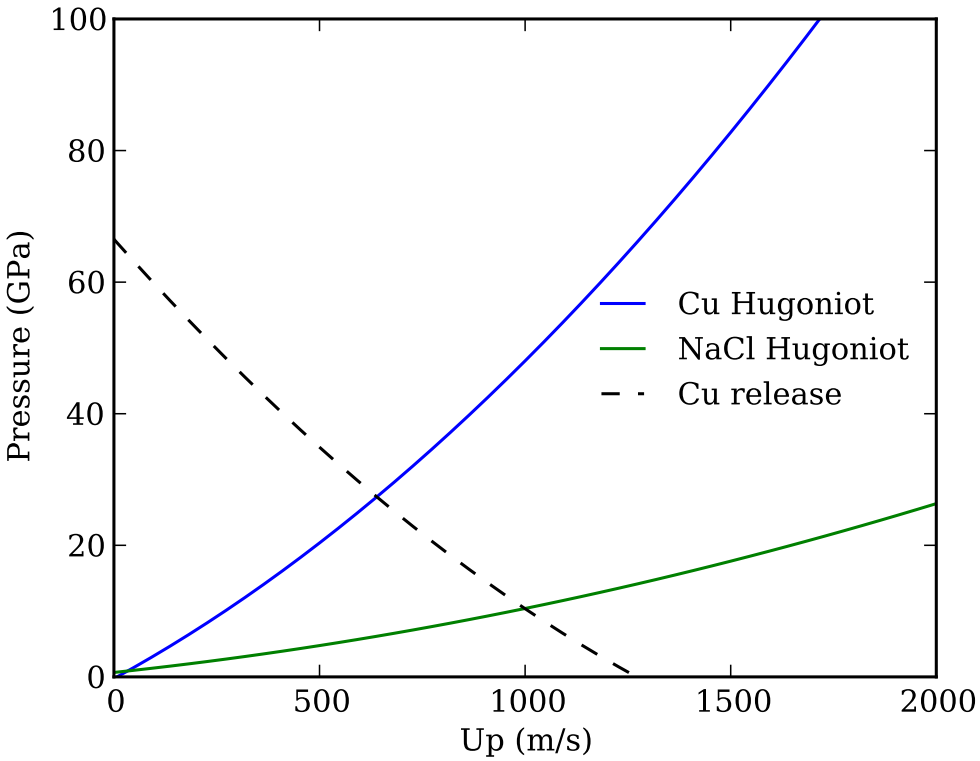


Figure 3.11: Hugoniot plots for copper and NaCl. The release curve for the copper is shown by the dashed line and is approximated by taking the mirror image of the copper Hugoniot. In this case the measured interface particle velocity from VISAR is $1000\,\mathrm{ms}^{-1}$. The copper release curve is plotted intersecting the NaCl Hugoniot at this velocity. The original pressure in the copper is given by the intersection of the release curve and the copper Hugoniot.

shock propagates from a material of higher impedance to a material of lower impedance, and the wave reflected back into the copper is a release wave rather than a reshock. For lower pressure shocks (less than 100 GPa) it is common to approximate the release adiabat by taking a mirror image of the Hugoniot in the pressure-particle velocity plane [79, 80, 81], as shown in figure 3.11. In this way, the pressure in the copper is calculated from the measured particle velocity. Of course, this relies on EOS data, where the shock velocity as well as the particle velocity are measured.

3.5 Fitting code

A fitting code was written for diffraction pattern analysis and future experimental planning. The code is written in straightforward Python with the user interface implemented using the TraitsUI package and Chaco plotting package. The advantage of Python is that the code is easily portable and will run on any system where Python is installed. This is most easily achieved by installing Enthought Python Distribution (EPD) which is a free, cross-platform, Python distribution, and the code has been tested on both Windows, Mac OS X, and the Linux operating systems for personal computers. The EPD provides the Traits and Chaco packages built-in.

The program's main window, shown in figure 3.12, displays a tabbed list of crystals and controls for setting the crystal parameters. An arbitrary number of crystals (within reason) can be added or removed, which is useful for fitting the overlapping patterns of a crystal and it's growth substrate for instance, such as tantalum and MgO, or for comparing changes to the calculated diffraction pattern due to perturbations, such as small angle rotations.

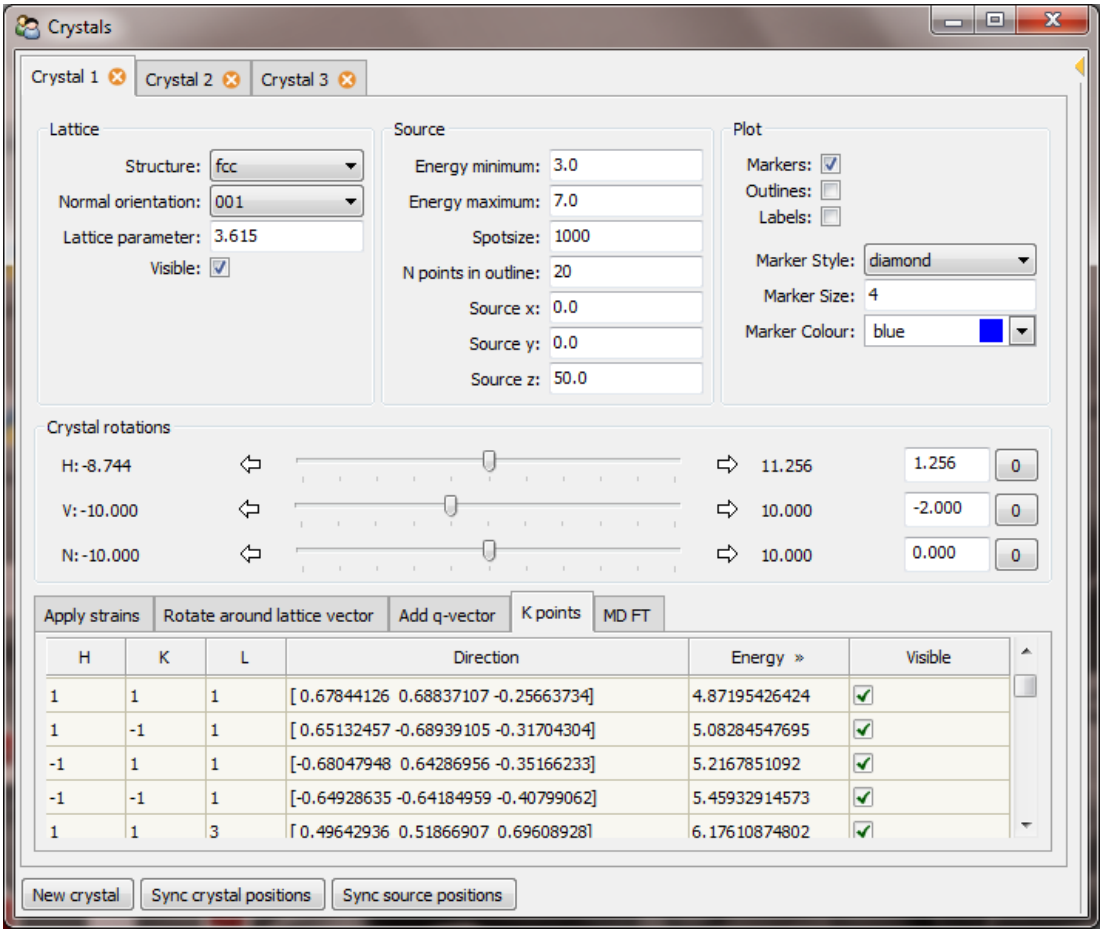


Figure 3.12: Fitting code interface for crystal parameters. The code can fit an arbitrary number of crystals with parameters set via the controls in this window. The properties of the lattice such as lattice parameter, structure, etc are set in the main window, along with controls for fitting the crystal orientation. Permutations to the crystal such as strain, rotation about lattice vectors, adding q-vectors, are controlled with the tabbed pane at the bottom of the window. The calculated orientation and x-ray energy for each k-point is tabulated. The checkbox indicates if the energy is within the given energy range, and allows the markers for individual peaks to be toggled on or off, useful for example where two peaks are overlapping and the labels are overwriting each other. The orientations of the crystals and the x-ray source positions can be synced across all the crystals which is useful for comparing permutations.

Each crystal has a number of parameters defining the lattice and orientation. Currently the supported crystal structures are simple cubic, face-centred cubic, body-centred cubic, and cubic diamond. The 'normal orientation' indicates the lattice direction which is parallel with the crystal surface normal, with [001], [110], and [111] options, which are typical for these experiments. The x-ray source position for each crystal can also be varied which can be used for comparing different source positions in the planning stage of an experiment. The crystal orientations and x-ray source positions can be synced, to enable the comparison of different perturbations in the same experimental geometry.

The tabbed pane at the bottom of the window holds the controls for perturbing the lattice. A full strain tensor can be applied to the crystal. The crystal lattice can be rotated around a given lattice direction. Small '**q**-vectors' can be added to the reciprocal lattice points to simulate streaking of the diffraction peaks due to stacking faults, for example. The modular nature of the code means that adding further perturbations is relatively straightforward. The final tab provides a table of reciprocal lattice points with the calculated direction in real space and x-ray energies. This is useful for seeing which reflections are present. The table also allows individual peaks to be toggled on or off, for clarifying the plotted diffraction pattern.

The diffraction patterns produced by the crystals can be plotted on multiple image plate windows, one of which is shown in figure 3.13. Image plate window consists of two panes, the diffraction plot itself, and a control pane. The position of the image plate is defined by two angles and a distance parameter. This defines the origin of the plane and in general the rough normal orientation. Two further controls tilt the plane about its x and y axes to set the orientation of the plane. Clearly, it is possible to set the plate position using just the two angles, and

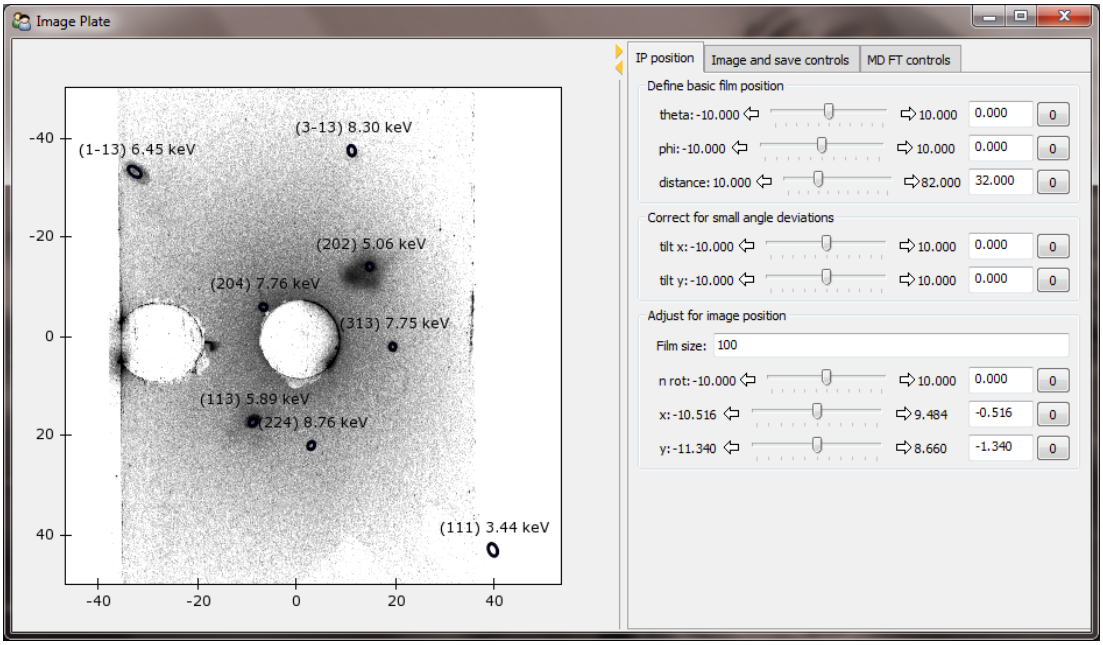


Figure 3.13: Fitting code interface for image plate. The code can handle multiple image plates which are generated in individual windows along with the necessary controls shown here. Typically no more than two or three image plates are required for fitting the data, however, being able to compare multiple image plate positions is useful for planning and comparing experimental geometries. The first three controls set the image plate 'origin' and orientation which can then be corrected for small angle deviations by the next set of controls. The rotation of the image and x and y offsets are adjusted for the plot rather than actually rotating the image. Additionally there are various controls for the adjusting the output figure.

distance controls, along with offsets in the plane, but having these additional tilt controls makes things more user friendly. The other controls rotate and offset the image, however, rather than actually rotate and offset the image, the diffraction pattern is rotated and offset with the image remaining fixed. Plate positions can be loaded and saved once defined for a given experimental set up.

All the parameters for crystals and image plates can be saved or loaded for a given shot number. This functionality uses the Python pickle module to dump and load the crystal and image plate objects. Additionally the parameters are saved in a plain text file. The image plot has zoom and panning tools, for looking at diffraction peaks in more detail during fitting.

3.5.1 Algorithm

The basic algorithm for calculating the diffraction pattern is relatively trivial and there are several codes available for predicting Laue patterns. In general these codes are designed simply for indexing a pattern and allowing the sample to be orientated along a specified direction. There are several important additions required for our specific needs. Perhaps the most important is that the x-ray source is slightly divergent unlike a much more collimated source such as a standard x-ray tube or the beam at a synchrotron[1]. This does not effect the position of centre of the diffracted spots but is important when finite spot sizes are to be simulated. Since the spot sizes used are relatively large in the experimental set-up used at JANUS, as well as the set-up used at Omega, the ability to fit not only the spot centres but also the spot shape is important. In fact, fitting the spot outlines provides a much greater constraint on the fitting parameters resulting in a much more accurate fit.

[1]The option to use a purely collimated beam is available in the code but not set by default.

For each crystal, the first calculation is the allowed values of (h, k, l) for the given crystal structure, using the classical selection rules described in section 2.2.4. The initial lattice vectors are set according to the 'normal orientation' value. After applying the strain matrix, the $\mathbf{G}_{h,k,l}$ for each (h, k, l) is calculated. At this point, any additional $\mathbf{q}$-vectors or rotations about specified lattice vectors are applied.

For the spot centres, the direction of the incoming ray $\mathbf{k}$ is defined by the specified x-ray source position, as the crystal is defined as the origin. The plane separation d is calculated using

$$d = 2\pi/|\mathbf{G}_{h,k,l}| \tag{3.13}$$

The x-ray energy is then calculated simply using Bragg's law. The diffracted ray vector is given by the Laue equation

$$\mathbf{k}' = \mathbf{G}_{h,k,l} + \mathbf{k} \tag{3.14}$$

The diffracted ray vectors are then passed to the image plates and the intersection points calculated.

For finite spot sizes, the incident and diffracted rays will have a different energy for each point in the spot. In the code, the cone of rays which outline the spot are defined by the x-ray source position and the input spot size, which represents the spot size which is produced if the crystal surface is normal to the cone axis. The user specifies the number of rays used for the spot outline and the intersection with the crystal surface is calculated. The diffracted ray for each point in the outline is calculated as outlined above for the central peak, and mapped to the image plates. Although the plotted peak positions update smoothly, using a large

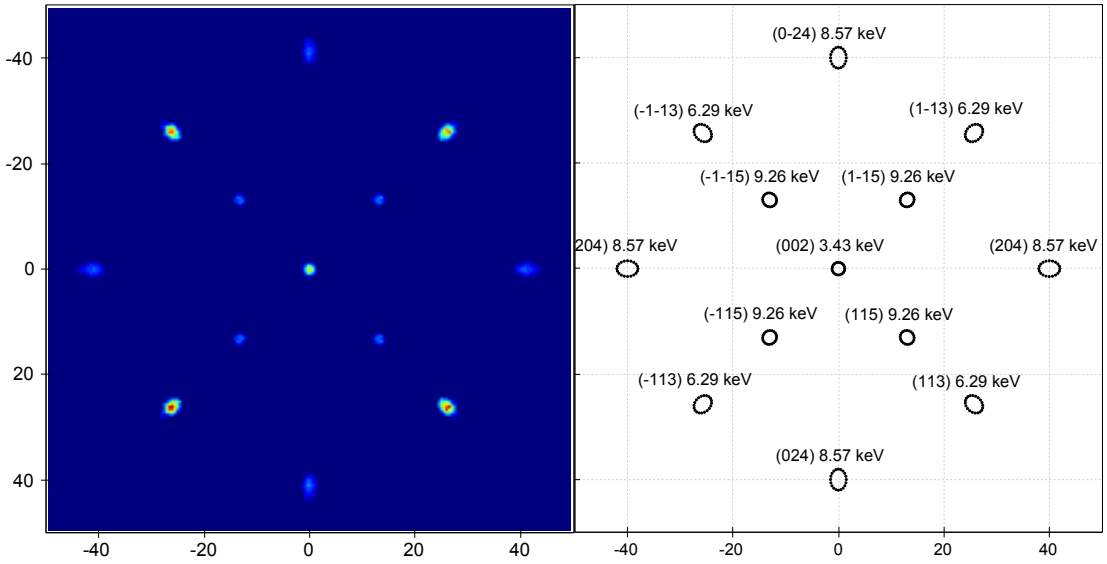


Figure 3.14: Example of simulated diffraction plot. The left image shows the simulated pattern from a MD simulation of copper at 300 K. In this case the image plate is positioned to be in direct back-reflection, with the crystal normal parallel to the image plate normal. The code will ray trace for any combination of crystal and image plate position. The right image indicates the spot indexes and x-ray energies.

number of points in the spot outline (> 20) results in a noticeable reduction in performance.

3.5.2 Simulated diffraction from MD

The fitting code is designed with experimental planning and data analysis in mind. However, it is also suitable for plotting simulated diffraction patterns from MD simulations. The code implements a ray tracing technique as described in detail in [52] and [82]. The main difference between this method and the tracing technique described in section 3.5.1 is that the rays are traced from the image plate, to the crystal, and then to the source. This vastly reduces the number of calculations by excluding rays which interact with the crystal but do not reach the film. The code can plot the simulated diffraction for a finite spot size as well

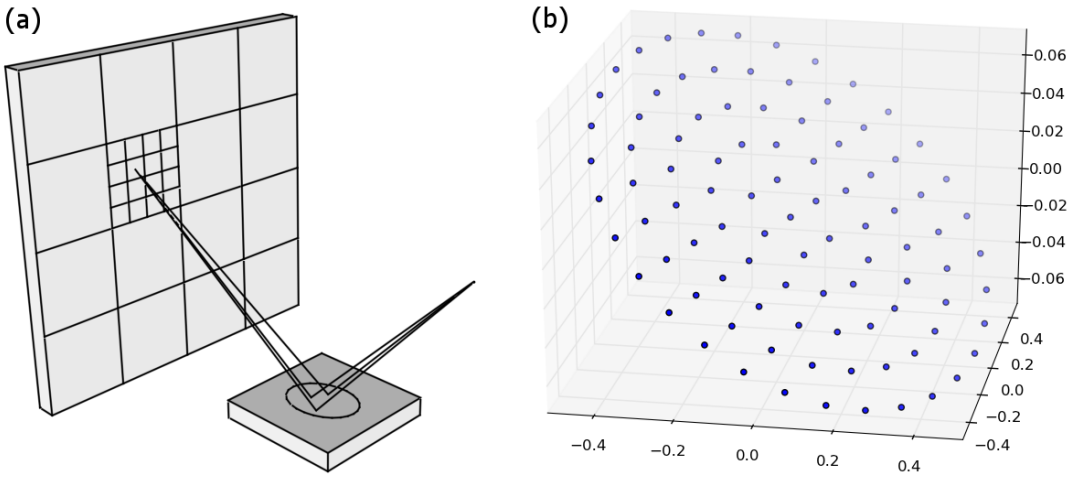


Figure 3.15: Ray tracing principle. (a) The film is divided into pixels and sub-pixels, in the figure only four oversized pixels are shown, with four sub-pixels per pixel. Rays are traced from each sub-pixel to sample points in the spot on the crystal surface. The vectors from the source to the crystal and from the crystal to the sub-pixel define a set of **g**-vectors in a given energy range. Figure (b) shows an example of how the crystal spot is sampled. Sample positions are calculated for a user-defined density, and the dependence on distance to the source is neglected.

as a single incoming ray.

For a single incoming ray the basic process is as follows. The MD simulation is sampled and the discrete Fourier transform calculated for a chosen range of reciprocal space, and this file is passed to the fitting code. The user defines an energy range and resolution over which to sample the Fourier transform. The film is divided into pixels and the pixels are further divided into sub-pixels if desired by the user. For each sub-pixel, at each energy, the distinct **G**-vector is calculated. The corresponding intensity is gathered from the Fourier transform and summed for each sub-pixel over all energies in the range. The sub-pixels are then summed for each pixel.

For a finite spot size there is the added complication of needing to scan over multiple positions on the crystal surface. The spot is divided into an evenly-spaced grid and each sub-pixel sums the intensity for all energies for each point

on the grid. The intensities are scaled by $1/r^2$. However, the effect of the oblique angles at which the rays intersect the crystal and the image plate is neglected. Sampling a finite spot size reduces the ray trace speed vastly.

Chapter 4

In situ x-ray diffraction from silicon and copper

The following chapter describes the results for experiments at JANUS utilising the white-light Laue technique.

4.1 X-ray source

The x-ray source was a key component of the experiment. For each shot the x-ray spectrum was recorded using the flat-crystal spectrometer described in section 3.3.1. Figure 4.1 shows the raw data for the 100mm strip of image plate used in the spectrometer. In an ideal case the x-ray yield should be fully optimized, however, with a limited number of experimental shots it is a case of balancing the time spent optimizing the set-up and time taking full data shots. This section presents the calibration method, calibrated spectrum, and source optimisation.

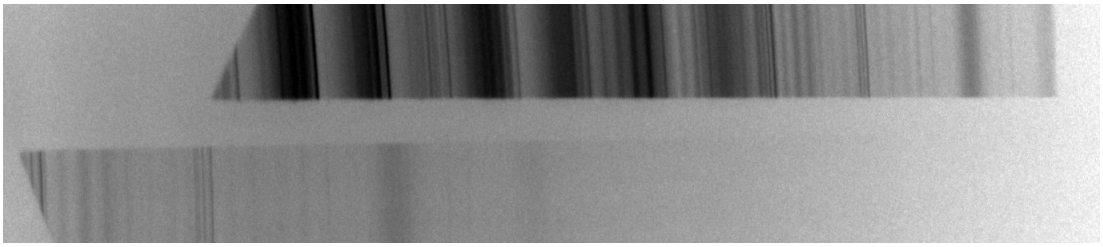


Figure 4.1: Crystal spectrometer raw data. The upper part of the image plate records the spectra from the (111) silicon wafer, and the lower part records diffraction from the (220) planes of the (110) silicon wafer.

4.1.1 Spectrum calibration

The spectra were calibrated using two methods. An initial calibration was made using the known geometry of the spectrometer. At the higher energies, above 6keV, the spectra from the (111) crystal and the (110) crystal overlap. The position of the source is varied until spectral features in the overlapping region match, this gives a rough calibration. During the experiment the spectrometer was fixed in place much of the time, however, whilst adjustments were made to the set-up, the position of the spectrometer did change and this rough calibration was required for each new position.

Once the rough calibration is made, the prominent spectral lines can be matched to reference lines from the NIST atomic spectra database [83] and in the literature [64, 84, 85, 86]. The pixel position and spectral line energy are then plotted, producing an instrument calibration curve as shown in figure 4.2. The peaks in the 3.0-3.5 keV range are M-shell emission from Palladium matching the emission observed by Phillion *et al* [64]. The most prominent spectral lines are the Ti and V He-α emission ($1s^2$-1s2p) at 4731 and 5718 eV respectively. Figure 4.3 shows a typical calibrated spectrum.

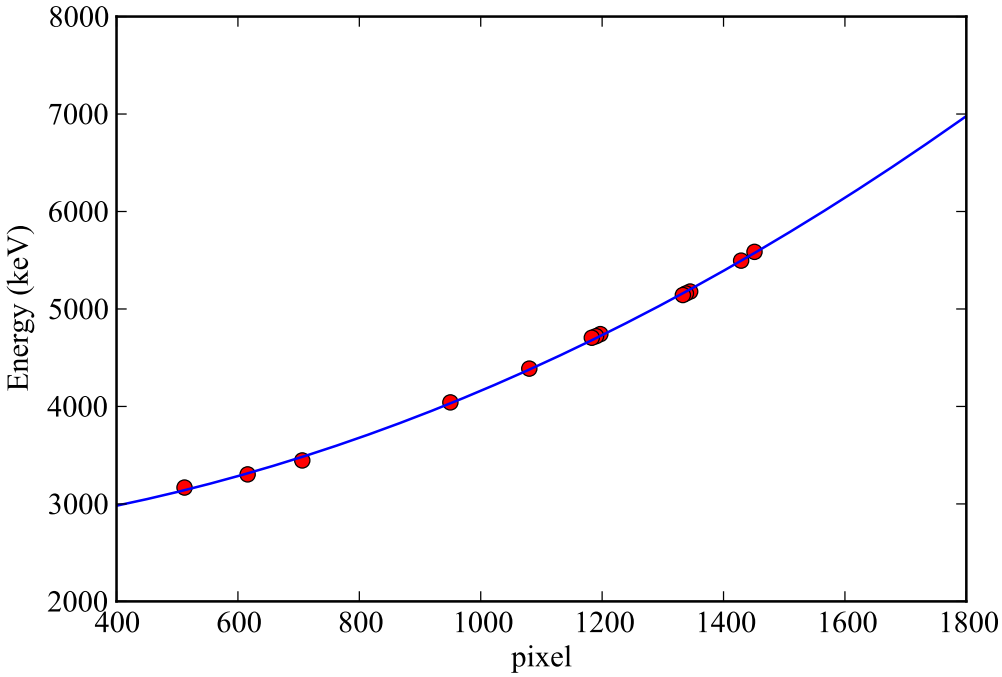


Figure 4.2: Calibration curve for (111) silicon crystal spectrometer. Plot of pixel position against energy of distinctive spectral features in the spectrum. The (220) crystal recorded at a higher energy range with fewer points to build a calibration curve, hence the calibration for the (220) crystal was based purely on the known geometry of the spectrometer rather than spectral features. The spectra shown later in this chapter are from the (111) crystal.

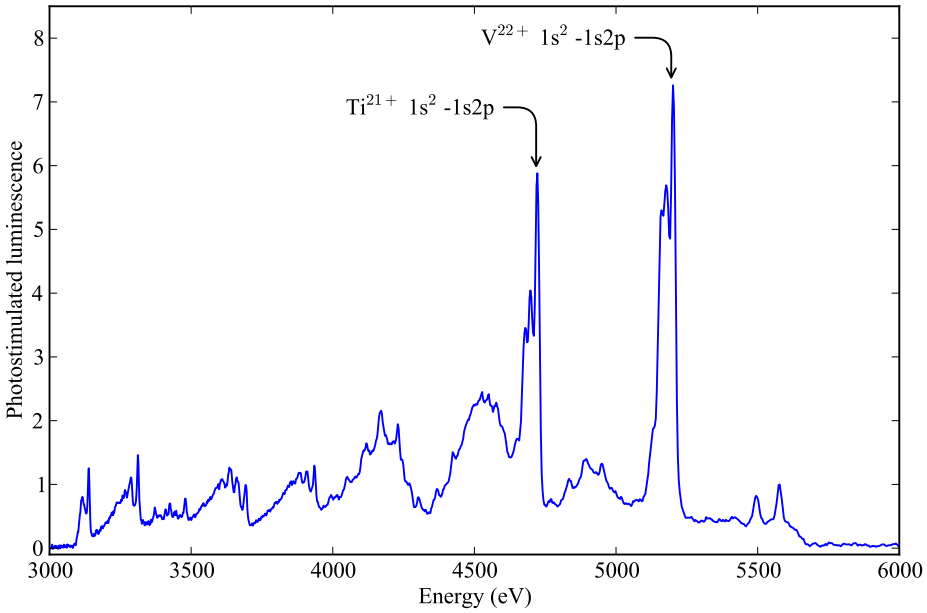


Figure 4.3: Typical backlighter x-ray spectrum after energy calibration and background subtraction. This is the spectrum recorded by the (111) Si crystal, the (220) crystal records higher energies up to 8 keV. The two brightest spectral features are the He-α emission from the titanium and vanadium, as labelled.

4.1.2 Source optimisation

There has been a large amount of study of laser to x-ray conversion efficiencies especially as K-α and He-α sources for radiography and monochromatic diffraction experiments [87, 88, 89]. For our purposes we aimed to use the broadband emission from L and M-shells where there have been fewer studies. This is perhaps because it may be more difficult to define the conversion efficiencies of these emitters in comparison to K-α sources as the x-rays cover a broader energy range.

To maximize the x-ray yield the maximum energy possible on the east beam was requested, which was typically around 250J. By defocusing the spot from best focus the intensity on target was varied in the range from $6.5 \times 10^{13}\,\mathrm{Wcm^{-2}}$ to a maximum of $9.0 \times 10^{14}\,\mathrm{Wcm^{-2}}$. Figure 4.4 shows spectra for several different laser irradiances. The energy measured in the pulse for the five spectra shown were in the between 243 and 261 J so the differences between the spectra are due to the change is spot size rather than a large change in the total incident energy which is nominally constant.

The brightest spectra were recorded at an irradiance of $2.2 \times 10^{14}\,\mathrm{Wcm^{-2}}$, with increased x-ray intensities over the 3-6 keV range. Figure 4.5 shows a plot of x-ray yield against laser irradiance. However, there is significant variability from shot-to-shot as shown in figure 4.5 where a simplistic x-ray yield is plotted against laser irradiance. The yield given is the mean PSL calculated for the x-ray energy between 3 and 6 keV. The vast majority of the points are at irradiances close to $2.2 \times 10^{14}\,\mathrm{Wcm^{-2}}$, where the defocus distance was nominally constant with small changes in the measured pulse energy.

There are several potential causes for the unreliability of the source. The energy in the laser pulse is largely reproducible to within 10%, however, the error in the spot diameter is much greater. The size of the spot is determined by the

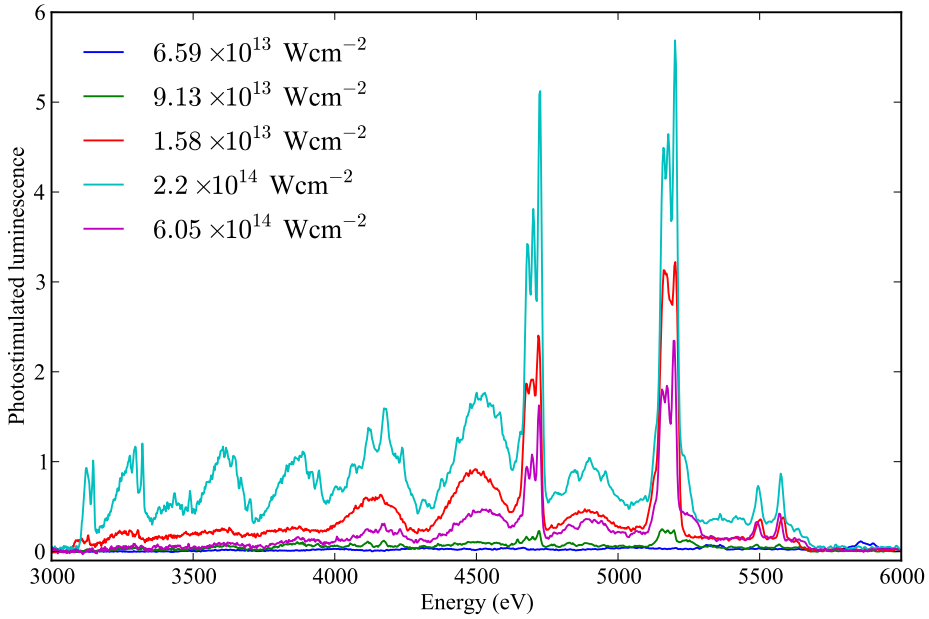


Figure 4.4: X-ray spectra for a range of laser irradiances. The legend indicates the incident laser intensity for the 2 ns pulse. A limited number of shots were taken for source optimisation and a defocusing length giving an intensity of $2.2 \times 10^{14}\,\mathrm{Wcm^{-2}}$ was chosen for the rest of the experiment.

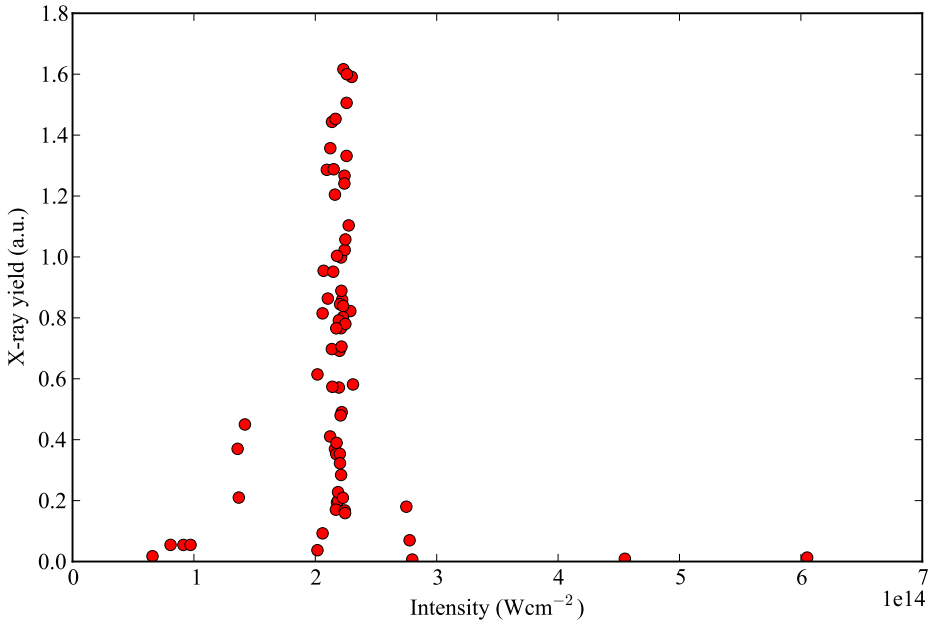


Figure 4.5: Plot of x-ray yield against laser irradiance for x-rays in the 3-6 keV energy range. The large number of data points at approximately 2.2×10^{14} are at the intensity chosen after an initial intensity scan. The yield calculated as the average PSL over this energy range. This data is from the experiment in 2010.

defocus distance from best focus which is difficult to quantify and the judgement of the person focusing the beam. Although the position of the focusing lens is known, in our set-up at Janus, the position of the backlighter foil can change by of order 0.5 mm and the position of the focusing lens therefore varies for each shot. Finding the position for the best focal spot is difficult and this add significant uncertainty to the measured incident laser irradiance.

Another potential cause for the large shot-to-shot variation is the backlighter foil itself. The layered nature of the foil makes it extremely delicate and prone to de-lamination from the plastic substrate. The surface of the foil also appeared tarnished in some areas. The surface of the foil was inspected under a microscope and poor targets rejected, however, changes in the backlighter foil quality may also have introduced significant variability in the brightness of the x-ray source.

4.1.3 Comparison with an implosion x-ray source

In order to make a direct comparison with other x-ray sources such as implosion capsule, the absolute intensity produced by the mixed-metal foil must be calculated. The first thing is to remove the background due to fluorescence. When the crystal spectrometer is correctly aligned, there is a strip of the image plate between the spectra recorded by the two silicon crystals (shown in figure 4.1) which provides a measure of the background fluorescence. This provides a method of neatly removing the background as demonstrated in figure 4.6 which shows a plot of the spectra, background, and resulting spectra after background removal.

After calibrating pixel to x-ray energy, as described earlier, the image plate sensitivity as measured by Maddox *et al* was used to calculate the number of photons and hence the energy at each pixel [66]. A correction was made for the absorption of the Kapton filters which covered the spectrometer entrance and

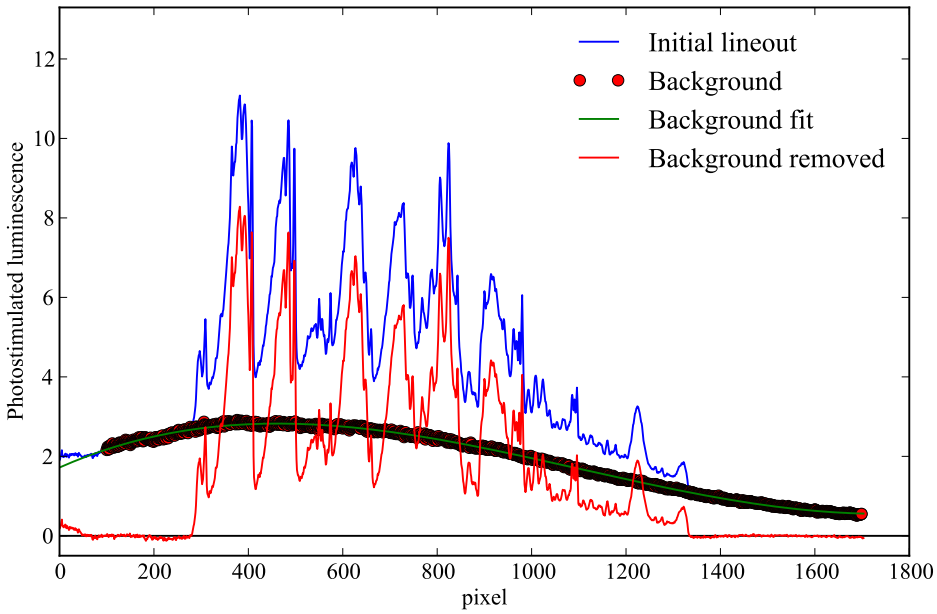


Figure 4.6: Fluorescence background subtraction.

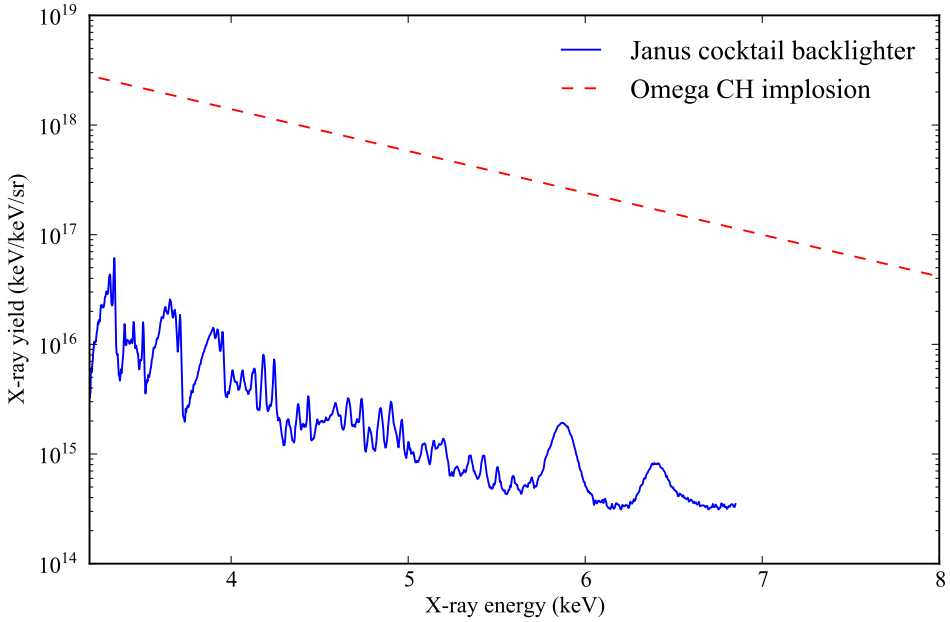


Figure 4.7: Plot of x-ray fluence against energy. Also shown is indication of the fluence produced by a CH implosion capsule at Omega [90].

image plate. Using the known geometry of the spectrometer the total distance from source to image plate can be calculated. The values for crystal reflectivity from Henke *et al* were used [91]. Figure 4.7 shows a plot of fluence against x-ray energy. The implosion source is several orders of magnitude brighter which is expected.

4.2 Shocked silicon

Single-crystal silicon was chosen as the target material in order to test the capabilities of the instrument. Not only are such crystals cheap and readily available, but previous work has shown that on nanosecond time-scales silicon can sustain large elastic compressions under shock conditions [63]. Elastic compression will result in a shift of the Laue spots owing to the change in shape of the unit cell. The hope was that the large elastic compression would result in a more measurable shift of the Laue spots.

The shock compression of single crystal silicon has been studied for many years [15, 92, 93, 94]. Even for, what might be called, the simplest case of a shock along the [001] axis there is some debate over the compression in the elastic regime. The large elastic compressions observed be Loveridge-Smith *et al* [63] for a laser-driven shock were not observed in later gas gun work [94].

Figure 4.8 shows a raw image of the single-shot diffraction pattern from an unshocked 50 μm thick crystal of Si, with the (001) reciprocal lattice vector parallel with the crystal surface normal. There are 24 visible diffraction spots with energies from 3.9 keV $(1\bar{1}3)$ to 9.52 keV $(2\bar{4}6)$. It should be noted that although the diffraction pattern is from unshocked silicon, the silicon has been driven, but timed such that the shock drive was after the x-ray pulse, in order to generate

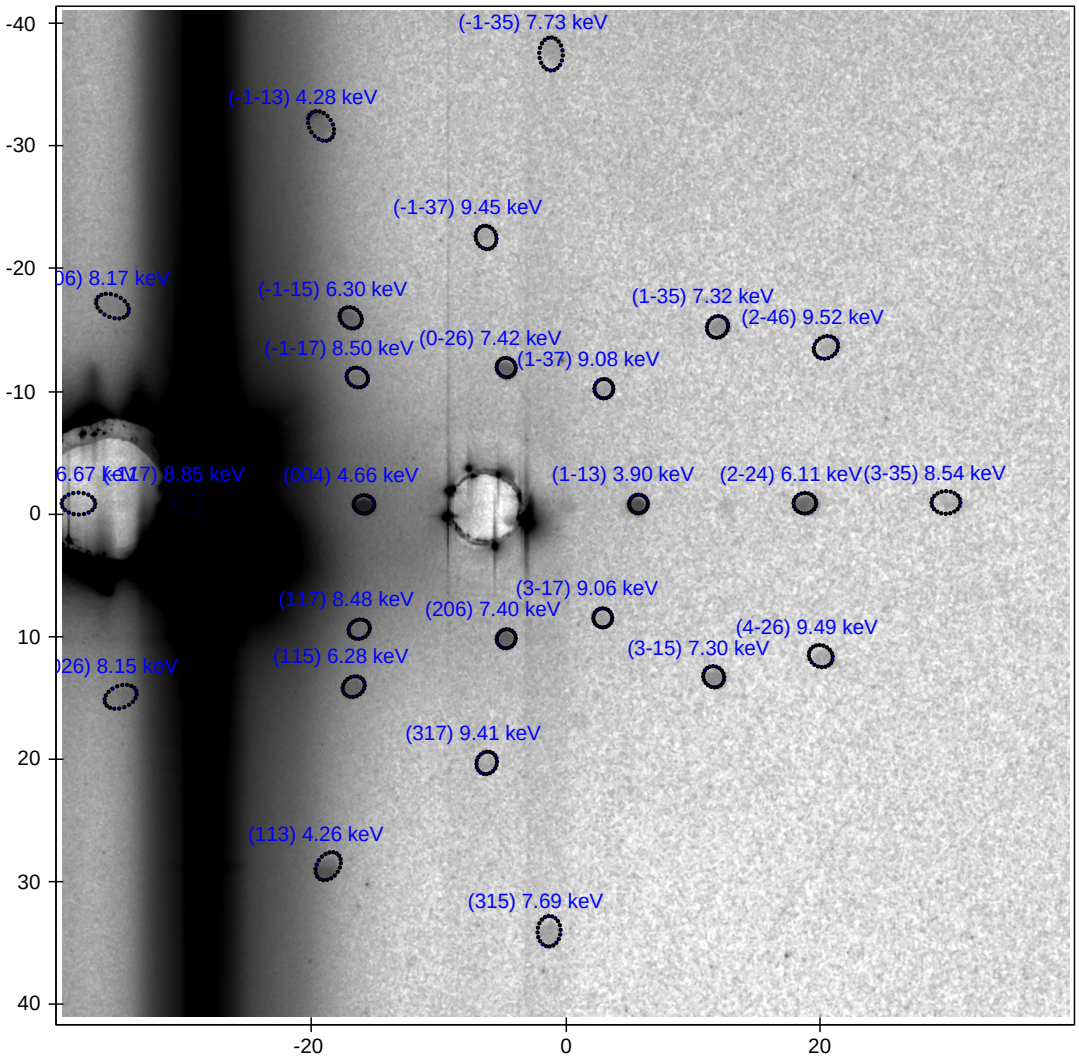


Figure 4.8: Diffraction pattern from unshocked, 50μm thick silicon, with surface normal parallel to the crystal [001]-direction. The dark strip is due to saturation of the image plate at the edges of the drive beam hole.

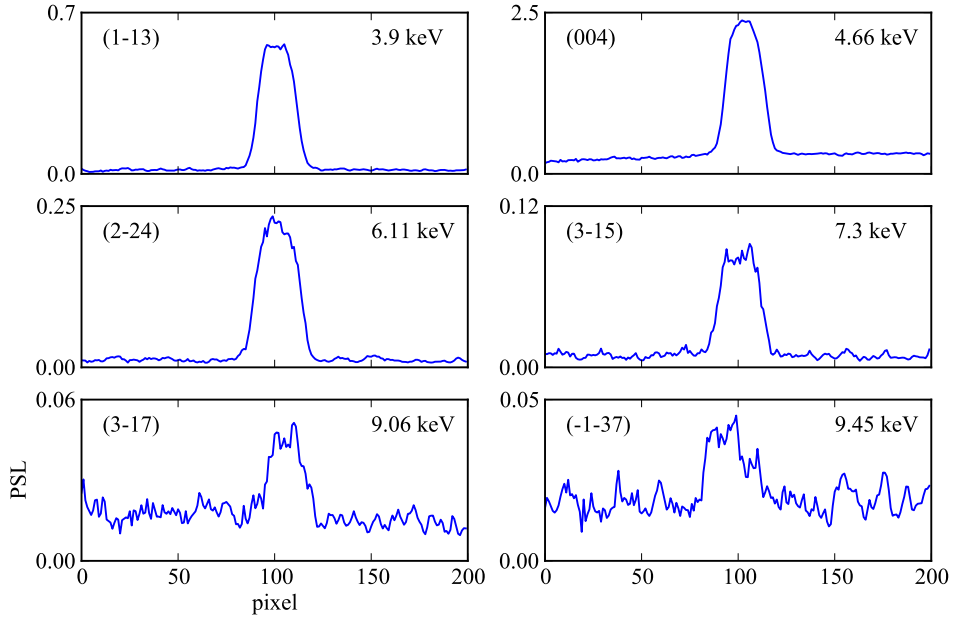


Figure 4.9: Lineouts through several diffraction peaks from the shot shown in figure 4.8. The spot index and energy are indicated. For the majority of peaks, the signal is approximately an order of magnitude greater than the background. For the higher energy peaks ($> 8\,\mathrm{keV}$), the bottom two plots in the figure, the signal-to-background ratio is approximately two.

equivalent background from the drive. The highest energy spots are at a higher energy than recorded by the crystal spectrometer and show that even at these energies there is significant emission from the mixed-metal foil. The smooth nature of the diffraction spots also implies that there is significant continuum emission filling in the gaps between line emission in the spectrum. On shots where the x-ray yield was low, it was possible to observe spectral features in the diffraction spots. The signal-to-background for several spots are shown in figure 4.9. For the majority of spots the signal is an order of magnitude higher than the background.

Figure 4.10 shows the diffraction from silicon shocked along the [001] direction. The drive pulse energy was 16 J in a 1 mm square spot, over 5ns ($\sim 3\times10^{11}\,\mathrm{Wcm^{-2}}$). The x-ray pulse was timed with a 1 ns delay and collimated using a 600 μm ap-

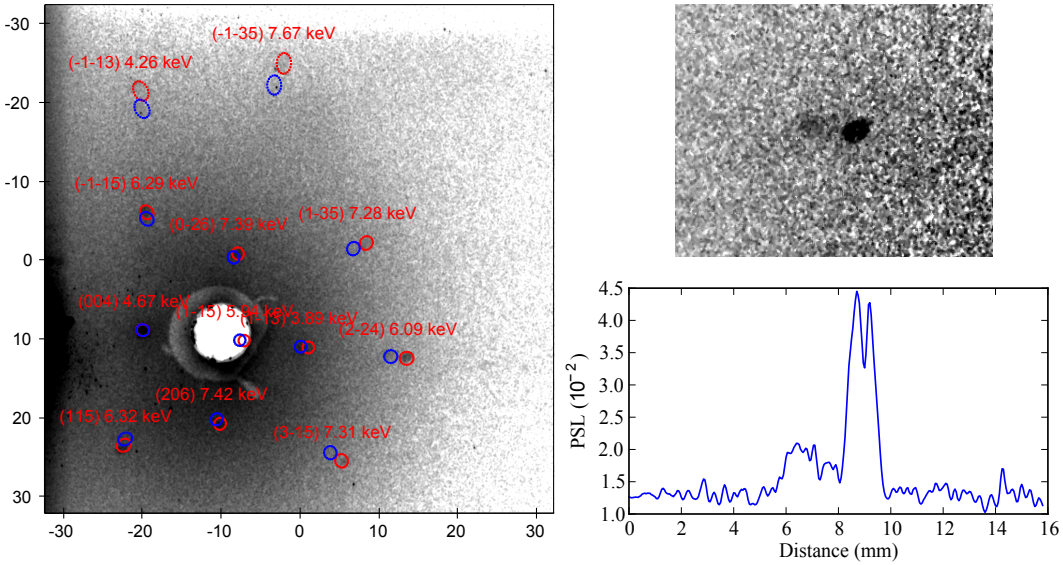


Figure 4.10: Diffraction from shocked silicon. Red indicates the diffraction pattern from the undriven region, blue indicates diffraction from the shocked region of the crystal. The enlargement shows the $(2\bar{2}4)$ peak (6.09 keV), with both shocked and unshocked spots visible. The plot shows a lineout through the two spots.

perture. Diffraction from both unshocked and shocked regions of the crystal is visible for several planes.

Analysis of the positions of spots corresponding to the shocked and unshocked crystal implies that the crystal was uniaxially compressed by $5(\pm1)\%$. Under uniaxial compression the planes rotate towards the surface normal and in the diffraction pattern the peaks shift towards the (002) peak. This compression is consistent with stresses inferred from VISAR measurements of the rear surface velocity of the target [92]. The V/V_0 assuming elastic compression are plotted against pressure in figure 4.11.

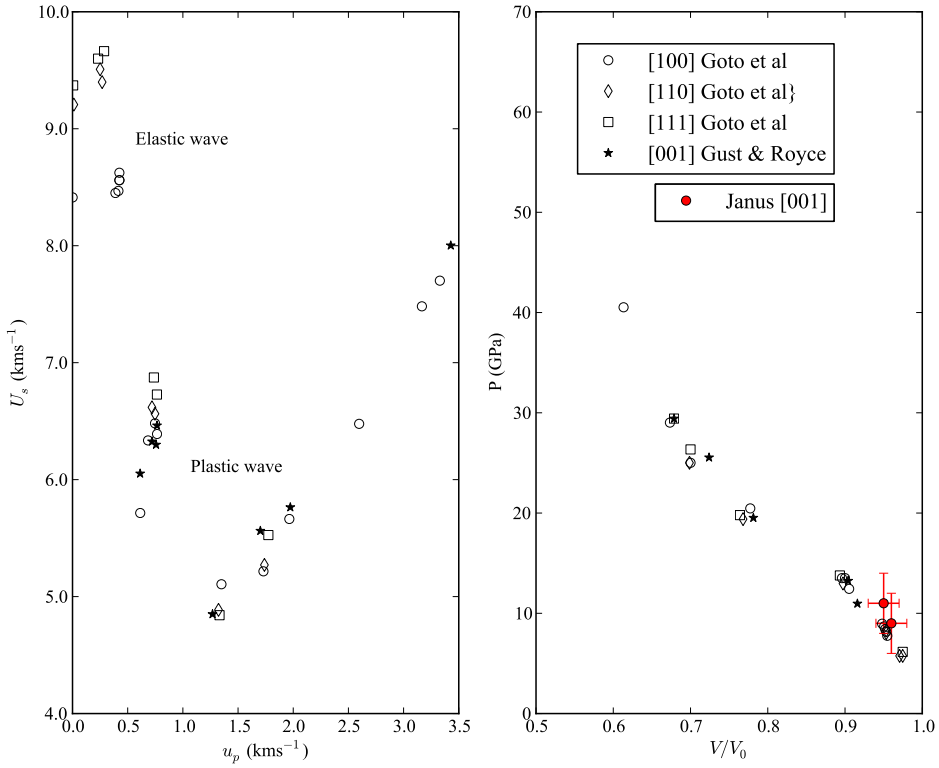


Figure 4.11: U_s-U_p plot and pressure against V/V_0 plot from Goto *et al* [93] with data from Gust & Royce [92], and two data points from this work. Since the shock velocity was not measured there is no data to add to the left hand plot.

4.3 Copper

After developing and testing the technique with silicon the focus was shifted to copper, where it was hoped there would evidence of microstructure in the diffraction pattern. Copper as a shock compressed material has been extensively studied via recovered target [95], *in situ* TXRD [19], and MD [96] experiments.

In recovered targets, electron microscopy studies have revealed a diverse variety of post-shock microstructures including cellular dislocation structures, stacking faults, and twins [97]. Focusing on data where the loading orientation is along the [001] crystal axis, since this is the orientation for the majority of the data taken at Janus, there are a number of observed post-shock defect structures and pressure dependencies. For laser-driven shocks in the pressure range 12-20 GPa the post-shock microstructue has been observed to consist of a cellular organisation of $\frac{1}{2}\langle 110\rangle$ dislocations [43]. At 20-40 GPa, large numbers of stacking faults are observed, with far fewer dislocation cell structures. At higher pressures, micro-twins are observed in addition to profuse stacking faults and slip bands. The insight gained in post-shock studies is fundamentally limited by the dynamic release, the rarefaction wave altering the microstructure that was present under peak compression. The shock wave generates significant heating and recovered targets will be thermally annealed. Post-shock methods are also fundamentally limited to pressures where the release pathway is not through the liquid phase, where all information is lost on melting. Although these high pressures were not attained in the results discussed here, with more development, *in situ* techniques such as white-light Laue will be the only option at pressures that recover through melt.

The stacking faults observed in recovery experiments are the dominant defect

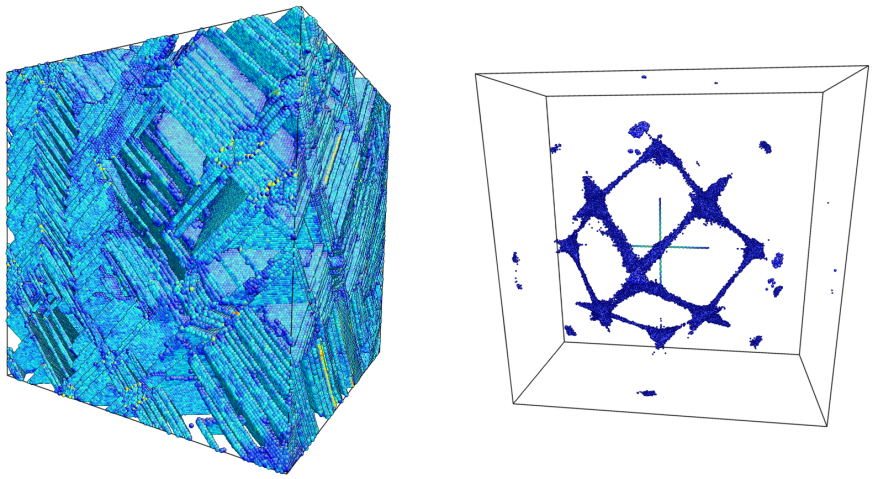


Figure 4.12: Stacking faults in MD and resulting FT. The left image shows real space, atoms coloured and thresholded by CSP to show only stacking faults, which dominate. The right image shows the 3D FT, thresholded by intensity, for k-points in the region $-3 < kx \leq 3$, $-3 < ky \leq 3$ and $0 < kz \leq 3$. The streaking between the peaks is due to the stacking faults.

in MD simulations of shocks in fcc materials such as copper. This is because the stacking fault energy (SFE) is usually very low for the potentials used in such simulations. Shock waves in the [001] direction generate Shockley partial dislocations which encompass a disc of stacking faulted material, and the SFE is low enough that the second partial dislocation is not emitted, so there are no full dislocations. The partial dislocations flow through the periodic boundaries and rapidly generate high densities of stacking faults. The density of stacking faults is 2-3 orders of magnitude greater than those reported in the recovered samples [96]. The partials are highly mobile, following the shock front, such that there is no distinct elastic and plastic waves and the shock is always overdriven. The behaviour for shocks in the [110] and [111] orientations is different, the second partials are emitted and full dislocations are generated [98].

In reciprocal space, the high density of stacking faults results in streaking of the peaks in a 'rod-like' intensity distributions, see figure 4.12. The full treat-

ment for calculating the intensity distributions is presented in Warren (1969) and extended by Veletrop *et al* [24, 99]. The broadening of the peaks is directly related to the average perpendicular separation of the stacking faults. The key result is that the influence of the stacking faults in reciprocal space is limited to directions perpendicular to the stacking fault planes. In the case of fcc stacking faults, the {111} planes. In terms of a Laue pattern the result would be streaking of the peaks in the ⟨111⟩ directions projected onto the image plane. If streaking was observed, it could be measured and related to the separation of the stacking faults, or compared with the FT from MD, providing an elusive measurement of *in situ* defect density.

4.3.1 Copper target characterisation

The initial defect density and microstructure of the copper targets were characterised by Kerstin Jurkschat from the Materials Science Department, University of Oxford. Focused ion beam (FIB) cuts were made into the crystal surface to form 6μm deep 100 nm thick slices as shown in figure 4.13. Slices were taken parallel to the [100] axis and at 45°.

As expected, the samples were single crystalline with no observable structures due to the growth technique. The potential for some sort of columnar growth structure, as observed in another experiment using single crystal tantalum, was suggested as a source of the observed *in situ* diffraction pattern. No columnar structure was observed during electron microscopy. The dislocations were typically 2-300 nm in length and there was no preferred orientation or arrangement. The observed dislocation density was $10^8\,\mathrm{cm}^{-2}$, typical for an undeformed crystal.

Additionally, the crystal surface orientation was mapped using EBSD. Apart from regions of the crystal that had delaminated from the NaCl substrate, the

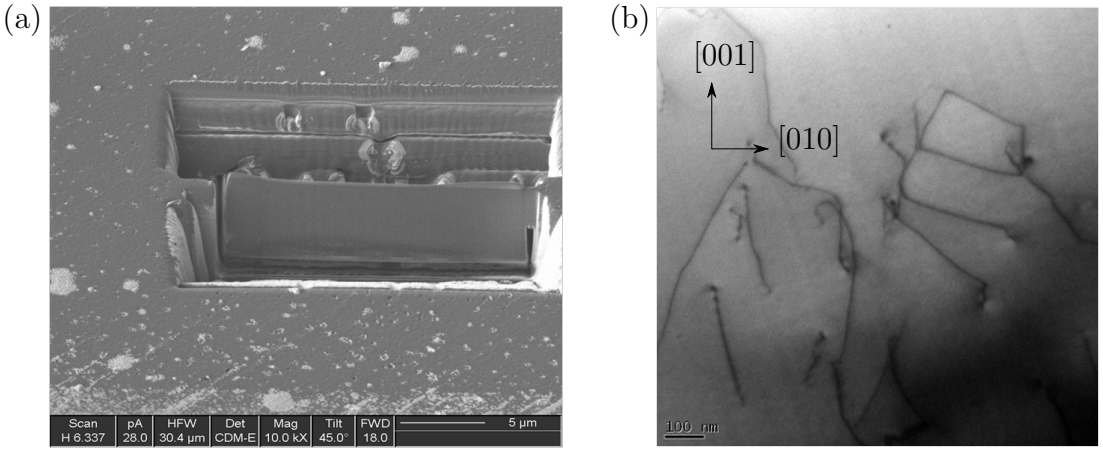


Figure 4.13: Copper single crystal characterisation. (a) Image of the sample slice cut by the focused ion beam (FIB). The surface debris are remnants of the plastic ablation coating. (b) TEM image of dislocations in the FIB slice.

misorientation from the [001] axis was within 0.25°.

4.3.2 Drive pressure

The drive pressures were calculated using VISAR data and the impedance-matching technique described in section 3.4. Figure 4.14 shows a plot of the measured peak pressure against incident laser intensity. The data points for both VISAR beds are shown for the 2010 experiment and data from VISAR A is shown for 2011. For some shots, the data quality on one VISAR bed was not sufficient for an adequate measurement of free surface velocity, due to poor alignment. For shots where both measurements were possible, both data points are plotted. Additionally the relationship between incident laser beam intensity and pressure by Lindl *et al* is plotted [100]. This gives the pressure as

$$P_{\mathrm{GPa}} \simeq 4000 \left[\frac{10^{-12} I}{\lambda} \right]^{2/3} \tag{4.1}$$

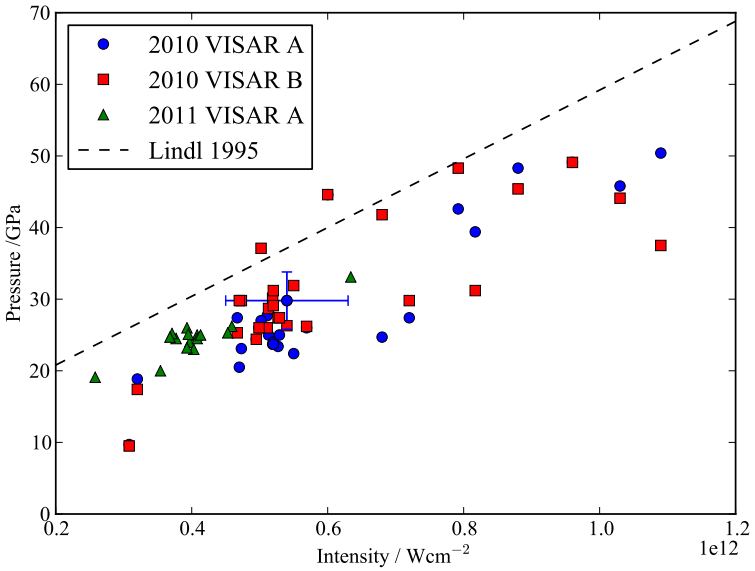


Figure 4.14: Plot of peak pressure versus incident drive intensity. The relation given by Lindl [100] is also shown. Typical error bars are shown for one point.

where P_{GPa} is the pressure in GPa, I is the laser intensity in units of Wcm^{-2}, and λ is the laser wavelength in nm. This relationship overestimates the drive pressure in comparison with the data. The difference is of order 10 GPa but the general trend is the same, and this gives us some confidence in the calculations of pressure from the VISAR velocity profiles. The HEL for single crystal copper is of order 5 GPa for shocks in the [001] direction, which is exceeded by all the shots, and therefore all the data is in the plastic regime [101].

4.3.3 Diffraction data

Figure 4.15 shows a representative white-light Laue pattern recorded at JANUS, for copper shocked along the [001] axis. The diffraction peaks are all in reflection rather than transmission and the other two image plates do not record any diffraction peaks. The crystal was typically rotated by 30° about the vertical

axis, resulting in the (002) lying on the left image plate. This peak is sometimes referred to as the 'basal' plane peak, since it is parallel to the crystal surface, although strictly speaking the cubic structure does not have a basal plane. The (002) is typically one of the strongest peaks as it is the lowest energy, where the x-ray source is brighter. The (202) and (113) are also relatively strong, with energies less than 6 keV where the spectrum still shows a large signal. Above 6 keV there are still several visible peaks but they are increasingly weak.

When the copper is driven, diffuse peaks appear around several peaks, in the data shown in figure 4.15 they are visible around the (002), (113), and (202) peaks. These extra peaks were not observed in static Laue patterns of these crystals, measured in a standard Laue rig and in the Janus set-up with no drive pulse.

There was some concern that the diffuse peaks may be in some way related to the drive laser spot. The fourfold directional nature of the peaks matches the symmetry of the square drive spot, and perhaps there was some sort of edge effect at play. The suggestion being that extra peaks may be diffraction from the interface between the shocked and unshocked region at the four edges of the drive spot. Figure 4.16 shows diffraction data for two shots with the same nominal drive energy. The orientation of the drive spot is fixed by the orientation of the phase plate for both shots. The difference between the two shots is the orientation of the target crystal in terms of rotation about the surface normal, the lower shot is rotated by 31° about [001] with respect to the orientation in the upper shot. The positions of the diffuse peaks are highlighted and show that the orientation changes with the crystal as it is rotated. If the extra peaks were related to the drive spot we would expect that their orientation would remain fixed in position at the edges (or corners) of the drive spot.

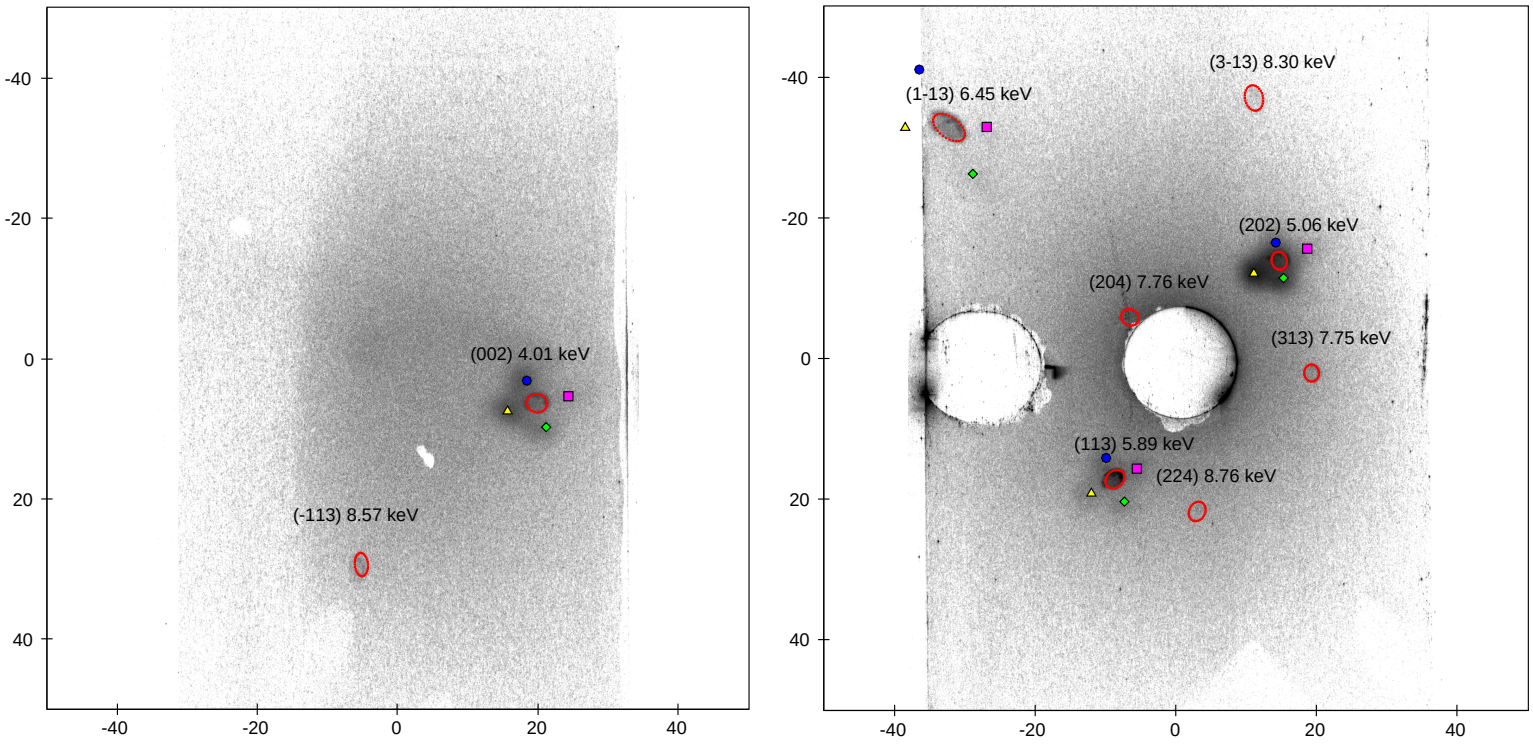


Figure 4.15: Typical diffraction data from copper shocked along the [001] axis. In 3d the left image plate is at 90° to the right image plate. The red outlines indicate the fitted pattern for the undriven crystal. Diffuse peaks are visible for the (002), (113), and (202) planes. The blue circles, green diamonds, pink squares, and yellow triangles show the peaks for rotations of the undriven orientation about the [100] and [010] crystal axes.

For several shots, the square phase plate was replaced with a circular phase plate. This did not have a noticeable effect on the typical diffraction shown in figure 4.16. The change in drive spot shape was not observable in the shocked peaks due to the diffuse nature of the peaks. These two results are compelling evidence that the extra peaks are not related to edge effects of the drive spot.

The fact that the extra peaks are centred on the undriven peak positions implies that the compression is hydrostatic or close to it. If there was a large residual strain anisotropy ($\epsilon_{xx} \neq \epsilon_{zz}$), the peaks would all be shifted towards the (002), in the same way as the silicon discussed earlier. The fact that there are extra peaks around the (002) peak itself, which is not shifted by uniaxial compression, is conclusive evidence that the peaks are due to plastic response and not an elastic effect.

The most important qualitative result to note is the orientation of the diffuse peaks. After fitting the diffraction pattern for the undriven crystal, the orientation of the peaks can be related to the crystallographic axes. The diffuse peaks lie in the [100], [$\bar{1}$00], [010], and [0$\bar{1}$0] directions, or directions which project onto these directions in the image plane, i.e. [10z], [$\bar{1}$0z], [01z], and [0$\bar{1}z$] where z is unknown. These directions are at 45° to the directions expected for stacking faults, which as described earlier, produce streaking in the $\langle 111 \rangle$ directions, and therefore the diffuse peaks are not due to stacking faults.

The positions of the peaks also appear to be incompatible with $\{111\}$ twinning or microtwinning as observed in recovered targets. Twinning on the $\{111\}$ is equivalent to a 180° rotation about the $\langle 112 \rangle$ directions, or rotation about the $\langle 110 \rangle$ directions. Peaks due to twin formation would lie in the same directions as the streaking due to stacking faults. Not only are the peaks in a different direction but the displacement from the original position is much smaller than

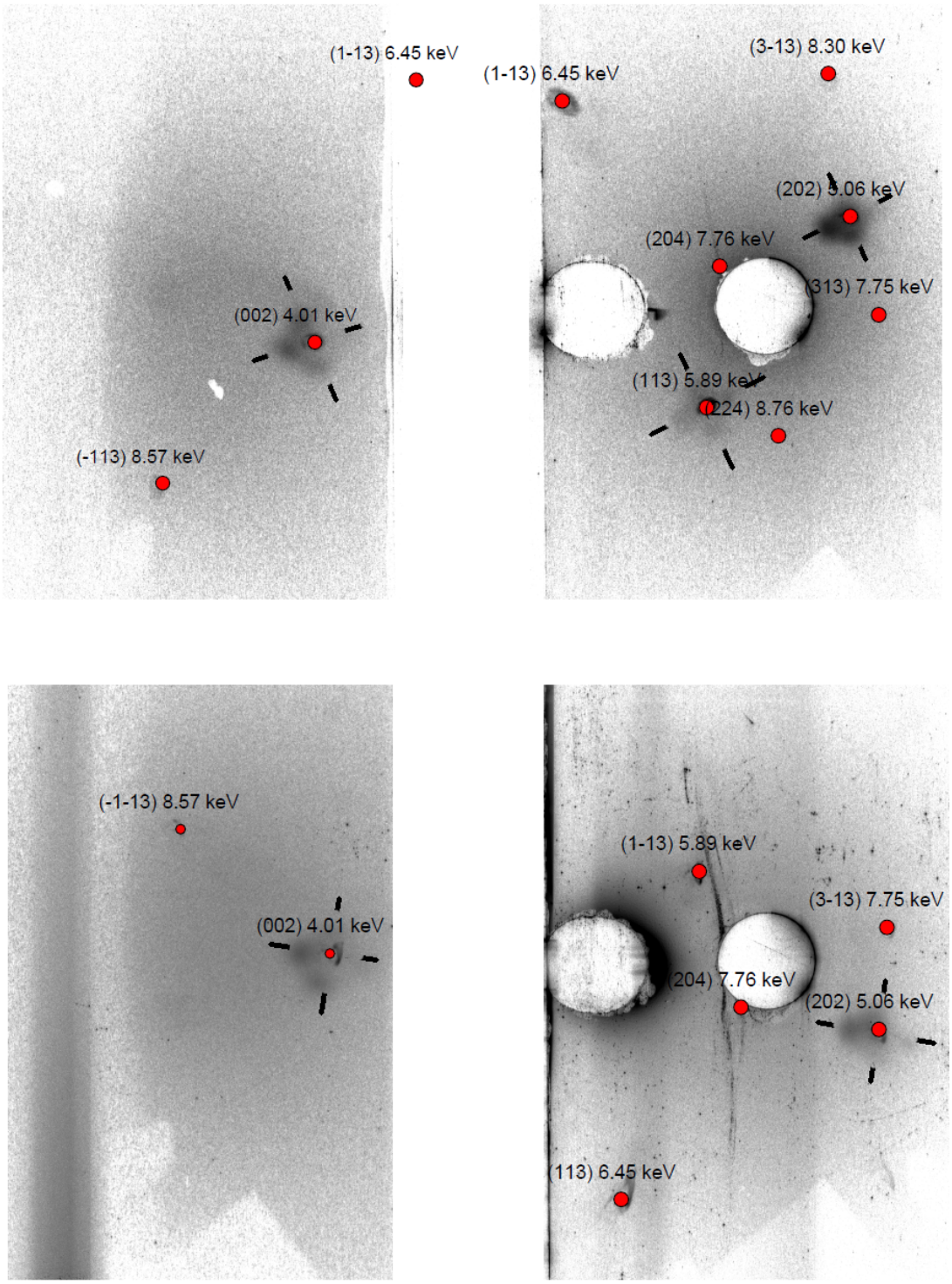


Figure 4.16: Elimination of drive orientation as the source of the extra peaks. The top two images show two plates from one shot, the bottom two images show two plates from a second shot. The drive orientation is fixed for both shots. The crystal in the second shot is rotated by 31° about the [001] surface normal, with respect to the first shot.

would be expected for twinning. Figure 4.17 shows the plotted positions for twins on the (111), ($1\bar{1}1$), ($\bar{1}11$), and ($\bar{1}\bar{1}1$) planes. The lack of evidence for twinning might be expected considering the observations in recovered targets, as for laser-driven shocks, high densities of micro-twins were observed for samples shocked in the 55-60GPa pressure range, which is at or above the pressure range in this experiment.

The peaks are best fitted by positive and negative rotations of the crystal about the [100] and [010] crystal axes. Using a single rotation angle, the magnitude of the peak displacement (from the undriven crystal peaks) is matched for those peaks where diffuse features are visible. If the diffuse features were due to a directional broadening (like the effect of stacking faults), the projection of the broadened peak onto the image plate is different for different peaks. This can be imagined as dressing the Laue peaks by the addition of scattering vectors $\mathbf{q}$ to the reciprocal lattice vectors. Fitting the pattern by adding $\mathbf{q}$-vectors in the [100] and [010] directions does not fit the displacements of the diffuse features for all the peaks. This supports the idea that the peaks are due to rotated crystal domains rather than directional broadening of the peaks.

Note that the diffuse peaks are also observed with free standing crystals, where the NaCl substrate is removed, which doesn't affect the data. Additionally, the same results were achieved using the millimeter-scale 'thick' crystals grown via Czochralski method. Although it might be expected that these crystal might have a higher initial dislocation density than the PVD crystals (due to cutting and electropolishing the surfaces), characterisation via TEM revealed a similar dislocation density to the PVD crystals. Since VISAR measurements were not possible for these thicker crystals, preventing any estimate of pressure, relatively few data points were taken with these crystals. There were no differences of note

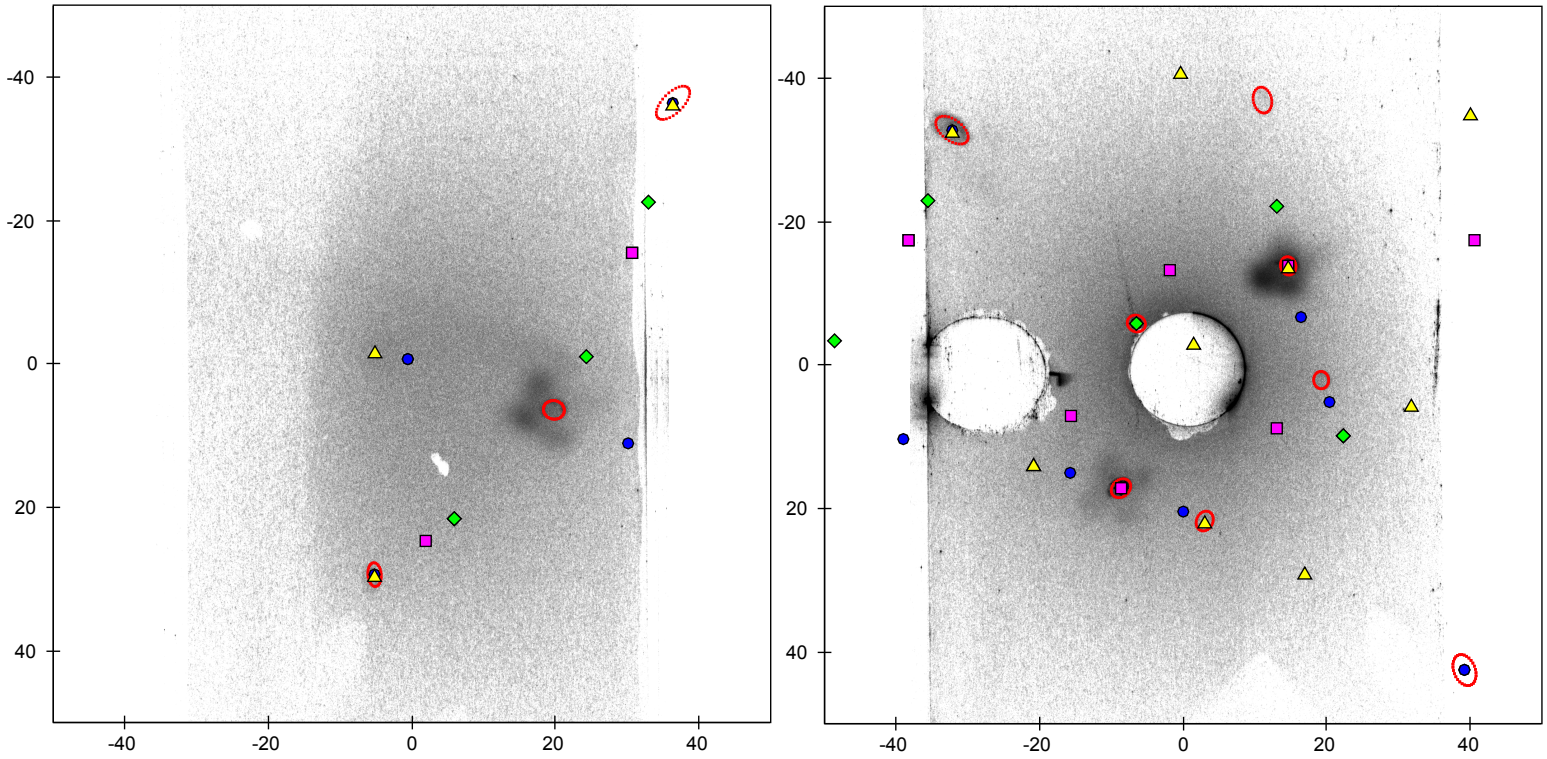


Figure 4.17: Twin positions. Red outlines correspond to the pattern for the undriven crystal. Blue circles, green diamonds, pink squares, and yellow triangles correspond to twins on the (111), $(1\bar{1}1)$, $(\bar{1}11)$, and $(\bar{1}\bar{1}1)$ planes respectively.

in the data recorded for these crystals and the PVD crystals. Therefore, the features are not due to an inherent pathology of the crystals.

4.3.4 MD simulations

As discussed earlier, the FT of the stacking faulted material from an MD simulation is dominated by the streaking in the $\langle 111 \rangle$ directions, but is there evidence of lattice rotation? Lattice rotations have been observed in previous MD studies of shocks in fcc crystals before (ref [102]), however, it was largely ignored. Slip in the $[11\bar{2}]$ directions on the $\{111\}$ planes has the largest Schmid factor of the three partial slip directions available for those planes. The resulting lattice rotation expected to be about the $[\bar{1}10]$ axis, the axis perpendicular to both the glide plane and the slip direction (ref [103]).

Shock simulations were performed using the Mishin EAM potential [47]. Shocks were applied by driving a thin 'piston' region at one end of the sample with a fixed velocity U_p in the [001] direction, producing the typical profuse generation of stacking faults. Small rotations of the crystal between stacking faults are observable in the real space visualisation of shocked crystal. For small simulation cross-sections (20×20 unit cells) of copper, shocked just above the MD HEL (24 GPa), only one stacking fault is generated which then propagates through the periodic boundaries transverse to the shock direction. If the stacking fault plane activated is the the $(\bar{1}11)$ for example, the resulting rotation is about $[\bar{1}\bar{1}0]$ axis. Similarly, if the $(\bar{1}\bar{1}1)$ plane is activated, the observed rotation is about the $[1\bar{1}0]$ axis. For larger simulation cross-sections, multiple slip systems are activated and the rotations combine. For simulations with a cross-section of 40×40 unit cells, both slip systems are activated and the overall lattice rotation axis is approximately [010]. The rotations of the lattice are measured by calculating the FT for

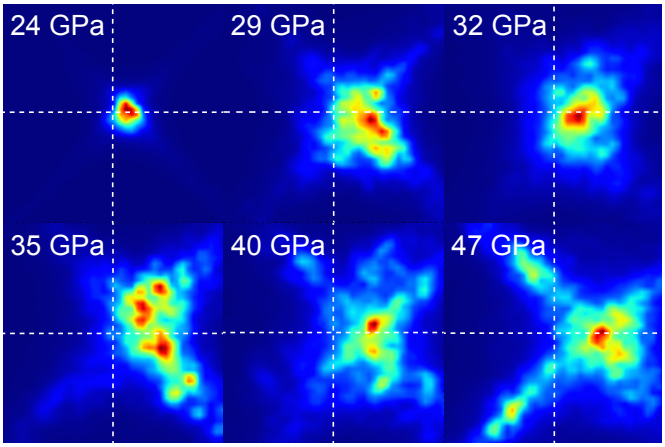


Figure 4.18: MD simulation for shocks along [001] in Cu (Mishin potential), (002) peak projected in direct back reflection. The peaks broaden in a cross shape due to the stacking faults. The peaks are highly textured but observed to rotate resulting in a shift of the whole peak.

a sample region and measuring the reciprocal lattice point rotations. Figure 4.18 shows the (002) peak for simulations at a range of pressures.

Simulations using larger cross-sections (100×100 unit cells) were carried out for a range of applied pressures from 22-47 GPa, which corresponds to the applied piston velocities of $U_p = 0.6$ - $1.0\,\mathrm{kms}^{-1}$, with repeat simulations carried out at each pressure using a different random thermal seed. As expected, the density of stacking faults increases with pressure, as shown in fig 4.19. The magnitude of the lattice rotations, measured using the Fourier transform, shows large variation, although there is a slight trend for increased rotation angle with increasing pressure. Although the measured rotation axis is close to the [100] or [010] for some of the simulations, it is not consistent. The (002) peaks shown in figure 4.18 show peaks which have all shifted to the right to demonstrate the effect but this is not always the case. With increasing pressure, the peak is increasingly diffuse and streaked due to the increased stacking fault density.

For simulations with 100×100 unit cells, the overall shift is always in one direc-

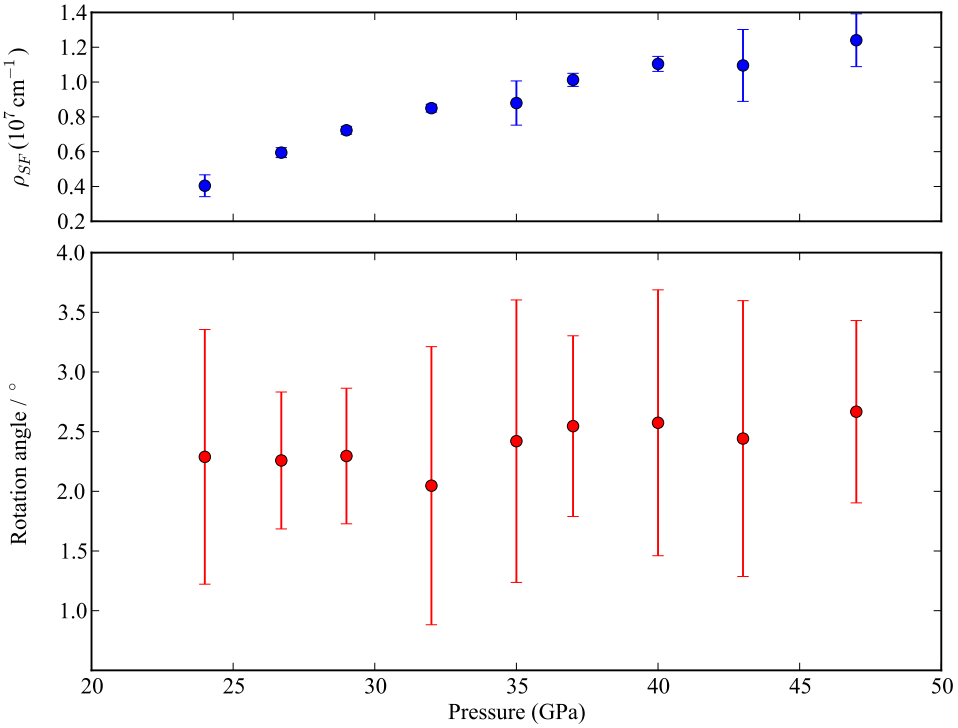


Figure 4.19: Stacking fault densities and rotation angles for 100 × 100 unit cell cross-section simulations. The mean values for 10 simulations at each pressure are plotted with error bars given by the standard deviations.

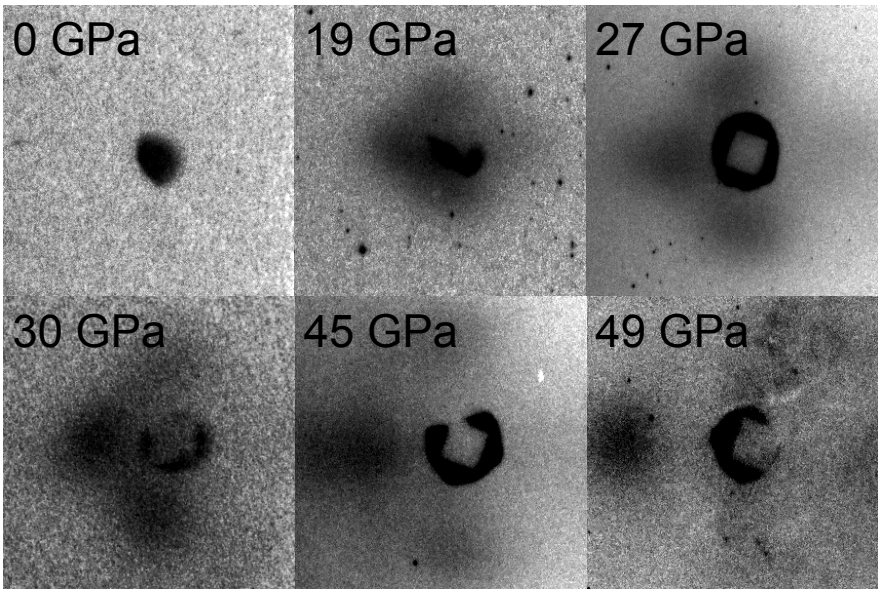


Figure 4.20: (002) diffraction peaks for 0-49 GPa, showing the increase in separation of the diffuse features with pressure. The bright spot in the centre is due to the undriven crystal, with the square drive spot particularly clear in several of the data images. Figure reproduced from [23].

tion rather than a fourfold splitting about the original position. It was suspected that the small cross-section, limiting the number of activated slip systems, was preventing multiple rotation orientations. However, when the simulation cross-section was increased (250×250 unit cells was sufficient), the observed rotations are averaged out and there is no overall rotation of the reciprocal lattice. The MD simulations certainly do not capture the physics which generates the diffuse features.

4.3.5 Lattice rotations

Interpreting the diffuse peaks as micro-structural lattice rotations, the magnitude of the rotation angle is seen to increase with increased peak pressure. Figure 4.20 shows the (002) for six different drive pressures. At higher pressure the distance between the diffuse peaks and the square driven region is increased.

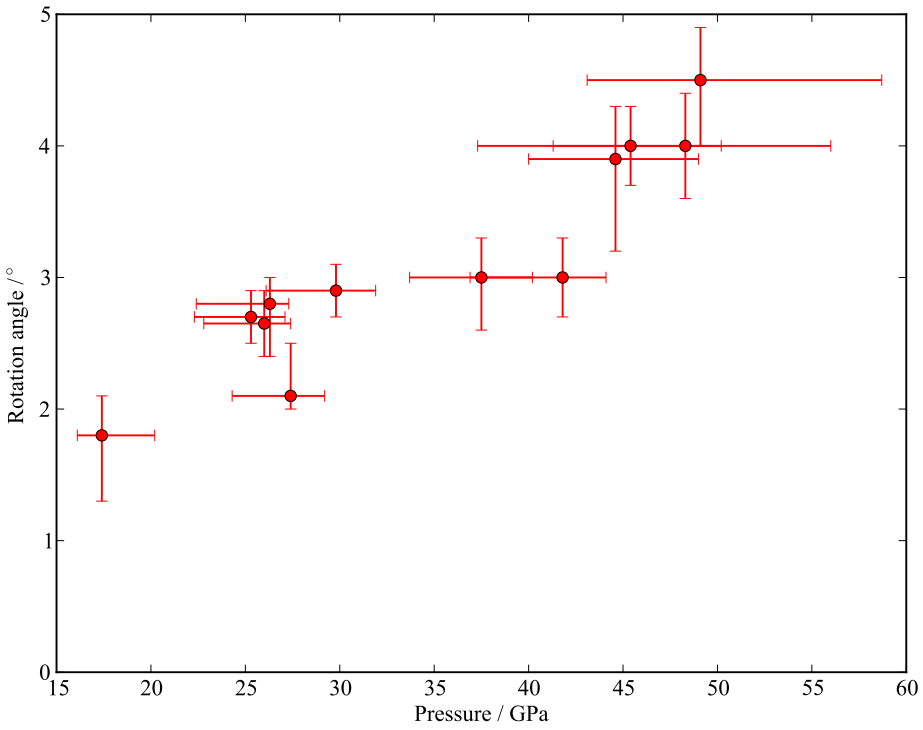


Figure 4.21: Plot of lattice rotation angle against peak pressure. Figure reproduced from [23].

The measured angles are plotted against pressure in figure 4.21. The mean angle is taken for all visible diffuse peaks, with error bars corresponding to the minimum and maximum fitted rotation angles. The pressure errors are calculated using the standard deviation of the fringe shift, converting to velocity, and hence pressure, then taking the minimum and maximum values during the x-ray pulse.

If the rotation is due to slip, the increased angle indicates an increased amount of slip possibly inferring an increased dislocation density. The idea of slip rotation is illustrated in figure 4.22. Under uniaxial tension or compression, slip occurs on the slip plane with the greatest resolved shear stress, given by the Schmid factor. If the two ends of the bar shown in figure 4.22 are unconstrained, slip

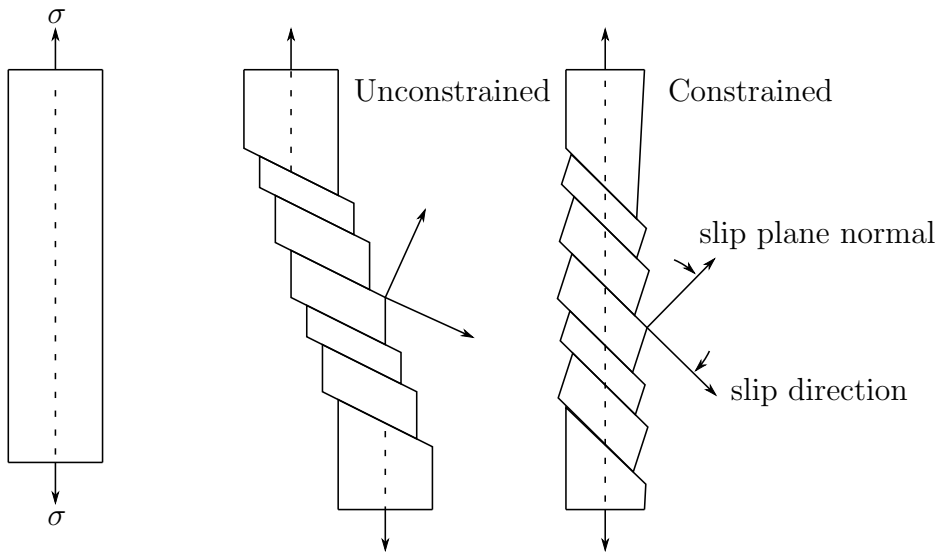


Figure 4.22: Slip rotation under confined strain.

results in a displacement of the two ends transverse to the loading axis. If the two ends are constrained to stay on the loading axis, in a quasi-static test this would be by friction or a channel die, then the crystal lattice rotates relative to the loading axis. The loading conditions of a planar shock wave are represented by the constrained condition.

In tension, the slip direction rotates towards the loading axis [27]. This effect is regularly used in static deformation tests to determine the active slip system, and is often visualised on a stereographic projection as seen in figure 4.23. The projection of the loading axis is plotted with respect to the crystal axes even though it is the crystal which actually rotates. In compression, the normal to the slip plane rotates towards the compression axis [103, 104]. For an fcc crystal, if the compression axis lies in the [001]-[101]-[111] triangle of a stereographic projection, the slip system with the highest Schmid factor is the $(1\bar{1}1)$ plane and slip in the $[0\bar{1}1]$ direction, given by d1 in table 4.1. The compression axis rotates towards $[1\bar{1}1]$ direction, or in reality, the equivalent rotation of the crystal towards the

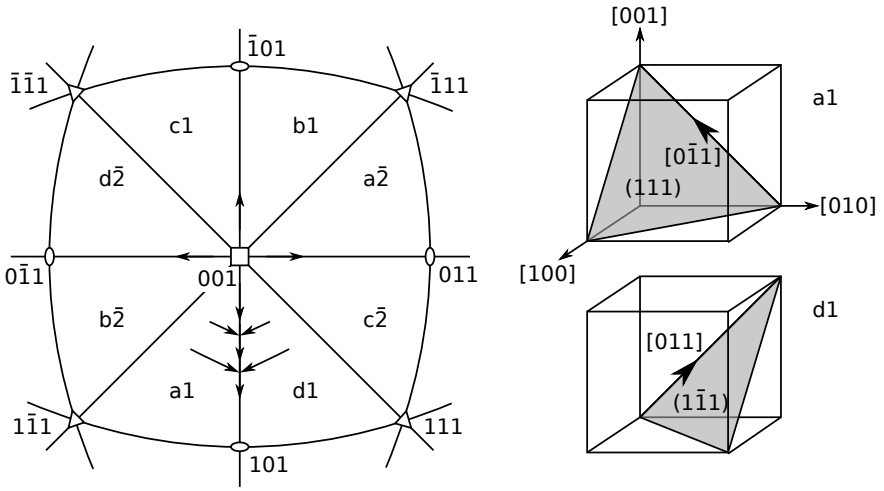


Figure 4.23: Stereographic projection for cubic crystals. The slip systems for fcc crystals are indicated and the corresponding slip planes and directions given in table 4.1. Figure is from [23].

loading axis.

If the loading axis lies on the $[001] - [101]$ symmetry line, the Schmid factors for $(1\bar{1}1)[011]$ and $(111)[0\bar{1}1]$ are equal. Equal slip on both systems results in the compression axis rotating towards [101]. This is called *conjugate* or *double* slip and is indicated by the arrows in figure 4.23. For compression along [001], the four $\{111\}$ planes are equally favoured. Slip on one of the planes causes a rotation towards the slip plane normal, and slip on the conjugate plane becomes more favourable. The rotations caused by conjugate slip are then equivalent to lattice rotations about the [100] and [010] axes, matching the directions in the data.

This splitting of the peak into four groups resembles the interpretation given by Zaretsky for diffraction data from shock compressed single crystal NaCl [104]. In the case of NaCl, the likely slip system in operation is the $\{110\}\langle 110\rangle$-system. One-dimensional compression and shear on these glide planes result in the ro-

Plane	Direction	System
(111)	$[0\bar{1}1]$	a1
	$[\bar{1}01]$	a$\bar{2}$
$(\bar{1}\bar{1}1)$	[011]	b1
	[101]	b$\bar{2}$
$(\bar{1}11)$	$[0\bar{1}1]$	c1
	[101]	c$\bar{2}$
$(1\bar{1}1)$	[011]	d1
	$[\bar{1}01]$	d$\bar{2}$

Table 4.1: The slip systems for an fcc crystal indicated in figure 4.23 [105].

tation of the lattice from the original orientation. Zaretsky describes a scheme whereby the loaded crystal is divided into uniformly sized domains with four unique orientations, with misorientation about the [010] and [001] crystal axes. The NaCl was loaded along the [100] directions so these axes of misorientation are equivalent to the axes we have observed for copper loaded along [001]. For fcc crystals such as copper, the active slip system is expected to be the $\{111\}\langle 110\rangle$-system. Although the slip system differs from NaCl, I suggest that a similar scheme of one-dimensional compression followed by slip, results in the lattice rotations that were observed. Zaretsky's measurements were via a monochromatic technique and the actual spatial orientations were not observed as in the data presented here. Lattice rotations of comparable magnitude have been observed in recovered shocked crystals of NiAl [106], and have also been shown to play an important role in dislocation dynamics simulations [107, 108].

Inferring a dislocation density from the rotation angle requires several assumptions. If we assume that there is equal glide on conjugate slip systems the full treatment for the rotation due to double slip is given by Bowen & Christian [109]. The rotation angle can be directly related to the amount of slip on the two

glide planes and is given by:

$$\gamma = \frac{2}{\boldsymbol{\beta}_1 \cdot \mathbf{n_2}} \ln\left(1 + \frac{\boldsymbol{\beta}_1 \cdot \mathbf{n_2}}{|\mathbf{n}|} \frac{\sin\alpha_0}{\cos\lambda_0}(\cot\alpha - \cot\alpha_0)\right) \tag{4.2}$$

The derivation of this equation is given in appendix 6.2. The glide on both systems is taken to be equal and given by γ. The two slip systems have slip plane normals defined by the unit vectors $\mathbf{n_1}$ and $\mathbf{n_2}$, and slip directions given by unit vectors $\boldsymbol{\beta}_1$ and $\boldsymbol{\beta}_2$. The angles α_0 and α are the initial and final angles between the loading axis and the direction given by the sum of the two slip plane normals, $\mathbf{n} = \mathbf{n_1} + \mathbf{n_2}$. The angles λ and λ_0 are the initial and final angles between the loading axis and the slip directions (equal for both systems). Using this equation, the value γ can be calculated for a pair of conjugate slip systems and a given rotation angle. The next assumption is that the dislocations travel no more than a few tens of nanometers, which at the expected strain rates around $10^{10}\,\mathrm{s}^{-1}$ is consistent with subsonic dislocation motion [110]. If this distance is denoted p, the dislocation density can be estimated by:

$$\rho_d = \frac{2\tan\gamma}{pb} \tag{4.3}$$

where b is the Burgers vector. If the assumption is made that p is no more than a few tens of nanometers, the inferred dislocations densities, for the observed rotation angles, are of order $10^{12}\,\mathrm{cm}^{-2}$. This order of magnitude is consistent with the defect densities predicted by Orowan's equation (2.36) and simulated in large-scale MD simulations, where defect densities of $10^{12} - 10^{13}\,\mathrm{cm}^{-2}$ are observed, even if they aren't telling the full story [96, 111, 112].

4.4 Summary

The copper diffraction data represent the first *in situ* Laue patterns recorded during shock compression of copper. The observed diffuse peaks are in directions which project onto the [100] and [010] crystal lattice vectors, and, as such, are not in the directions that would be expected for broadening due to stacking faults, or the rotation due to twinning. The diffuse peaks are consistent with small-angle lattice rotations about the [100] and [010] axes. MD simulations of copper do not predict the diffuse features. The magnitude of the rotation increases with shock pressure, consistent with increased dislocation generation and slip. The rotation orientations suggest the action of conjugate slip systems and an inferred defect density of order $10^{12}\,\mathrm{cm}^{-2}$. These measurements provide the first direct evidence on nanosecond timescales of stress dependent lattice rotations in a shocked single crystal.

Chapter 5

Twinning in MD simulations of shocked tantalum

This chapter describes MD simulations and analysis investigating the shock compression of single-crystal tantalum along the [001] axis. This work was initially driven by concurrent experiments at Omega, led by Andrew Comley, utilizing the white-light Laue technique described in previous chapters to study shock-loaded single-crystal tantalum.

5.1 Background

As described earlier in this thesis, there has been extensive research into material response under shock loading. Much of this work has focused on fcc metals such as copper, like the experiment in the previous chapter, where plastic deformation is understood to be dominated by the generation and flow of dislocations. There is relatively less information about other deformation mechanisms such as shock-induced twinning. In standard deformation tests, twinning is a relatively

important deformation mechanism in bcc metals, especially at low temperatures and high strain rates [27]. Understanding these mechanisms at the high strain rates involved in shock compression is important for developing models which can make reliable predictions over a wide range of strain rates and pressures.

Generating and validating predictive models of compression under shock loading is of interest for various applications, especially heavier, high-Z materials such as tantalum. Although *in situ* x-ray diffraction experiments have proven to be a powerful technique for investigating these effects, there is not a great deal of data for these high-Z elements. This is largely due to the extra requirements imposed on the x-ray source. As the target material increases in atomic number and density, the x-ray absorption increases requiring brighter and higher energy x-ray sources to penetrate the sample. Generating these x-ray sources is difficult in itself, requiring larger laser systems such as Omega, and the experiments have to be designed with a great deal more shielding than the JANUS set-up of the previous chapter.

In terms of MD simulations, there is also relatively less work on shock compression in bcc materials. This is perhaps due to the lack of atomic potentials which succeed in describing non-close-packed metallic bonding. However, arguably the greatest success story for MD simulations of shock compression is the predicted $\alpha - \epsilon$ phase transition in Fe which has a bcc structure [9]. The mechanism for this transition involves an initial elastic uniaxial compression followed by a shuffle of alternate planes. This mechanism bears a resemblance to mechanism proposed later in this chapter for the observed twinning in MD simulations shock compressed tantalum. The results of the MD simulations of Fe shocked along the [001] axis were later observed experimentally via TXRD with good agreement [7, 113]. For shocks in other crystallographic directions the predictions are less

successful. Shocks along the [110] axis result in the formation of grains of fcc and hcp and these phases have not been observed experimentally [67]. The high orientation dependence for shocks in single-crystals is particularly evident in MD simulations, as discussed earlier with shocks in copper, and is relevant to the twinning mechanism discussed in this chapter.

The results discussed here are for shocks along the [001] axis in single-crystal tantalum, the aim being to compare MD simulations with the results of white-light Laue experiments on the Omega laser system at LLE. These experiments built on the technique developed in this thesis and were performed by a collaborative group from AWE, LLNL, and Oxford, lead by Andrew Comley [114]. Tantalum was the chosen target material as it acts as a surrogate for other high-Z materials which are important for defence applications. It is the complexity of the material as well as its atomic number which makes it a good surrogate for testing experimental platforms, modelling codes, and validation of those codes. It has multiple plasticity mechanisms; dislocation glide, deformation twinning, and phase transformations, which must all be built into the predictive models.

Although tantalum has proved to be a challenge for *in situ* x-ray diffraction experiments, numerous studies of recovered samples have been made. In single-crystals, dislocation activity and deformation twinning has been observed for shocks along multiple orientations, not just the [001] axis (ref [115]). The formation of twins was observed to have a strong pressure dependence, and different orientations developed varied twin fractions. Other recovery experiments have observed twinning and a metastable ω phase in shock loaded tantalum [116], and also observed strong orientation dependence. Shocks along the [110] axis did not produce observable twinning or phase transformed material. Earlier work focused on polycrystalline tantalum, explosively driven to peak pressures of up

to 45 GPa, which showed profuse twinning. The observed twins are on the {112}, but the twinning mechanism has not been discussed, the assumption being that the standard shearing mechanism as in section 2.1.6.3.

5.2 Simulations

The simulations were carried out with the LAMMPS code using the extended Finnis-Sinclair (EFS) potential [48]. The EFS potential was chosen as it provides a reasonable representation for the high pressure elastic constants without too great a computational cost. More advanced potentials such as the Model Generalised Pseudopotential Theory (MGPT) potential of Moriarty *et al* [117] have been designed with high-pressure applications in mind and have been shown to be more accurate at high pressures. However, the computational expense is far greater. In order to run a shock simulation for a reasonable time the simulation box has to to be sufficiently long in the shock direction. The size of the simulation box in the transverse directions is also important and small box cross-sections can inhibit behaviour such as defect nucleation. For the work discussed here, the sample size and simulation duration prohibited the use of the MGPT potential.

The EFS potential has a similar form to the EAM potential. Referring back to section 2.4.1, the pairwise term in the original FS potential is given by a quartic polynomial, which is replaced in the extended form by a sextic polynomial given by:

$$V_{EFS}(r) = \begin{cases} (r-c)^2(c_0 + c_1 r + c_2 r^2 + c_3 r^3 + c_4 r^4) & \text{for } r \leq r_c \\ 0 & \text{for } r > r_c \end{cases} \tag{5.1}$$

The parameters c_i are fitted for the material properties of the chosen element

and the cut-off r_c is chosen to lie between the second and third shell of neighbour atoms. The embedding type term is given by

$$\sqrt{n_i} = \left[\sum_{j \neq i}^{N} \rho(r_{ij}) \right]^{1/2} \tag{5.2}$$

where the electron density is calculated using:

$$\rho(r_{ij}) = \begin{cases} A^2(r_{ij} - d)^2 + B^2(r - d)^4 & \text{for } r \leq d \\ 0 & \text{for } r > d \end{cases} \tag{5.3}$$

The second cut-off parameter d is also chosen to lie between the second and third neighbours.

A variety of sample sizes and temperatures were used in the simulations. For the majority of the data discussed here, the sample size was $140 \times 140 \times 2000$ bcc unit cells ($46 \times 46 \times 660\,\text{nm}$, 80 million atoms), with the orientation of the sample such that the [001] axis is in the z-direction. The shock is generated in the z-direction and the boundaries are set to be periodic in the x and y directions. A shock wave was generated by freezing a 'piston' region of five atomic planes at one end of the sample and giving it a fixed velocity U_p. The velocity is applied instantaneously rather than using any form of small ramp. The system was then allowed to run until the shock wave reached the rear surface of the sample and began to release.

Figure 5.1 shows the Hugoniot for Ta for reference data ([118, 119]) and as calculated using the Ta EFS potential in these simulations. The small bump at $0.8\,\text{kms}^{-1}$ represents the HEL, below which all simulations responded elastically. At a piston velocity of $U_p = 0.8\,\text{kms}^{-1}$ the material begins to respond plastically reducing the shear stress. The HEL may be slightly lower, but $U_p = 0.8\,\text{kms}^{-1}$ is

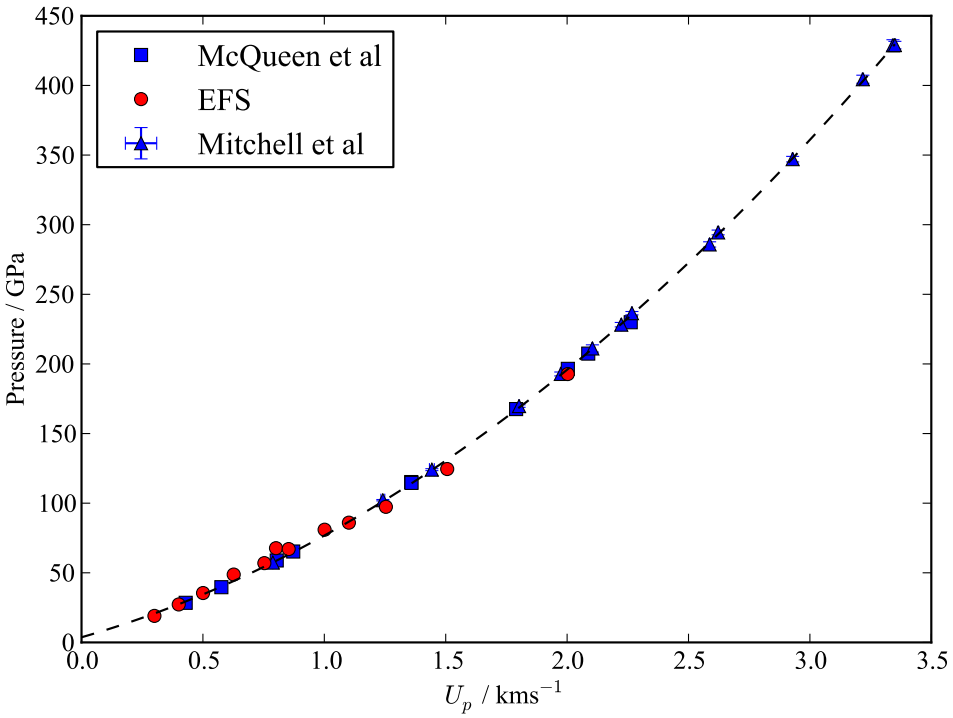


Figure 5.1: Hugoniot for Ta EFS potential and experimental data. Reference data is from McQueen *et al* [118] and Mitchell *et al* [119]. The dashed line is fitted to the reference data. Only one simulation was performed for each piston velocity so no error bars are shown for the EFS points.

certainly close as for smaller simulation cross-sections e.g. 40×40 unit cells, the simulations did not always respond plastically.

Velocity and stress profiles are shown in figure 5.2 for piston velocities of $0.8\,\mathrm{kms}^{-1}$ and $0.9\,\mathrm{kms}^{-1}$. The velocity in the z direction is plotted for three timesteps at 75, 95, and 115ps after the piston starts moving, showing the two wave structure. The first wave is an elastic compression wave, which is then followed by the plastic wave where the shear stress is relieved. The pressure, P_{zz}, and the shear stress $P_{zz} - \frac{1}{2}(P_{xx} + P_{yy})$ are plotted for the timestep at 115 ps. At the second wave the shear stress reduces to close to zero.

These simulations were performed at a temperature of 5 K. Although this is rather low, the aim was to make identifying the twins less difficult. The simulations were repeated at 300 K with the same general result. The per atom structure factor method described in the subsequent section still identified the twins.

5.2.1 Fourier transform analysis

For fcc structures, the centro-symmetry parameter is an excellent tool for identifying dislocations and stacking faults. The CSP of the atoms in the stacking faults is the same as for hcp so it is differentiated from the bulk fcc material. For the bcc structure it is less successful. For these simulations, an initial visualisation using the CSP did not provide a great deal of information. There was a general increase in the CSP of the atoms in the region where the shear stress was reducing, but no obvious stacking faults or dislocations, as observed in copper say. Note that at this early stage we suspected twinning but had not demonstrated that it was actually occurring. The CSP, used with success with copper, was of no use. If the material twins, by definition, the structure does not

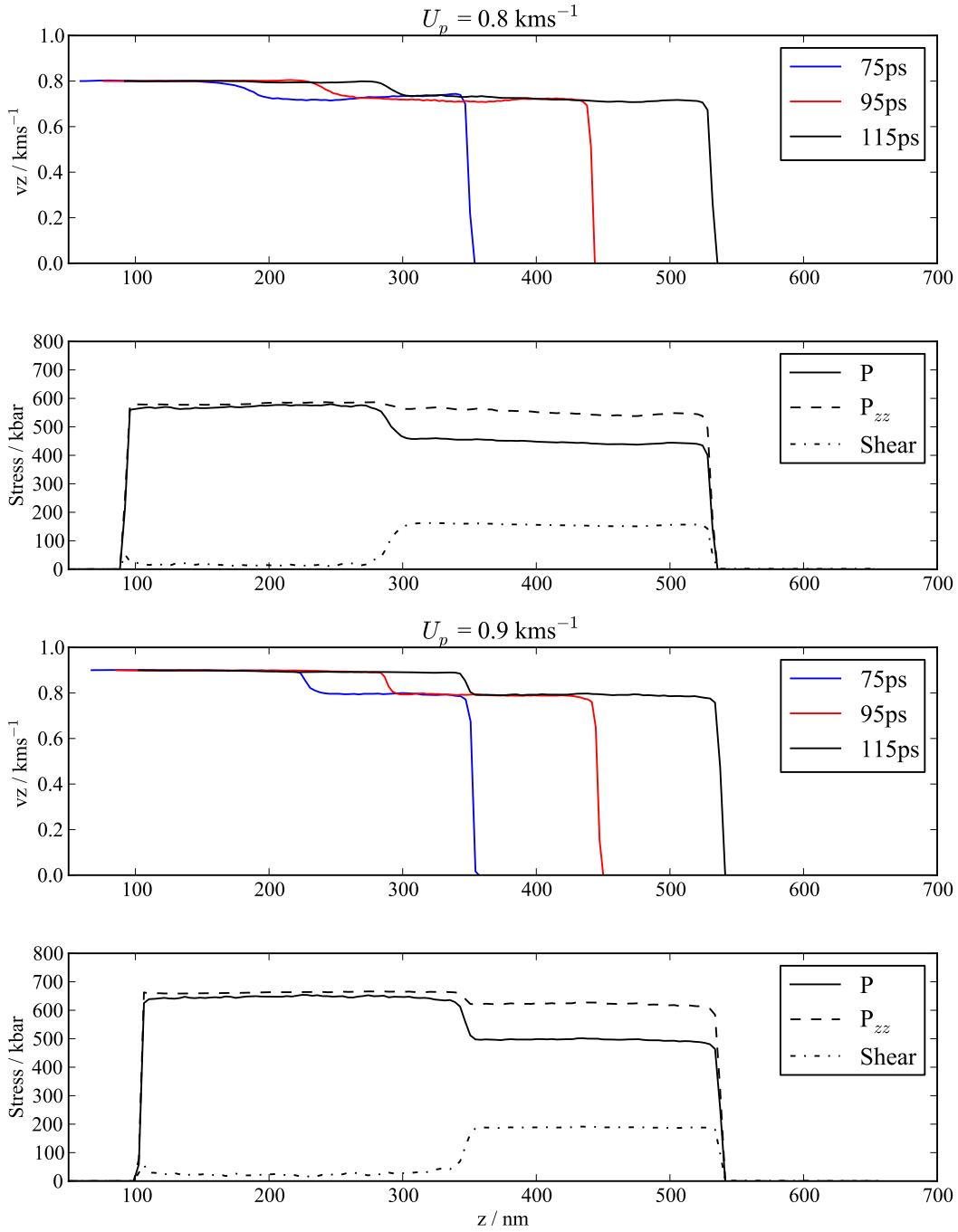


Figure 5.2: Wave profiles for shock along [001]. The upper two plots and the lower two plots correspond to piston velocities of 0.8 kms^{-1} and 0.9 kms^{-1} respectively.

change, and this is why CSP does not work.

Studying the Fourier transform (FT) of the plastically-deformed region showed a vast increase in the number of peaks. Figure 5.3 shows three slices from the three-dimensional (3D) FT of the region $200 < z \leq 250\,\text{nm}$, for the $U_p = 0.9\,\text{kms}^{-1}$ shock shown in figure 5.2. This range was chosen since the shear stress has reduced to minimum in this region. Ignoring the position of the peaks in the kz directions (which of course change with compression along z), the normal reciprocal lattice for bcc has peaks lying on integer values of kx and ky (in units of $2\pi/a$) and from figure 5.3 it is clear that there are many additional peaks not compatible with uniaxial compression.

The right hand plots in figure 5.3 show the positions of peaks for twins on the $\{112\}$ planes. 'Twin 0' corresponds to the original orientation and twins 1, 2, 3, and 4, correspond to twins on the $(\bar{1}\bar{1}2)$, $(1\bar{1}2)$, $(\bar{1}12)$, and (112) planes, respectively. It is important to note that the peak positions calculated here are not for an undeformed bcc structure. The strains used to fit the FT were calculated with hindsight after applying the per atom structure factor method discussed in the next section. The three slices shown are taken through planes where the analytical peaks lie. As they are quite close in the kz direction, the peaks from one slice are still observable in the adjacent slices.

5.2.2 Per atom structure factor

In order to identify and separate the twins in the simulation, we developed a new per atom order parameter based on the FT method, dubbed the per atom structure factor (PASF). The idea was to in effect calculate a FT for each atom, using only its neighbouring atoms within some cut-off range. The 3D FTs shown in figure 5.3 were calculated using a grid of $240 \times 240 \times 120$ k-points in reciprocal

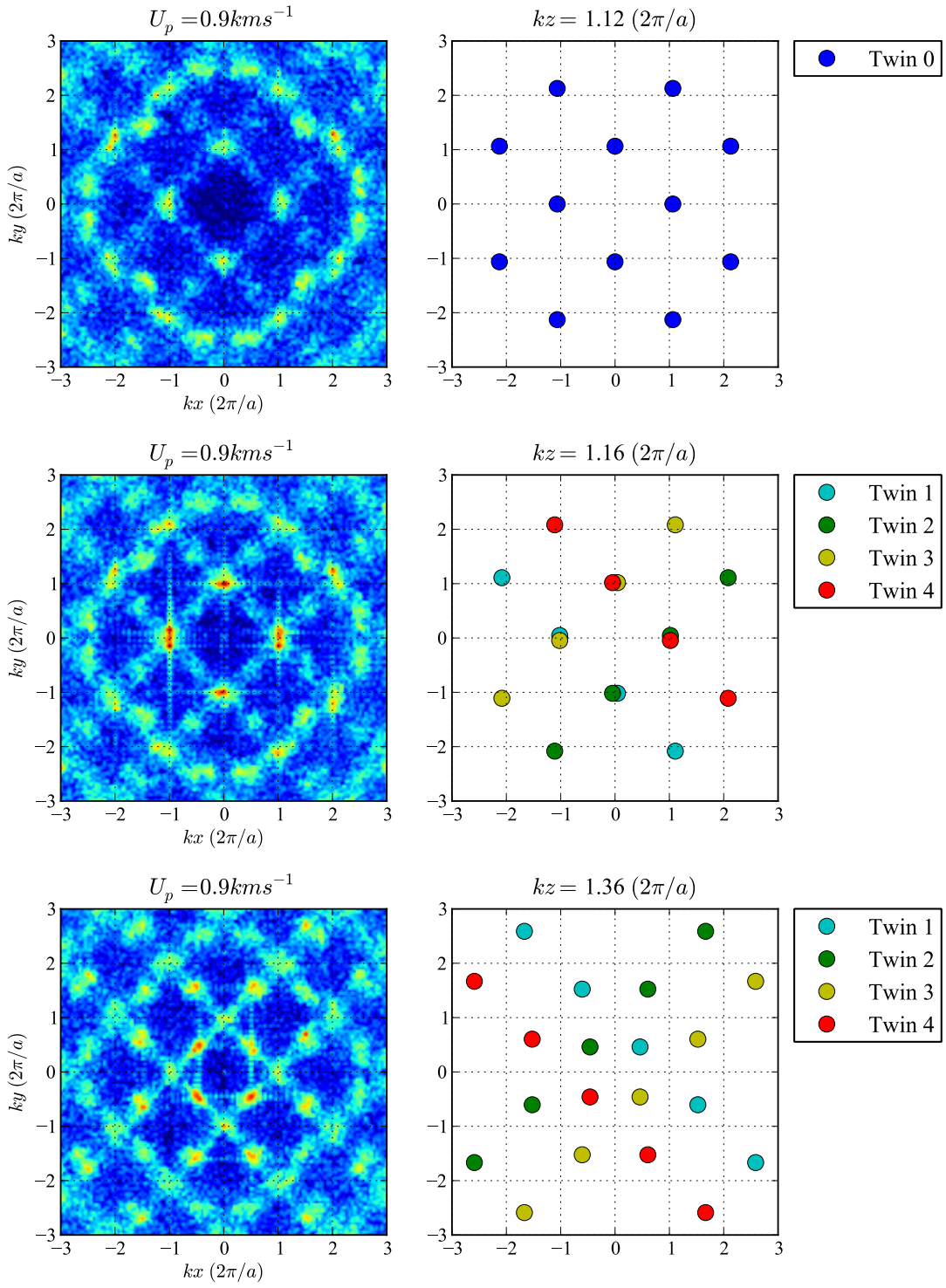


Figure 5.3: Fourier transforms of twinned region. Each plot pair corresponds to a slice in reciprocal space. The left plot is the FT from the twinned region in the MD, and the right plot is the analytical peak positions, which are colour coded according to twin orientation. 'Twin 0' is the original orientation.

space. It would of course be possible to calculate the FT for an extended region of reciprocal space for each atom using its neighbours. This would represent the full local structure of the atom. Increasing the cut-off range would increase the resolution in k-space, as the peak width is inversely proportional to sample size. It would also reduce the resolution in real space, since the local structure of each atom would be dependent on a larger region of atoms in real space. Instead, we choose only five k-points to calculate for each atom and use a short cut-off range of 4 Å, which balances the real space and reciprocal space resolutions. Increasing the number of sample points in reciprocal space may have some advantages or be necessary for applying the PASF to other problems in the future, but five points (for the four twin variants and default orientation) were adequate for this case and kept computational cost down.

Initiallly, the five k-points were chosen based on estimated peak positions like those in figure 5.3. The peak positions were estimated based on the assumption of hydrostatic compression without knowledge of the strains in the individual twins. Peak were selected for each twin where there is minimal overlap with peaks from other twins and the default orientation. For example, the peaks shown in figure 5.3, for the $kz = 1.36$ plot, at $kx = \pm 1.6$ and $ky = \pm 0.7$ are contributed from individual twins, unlike the peaks at $kz = 1.16$, $kx = \pm 1$ or $ky = \pm 1$ where the twin peaks overlap and are also close to the default orientation peaks in $kz = 1.12$.

Using the selected k-points, the structure factor for each point is calculated using

$$S\left(\mathbf{k}\right) = \sum_{n} e^{i\mathbf{k}.\mathbf{r_n}} \tag{5.4}$$

where n are the neighbour atoms within the cut-off. The square is then taken, effectively calculating the intensity at each of the k-points, and these values are

then compared. If the intensity at one k-point is significantly higher than the others the atom it is identified as belonging to the corresponding twin. We defined significant as being a factor of five higher than the other k-points, however the technique still appears to work with less stringent conditions (a factor of two was tested). For the majority of atoms this is indeed the case, and atoms with two or more equally-strong k-points were assigned a value representing undefined, which is coloured purple in the figures which follow. These atoms typically lie on the boundaries between twins, where atoms of both twin orientations are sampled within the cut-off radius.

The result can be refined by improving the k-points and iterating. If the full 3D FT is calculated for each set of atoms, separated according to twin type identified by the PASF, a more accurate position for each PASF k-point can be calculated. Using the refined k-points the PASF is performed again. The FTs produced by sampling the identified twins are, as expected, equivalent to the original reciprocal lattice rotated into the twin orientation. Although there are residual strains, which are discussed in the next section, the reciprocal lattice is still that of a cubic structure and there is no evidence of the ω phase observed in some recovered samples [116]. Nor is there any evidence of face-centred tetragonal material reported in previous studies using the Dai EFS Nb potential [120].

This technique seems to be quite powerful and may be useful in the analysis of other systems. The main disadvantage is that it requires *a priori* knowledge of what may be happening. The k-points also have to be tailored for each individual piston velocity since the compression is different. However, once suitable k-points are selected, modifying for different piston velocities is quite simple.

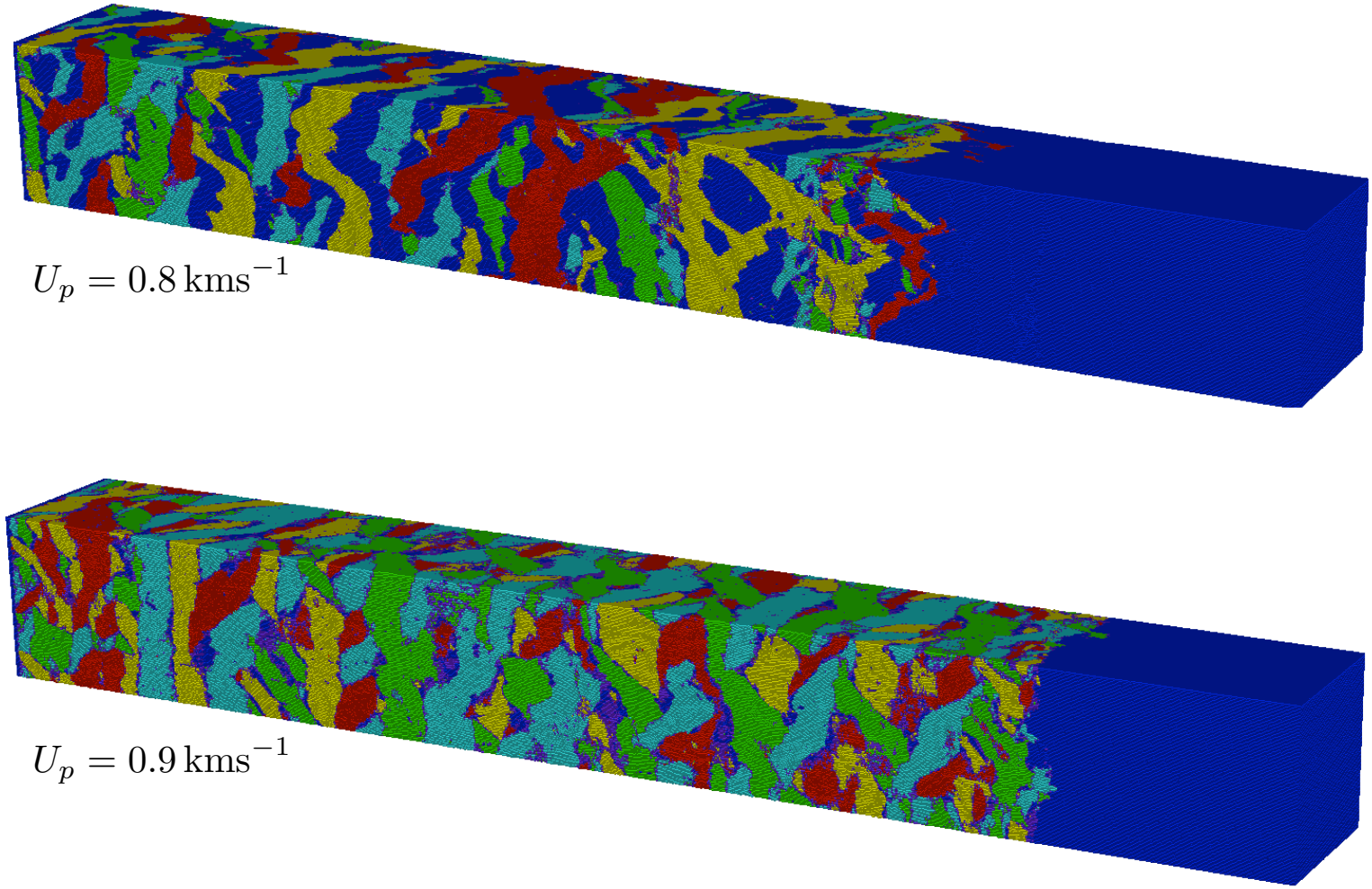


Figure 5.4: Atoms coloured by PASF method. Blue represents the untwinned orientation, without differentiating between uncompressed and compressed. Red, green, cyan, and yellow represent the four twin {112} variants. Small amounts of purple represent atoms which have not been identified as a unique twin.

5.3 Results

Figure 5.4 shows the two simulations, with piston velocities of $U_p = 0.8\,\mathrm{kms}^{-1}$ and $U_p = 0.9\,\mathrm{kms}^{-1}$, coloured according to the PASF. The upper image, at $U_p = 0.8\,\mathrm{kms}^{-1}$ represents the velocity at which the HEL is only just exceeded and there are large regions which remain in the original orientation, coloured blue. At $U_p = 0.9\,\mathrm{kms}^{-1}$, the sample is almost completely twinned, with slightly more undefined material at the twin boundaries. The PASF identifies the twinned regions remarkably cleanly.

We know that globally, the shear stress is reduced to close to zero in the twinned region, as shown in the wave profiles. The PASF allows us to separate the individual twins and investigate their contributions to the global stress state. An initial hypothesis might be that during the act of twinning the resulting twin grains relax towards hydrostatic compression, reducing the shear stress both locally and globally. Another suggestion was that the shear stress might be reduced globally but not locally in individual twin grains. The idea being that the uniaxially compressed, tetragonal unit cell, is largely retained and rotated into the four twin orientations. In the rotated co-ordinates of the twin, the grain still supports a significant shear stress, but the combined effect of the four twin variants reduces the global shear stress to zero.

The strains in the individual twin variants were calculated using the separated FTs and are shown in table 5.1. The strains are given in the rotated co-ordinates of the twin, for example ϵ_{zz} is calculated by finding magnitude the rotated (002) peak in the FT of the twin i.e. the short axis of the tetragonal unit cell. The strain anisotropy $(\epsilon_{zz} - \frac{1}{2}(\epsilon_{xx} + \epsilon_{yy}))$ in the twins has reduced considerably from the initial elastic compression close to 18%. However, the anisotropy is still

Table 5.1: The stresses and strains of the host lattice and twin variants after twinning has relaxed the shear stress.

U_p	Material	P_{xx} (kbar)	P_{zz} (kbar)	$P_{zz} - P_{xx}$	ϵ_{xx}	ϵ_{zz}
$0.8\,\mathrm{kms}^{-1}$	Host	566	580	14	-0.046	-0.119
	Twin 1	566	572	6	-0.043	-0.107
	Twin 2	566	569	3	-0.055	-0.093
	Twin 3	570	577	7	-0.047	-0.107
	Twin 4	570	577	7	-0.058	-0.085
	Twin mean	568	574	6	-0.057	-0.104
	Total	571	585	14	-	-
$0.9\,\mathrm{kms}^{-1}$	Host	642	678	36	-0.050	-0.13
	Twin 1	642	647	5	-0.051	-0.117
	Twin 2	641	645	4	-0.049	-0.121
	Twin 3	649	650	1	-0.057	-0.114
	Twin 4	648	650	2	-0.057	-0.114
	Twin mean	646	648	2	-0.056	-0.13
	Total	639	663	24	-	-

significant and the shear stress in the twin is 6 kbar for $U_p = 0.8\,\mathrm{kms}^{-1}$. It should be noted that the stresses in table 5.1 given for the twins are in the rotated twin co-ordinates.

For $U_p = 0.9\,\mathrm{kms}^{-1}$ almost 95% of the sample twins. The strains in the twins and the small amount of untwinned are almost equal, with shear stress in the twin on average reduced to 2kbar. The resulting picture is that when the material twins, the initial uniaxial compression is rotated into the twin orientation but with some relaxation towards cubic compression. The shear stresses are reduced both globally and locally, with higher shear stresses in the remaining untwinned material.

5.3.1 Mechanism

The mechanism employed in deformation twinning has long been a topic of debate [28]. The standard idea of twinning by shear, increasing displacement of progressive planes from the slip plane, was discussed in the background theory. Such large displacements seem unlikely in these timescales, and the actual path that the atoms take is not something that has been discussed for shock compression.

In an effort to determine the mechanism we employed two methods. In the first attempt we used a 3D pair correlation function, $g(\mathbf{r}) = \sum_i \sum_n \delta(\mathbf{r_n} - \mathbf{r_i} - \mathbf{r})$ where the sum in i is over all atoms in the sample, and n the neighbours of atom i falling within a cut-off radius. The function $g(\mathbf{r})$ is calculated by taking each atom in the sample, calculating the vectors to all neighbouring atoms within the cut-off (in this case we again used 4 Å). The vectors are binned into a 3D grid, effectively forming an 'average' unit cell. As the sampled region twins the peaks split and move to the twin positions. In the intermediate phase the atoms that are moving show up in the regions between the initial and final positions.

Figure 5.5 shows the 3D pair correlation function for one twin variant over several timesteps, in the elastically compressed stage, during twinning, and finally in the twinned state. A threshold is applied so that only bins with more than a particular value are visible (the thresholding value depends on the sample size). The points are coloured by distance along [110], out of the page such that red points are a plane above the page (and blue, where visible, is a plane below the page). The atoms are selected as those in the twin with twin plane $(\bar{1}12)$ at 140ps, and the $(\bar{1}12)$ plane is indicated in the elastically compressed snapshot. In the intermediate phase it is clear that the atoms on alternating $(\bar{1}12)$ planes are taking curved paths broadly in the $[1\bar{1}1]/[\bar{1}1\bar{1}]$ directions. The points on the other planes, indicated by the three lines on the intermediate figure, are largely

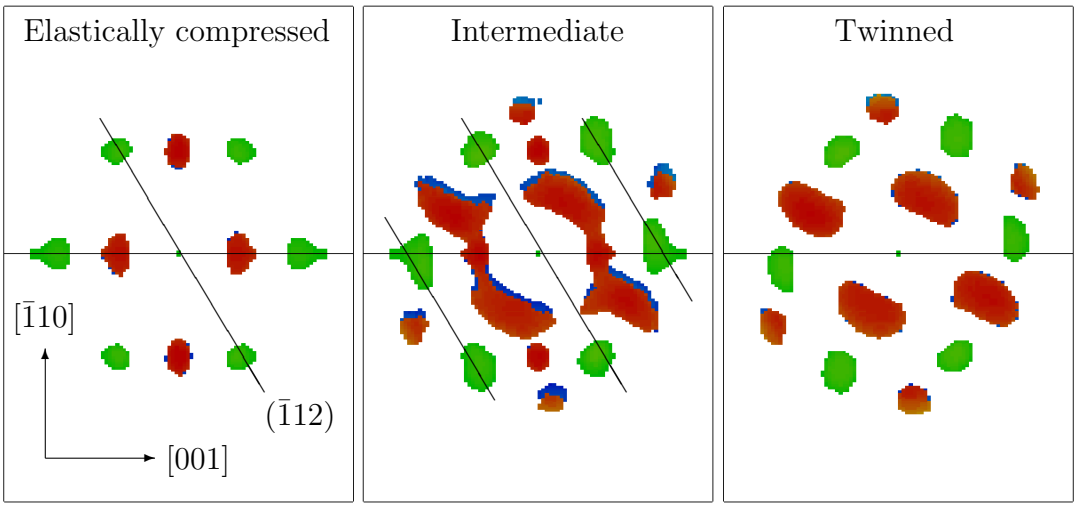


Figure 5.5: 3D pair correlation function for atoms evolving from the initially elastically compressed state to one of the twin orientations. The sample is from the $U_p = 0.9\,\mathrm{kms}^{-1}$ simulation with atoms selected from one of the twins at 140 ps. The 3D pair correlation function is thresholded by intensity and coloured by distance in the [110] direction.

unmoved with a slight rotation. This is telling us that if we take a single atom's position as the origin, the adjacent ($\bar{1}$12) planes are displaced relative to this atom, but the next ($\bar{1}$12) planes do not appear to be displaced.

This suggests that the standard shearing of successive planes does not occur. The 3D pair correlation function for an idealised shearing of successive planes is shown in figure 5.6. The main thing to note is that the outer ($\bar{1}$12) planes are displaced unlike in figure 5.5. Additionally, in the shearing mechanism, at no point will there be displacements in the positions indicated by the + symbol, which is evident in the previous figure. This is simply due to the fact that in the shearing mechanism, the atoms are all displaced in the same direction, suggesting that this may not be the case. The 3D pair correlation function for a 'shuffle' mechanism is also shown in figure 5.6. The atoms on every third ($\bar{1}$12) plane

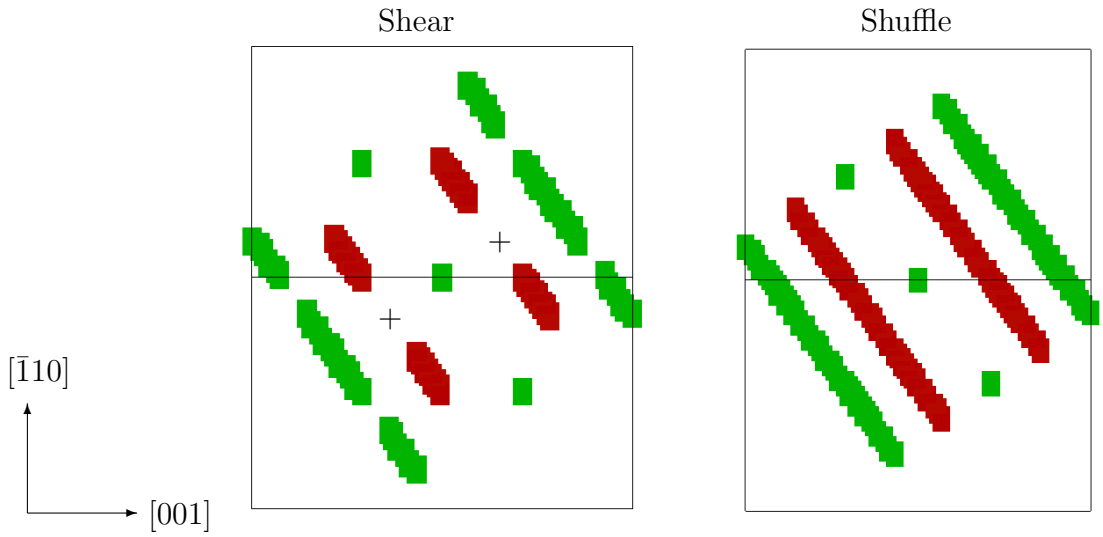


Figure 5.6: 3D pair correlation function for idealised shear and shuffle mechanism.

do not move, and the atoms on adjacent ($\bar{1}12$) planes are displaced in opposite directions by $\frac{a}{6}[111]$. The problem here is that the outer ($\bar{1}12$) planes are still displaced.

This problem is resolved if one considers effect of the initial uniaxial strain. Figure 5.7 illustrates the displacements involved at three uniaxial strains. Red and blue circles represent atoms in two adjacent ($1\bar{1}0$) planes. The top figure shows the normal case with no uniaxial strain, where both the adjacent and successive ($\bar{1}12$) planes must be displaced to the twin positions. The bottom figure shows the case for 18.4% uniaxial strain, where alternating ($\bar{1}12$) planes are already at the twin positions and only one in two planes are displaced from the twin positions. A mechanism where one set of planes shifts and the other is stationary fits the 3D pair correlation function in figure 5.5, seen in these MD simulations.

What makes this argument compelling is that the measured compression for the simulation with piston velocity $U_p = 0.9\,\mathrm{kms}^{-1}$, in the elastically compressed

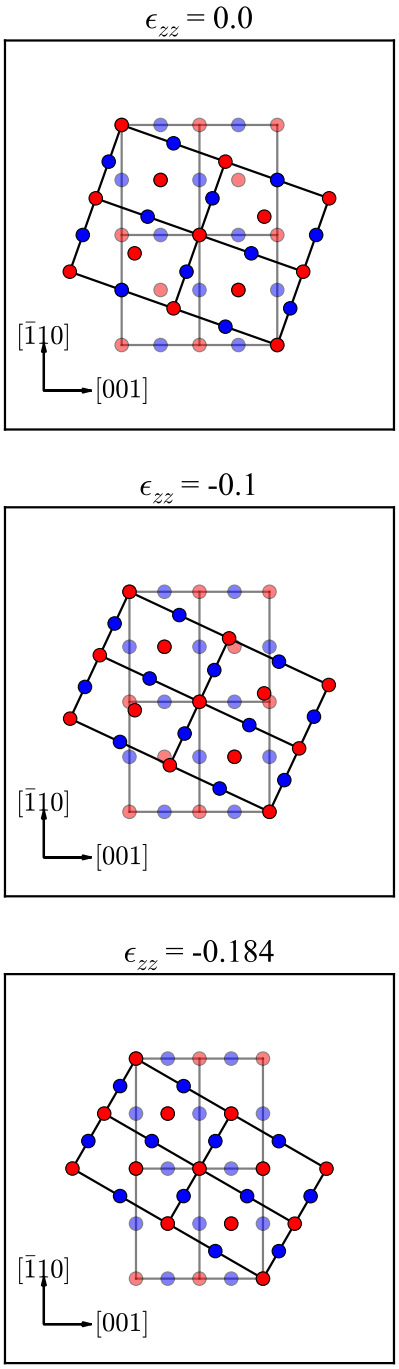


Figure 5.7: Effect of initial uniaxial strain on twinning atomic displacements.

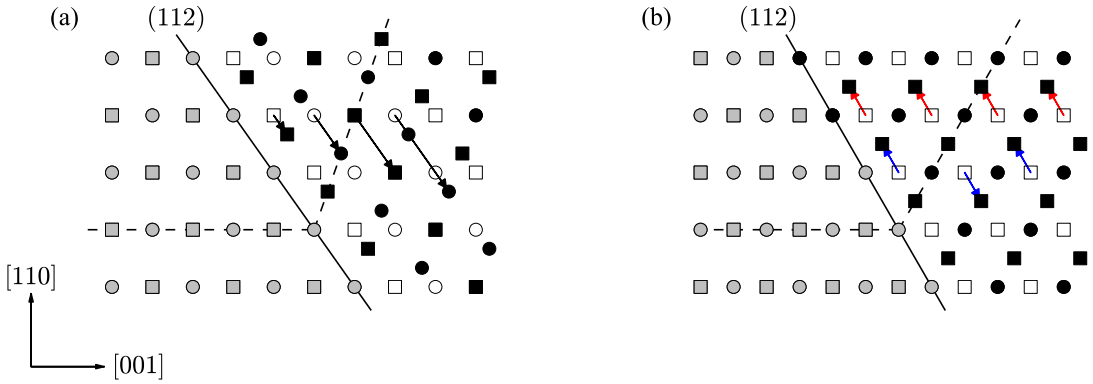


Figure 5.8: (a) The standard picture of twin formation on the $\langle 111 \rangle \{112\}$ system in a bcc metal. (b) The proposed shuffle mechanism for shock compression with this potential, with an inital compression of 18.4%. Squares and circles represent two neighbouring $(1\bar{1}0)$ planes. Grey sites denote the host lattice, with white and black sites indicating the initial and final positions of the twinned atoms. Twin boundaries are indicated by solid lines with a dashed line highlighting the twin. The red and blue arrows in (b) indicate two potential shuffle mechanisms.

region $350 < z < 540$nm (see figure 5.2), is 18%. At this compression the atoms on alternating (112) planes are almost coincident with the equivalent positions in the twin (at $\epsilon_{zz} = \sqrt{2/3} - 1$ these positions are exactly coincident ignoring thermal vibrations).

The direction in which each alternate (112) plane shifts is not obvious and two potential candidates are shown in figure 5.8 (b) by the red and blue arrows. The red arrows show a case where each alternating plane moves in the same direction. The blue arrows indicate alternating planes moving in opposite directions. In order to confirm the direction of shuffling on the alternate planes, we employed a second analysis method, looking at the relative displacements of the atoms. This is visualised and shown in figure 5.9. For each atom, its position with respect to its neighbour in the $[0\bar{1}0]$ direction was compared for two different timesteps, producing a relative displacement. This method was chosen as there is no obvious frame of reference to use in the shock simulation to subtract the large change in

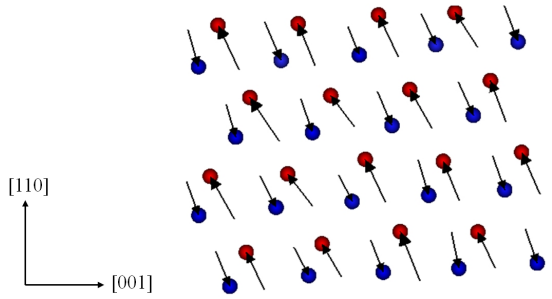


Figure 5.9: Relative displacements for a small region of one twin variant. The arrows indicate the change in position for each atom with respect to the original nearest neighbour in the $[0\bar{1}0]$ direction, from 80 ps to 120 ps. Red and blue spheres represent atoms in two neighbouring $(1\bar{1}0)$ planes.

position in the shock direction. The displacement vectors are plotted with heads lying at the atom positions in the latter timestep. The timesteps were chosen such that the region is elastically compressed in the first timestep, and twinned in the second timestep. The result shows that each (112) plane is displaced in the opposing direction to the two neigbouring (112) planes. This is compatible with the mechanism indicated by the red arrows in figure 5.8, and is surprisingly similar to the mechanism of the $\alpha - \epsilon$ phase transition in Fe [9].

5.4 Omega diffraction experiments

These white-light Laue experiments, built on the technique developed at Janus, employed an implosion capsule x-ray source (with energies up to 25 keV, 150 ps pulse) and a transmission geometry set-up. The Ta crystals were mounted directly in front of a pinhole on an image plate containing box. The Ta single-crystals were loaded in the [001] direction and peak pressures were measured using the impedance-matching method and VISAR velocity profiles.

No evidence of twinning was observed in the Ta Laue experiments at Omega.

The observed diffraction peaks under shock compression suggest a state of uniaxial compression. The peaks are shifted towards the basal plane spot, in the same manner as the elastically compressed silicon discussed in the earlier chapter. Using the measured peak stress and elastic constants determined from density functional theory, the positions for purely elastic compression were calculated, and were not found to match the peaks from the shocked material. Therefore, the measured shear strain was significantly reduced from that expected for elastic compression. This work, analysed by Andrew Comley, is published in Physical Review Letters [114].

As shown earlier, the twinning mechanism in the MD simulation relies on a large initial elastic compression, such that the atoms on alternating planes are coincident with the twin positions. If the shear strain were relieved, by pre-existing dislocations for example, twinning via this mechanism would be inhibited. Perhaps this is why twinning is not observed in the diffraction data.

5.5 Conclusions

Molecular dynamics simulations of shock compression of Ta with piston velocities of $U_p = 0.8\,\mathrm{kms}^{-1}$ and $0.9\,\mathrm{kms}^{-1}$, employing the EFS potential, show significant deformation twinning. A novel order parameter, the PASF, was developed and shown to be highly successful at identifying the four twin variants. Using the separated atoms to measure the strains in the individual twin variants, and thus analytically calculate the twin peak positions, the peaks in the 3D FT of the plastically deformed region are all accounted for by twinning, with no evidence of ω phase or face-centred-tetragonal material seen in other simulations using EFS. The stress states in the twins appear to show that even though the strains in the

twins are anisotropic, the shear stresses are largely relieved locally leading to the global relief of shear stresses. The twinning mechanism is conclusively identified as the displacement of alternating planes in the same direction in a manner which bears some resemblance to the $\alpha - \epsilon$ phase transition in Fe.

Chapter 6

Summary and Future work

6.1 Summary

The work in chapter 3 describes the design and development of a nanosecond timescale, white-light Laue x-ray diffraction technique. The novel mixed-metal backlighter designed for this technique is described and x-ray spectra presented, showing that it produces a highly-textured broad-band source of x-rays with energies from 3 to 8keV. The potential of the technique is tested on shocked single-crystal silicon, driven below the elastic limit, showing uniaxial compressions consistent with the deduced peak pressure.

The white-light Laue technique is then applied to the shock compression of single-crystal copper, loaded along the [001] crystallographic axis. The observed diffraction patterns are not consistent with spot streaking due to stacking faults, as predicted in large-scale MD simulations. Nor are they consistent with twinning observed in some recovered target experiments. The observed subsidiary peaks are in the [100] and [010] directions and suggest small-angle rotations of the crystal about the [010] and [100] axes. The magnitude of the rotation angle is observed to increase with shock pressure, suggesting an increase in dislocation generation and subsequent slip. The observed rotation axes are accounted for

by a conjugate or double slip model, where the combined slip of the two systems results in the correct crystal rotation orientation. The inferred dislocation density for the measured rotation angles is of order $10^{12}\,\mathrm{cm}^{-2}$, consistent with the defect densities predicted by Orowan's equation (2.36). These measurements provide the first direct evidence of stress dependent lattice rotations in a shocked single-crystal on nanosecond timescales.

Chapter 5 presents MD simulations of shock compression in single-crystal Ta, using an EFS inter-atomic potential. At piston velocities greater than $U_p = 0.8\,\mathrm{kms}^{-1}$, the crystal undergoes plastic deformation, relieving the shear stress towards zero. The deformation mechanism is identified using Fourier transform analysis and a new order parameter technique, the per atom structure factor, is developed. The PASF is demonstrated to be highly successful at identifying the four twin variants in the shocked Ta. The individual twin stresses are extracted, and show that in the act of twinning, the shear stress is largely relieved at the local level of each grain despite considerable strain anisotropies. The twinning mechanism is identified using a 3d pair correlation function, and tracking of the relative atomic displacements, showing a mechanism which is not the standard shear of twin planes. The mechanism is shown to occur at large uniaxial compressions, where the atoms on alternating (112) planes are almost coincident with the equivalent twin positions. The other (112) planes are displaced, in the same direction, to the twin positions. This mechanism has not been observed or discussed previously in relation to deformation twinning in shock compression.

6.2 Future work

The white-light Laue technique developed at JANUS has already been applied by other researchers in work which is yet to be published. The same technique, or at least an improved version, is being considered as an x-ray diffraction diagnostic at the National Ignition Facility. Development has also continued at the newly commissioned Orion laser at AWE. Development shots with new backlighter cocktails using different elements have already taken place during commissioning shots at Orion. This work is ongoing, with aim being to continue Laue diffraction experiments on shocked Ta, which were started at Omega. The Omega shots used a transmission geometry set-up, and the Orion diagnostic is being designed for back-reflection geometry, with a number of advantages.

Something I was continually reminded of whilst writing this thesis, is that the both the copper diffraction data, and the tantalum twinning simulations, are both restricted to shocks along the [001] axis. This is really a special case, and both MD simulations and TXRD experiments have demonstrated the change in behaviour for different shock directions. A handful of shots in the [110] and [111] directions were taken for copper at JANUS. However, under the limited time conditions of the experiments, the effort was focused on [001] where the interesting diffuse peaks had already been observed. The other crystal directions are clearly a large avenue for future investigation, as well of course are other elements!

Both the experimental and MD simulation work presented here are also devoted to single-crystals, at least in the initial state. Most real materials are of course not single-crystalline. The PASF might be applied to individual grains in polycrystalline simulations. Is the the same twinning mechanism observed or do defects generated at the grain boundaries relieve the shear stress before twinning

can occur? Other potentials need to be explored too.

The white-light Laue technique is inherently limited to single-crystals. However, the mixed-metal backlighter may be applicable to another technique. Using CCD cameras in a single photon mode, the energies and positions of the single hit events can be used to map out reciprocal space. The development of this technique, using the same backlighter foil developed for white-light Laue, is already underway.

Appendix A

A.1 Lattice rotation under large strains

The following theory is from Kelly [27] and then Bowen & Christian [109] and based upon the geometry in figure A.1. The theory for tension is given in addition to the compression as it is more intuitive and makes the compression case more understandable. The loading axis is initially vertical through 0 and the system is constrained such that after glide the point A' is forced to still be along this axis.

A.1.1 Single glide

For single glide in tension, denoting the vector OA as $\mathbf{r}$ and the vector OA' as $\mathbf{r}'$ it follows that for a glide of γ:

$$\mathbf{r}' = \mathbf{r} + \gamma(\mathbf{r} \cdot \mathbf{n})\boldsymbol{\beta} \tag{1}$$

where $\mathbf{n}$ is the unit vector normal to the slip plane and $\boldsymbol{\beta}$ is the slip direction.

$$\frac{l}{l_0} = (1 + e) = \frac{|\mathbf{r}'|}{|\mathbf{r}|} \tag{2}$$

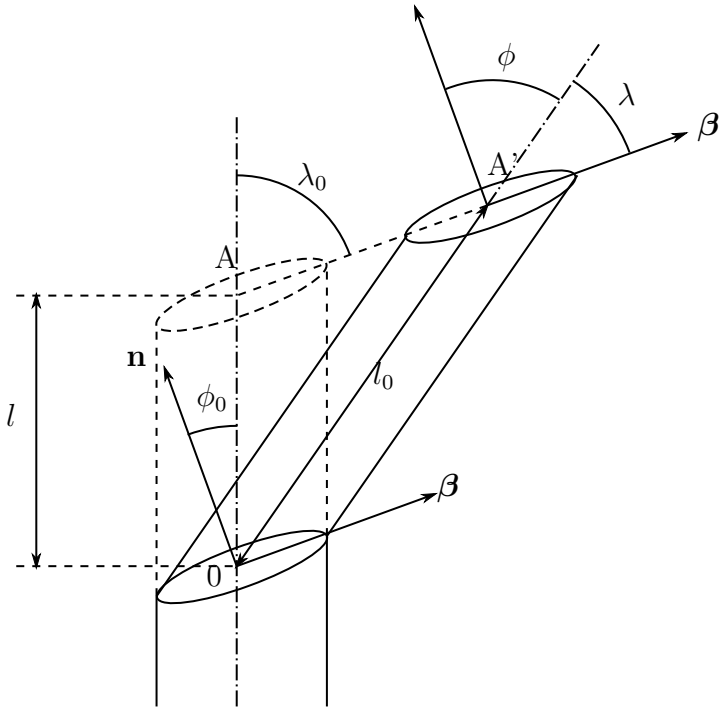


Figure 1: Geometry and parameters for lattice rotation during glide.

The angle ϕ_0 between the final slip plane normal and the loading axis is given by:

$$\cos\phi = \frac{1}{|\mathbf{r}'|}(\mathbf{r}' \cdot \mathbf{n}) \tag{3}$$

$$= \frac{1}{|\mathbf{r}'|}[\mathbf{r} \cdot \mathbf{n} + \gamma(\mathbf{r} \cdot \mathbf{n})(\boldsymbol{\beta} \cdot \mathbf{n})] \tag{4}$$

$$= \frac{1}{|\mathbf{r}'|}(\mathbf{r} \cdot \mathbf{n}) \quad \text{since } \boldsymbol{\beta} \cdot \mathbf{n} = 0 \tag{5}$$

$$= \frac{l_0 \cos\phi_0}{l} \tag{6}$$

and therefore:

$$\frac{l}{l_0} = \frac{\cos\phi_0}{\cos\phi} \tag{7}$$

Similarly, taking the cross product of both sides in equation 1 with $\boldsymbol{\beta}$:

$$|\mathbf{r}' \times \boldsymbol{\beta}| = |\mathbf{r}'| \sin\lambda \tag{8}$$

$$= |[\mathbf{r} + \gamma(\mathbf{r} \cdot \mathbf{n})\boldsymbol{\beta}] \times \boldsymbol{\beta}| \tag{9}$$

$$= |\mathbf{r} \times \boldsymbol{\beta}| \quad \text{since } \boldsymbol{\beta} \times \boldsymbol{\beta} = 0 \tag{10}$$

and therefore:

$$\frac{l}{l_0} = \frac{\sin\lambda_0}{\sin\lambda} \tag{11}$$

Taking the dot product of equation 1 with $\boldsymbol{\beta}$:

$$\mathbf{r}' \cdot \boldsymbol{\beta} = \mathbf{r} \cdot \boldsymbol{\beta} + \gamma(\mathbf{r} \cdot \mathbf{n})\boldsymbol{\beta} \cdot \boldsymbol{\beta} \tag{12}$$

$$l\cos\lambda = l_0\cos\lambda_0 + \gamma l_0 \cos\phi_0 \tag{13}$$

and therefore:

$$\gamma = \frac{\cos\lambda}{\cos\phi} - \frac{\cos\lambda_0}{\cos\phi_0} \tag{14}$$

Single glide in compression

The approach is similar for single glide in compression. Taking $\mathbf{r_1}$ and $\mathbf{r_2}$ as two non-parallel unit vectors in the plane with normal $\mathbf{m}$. After glide, the new values

of $\mathbf{r'_1}$ and $\mathbf{r'_2}$ define the new plane $\mathbf{m'}$ by

$$\begin{aligned}
\mathbf{m'} &= \mathbf{r'_1} \times \mathbf{r'_2} && (15)\\
&= [\mathbf{r_1} + \gamma(\mathbf{r_1} \cdot \mathbf{n})\boldsymbol{\beta}] \times [\mathbf{r_2} + \gamma(\mathbf{r_2} \cdot \mathbf{n})\boldsymbol{\beta}] && (16)\\
&= [\mathbf{r_1} \times \mathbf{r_2}] + \gamma(\mathbf{r_1} \cdot \mathbf{n})\boldsymbol{\beta} \times \mathbf{r_2} - \gamma(\mathbf{r_2} \cdot \mathbf{n})\boldsymbol{\beta} \times \mathbf{r_1} && (17)\\
&= \mathbf{m} + \gamma\boldsymbol{\beta} \times [(\mathbf{r_1} \cdot \mathbf{n})\mathbf{r_2} - (\mathbf{r_2} \cdot \mathbf{n})\mathbf{r_1}] && (18)\\
&= \mathbf{m} + \gamma\boldsymbol{\beta} \times \mathbf{n} \times [\mathbf{r_2} \times \mathbf{r_1}] && (19)\\
&= \mathbf{m} - \gamma\boldsymbol{\beta} \times [\mathbf{n} \times \mathbf{m}] && (20)\\
&= \mathbf{m} - \gamma[(\boldsymbol{\beta} \cdot \mathbf{m})\mathbf{n} - (\boldsymbol{\beta} \cdot \mathbf{n})\mathbf{m}] && (21)
\end{aligned}$$

and since $\boldsymbol{\beta} \cdot \mathbf{n} = 0$ we arrive at:

$$\mathbf{m'} = \mathbf{m} - \gamma(\boldsymbol{\beta} \cdot \mathbf{m})\mathbf{n} \tag{22}$$

Taking the dot product of both sides with $\boldsymbol{\beta}$ gives:

$$\mathbf{m'} \cdot \boldsymbol{\beta} = \mathbf{m} \cdot \boldsymbol{\beta} \tag{23}$$

and therefore:

$$\frac{l_0}{l} = \frac{\cos\lambda_0}{\cos\lambda} \tag{24}$$

where λ and λ_0 are again the angles between the compression axis and the slip direction. Taking the cross product of 22 with $\mathbf{n}$ similarly gives:

$$\frac{l_0}{l} = \frac{\sin\phi_0}{\sin\phi} \tag{25}$$

where ϕ and ϕ_0 are the angles between the compression direction and the slip plane normal. Taking the dot product of each side of 22 with $\mathbf{n}$ gives:

$$\mathbf{m}' \cdot \mathbf{n} = \mathbf{m} \cdot \mathbf{n} + \gamma(\boldsymbol{\beta} \cdot \mathbf{m}) \tag{26}$$

$$\gamma = \frac{\cos\phi}{\cos\lambda} - \frac{\cos\phi_0}{\cos\lambda_0} \tag{27}$$

A.1.2 Double glide

Assume the stress axis is such that two slip systems $\mathbf{n_1}$, $\boldsymbol{\beta}_1$ and $\mathbf{n_2}$, $\boldsymbol{\beta}_2$ are equally stressed then:

$$\mathbf{r}' \cdot \mathbf{n_1} = \mathbf{r}' \cdot \mathbf{n_2} = l\cos\theta \quad \text{and} \quad \mathbf{r}' \cdot \boldsymbol{\beta}_1 = \mathbf{r}' \cdot \boldsymbol{\beta}_2 = l\cos\lambda \tag{28}$$

For incremental shears on $\mathbf{n_1}$, $\boldsymbol{\beta}_1$, using equation 1:

$$d\mathbf{r}' = l\cos\theta d\gamma_1 \boldsymbol{\beta}_1 \tag{29}$$

Then for both systems:

$$d\mathbf{r}' = l\cos\theta(d\gamma_1\boldsymbol{\beta}_1 + d\gamma_2\boldsymbol{\beta}_2) \tag{30}$$

For equal slip on both systems:

$$d\gamma_1 = d\gamma_2 = d\gamma \tag{31}$$

leading to:

$$d\mathbf{r}' = l\cos\theta d\gamma(\boldsymbol{\beta}_1 + \boldsymbol{\beta}_2) \tag{32}$$

From equation 28 we have:

$$d(l\cos\theta) = \mathbf{n_1}\cdot d\mathbf{r}' = \mathbf{n_1}\cdot\boldsymbol{\beta}_1 l\cos\theta d\gamma_1 \tag{33}$$

$$d\gamma_1 = \frac{d(l\cos\theta)}{\mathbf{n_1}\cdot\boldsymbol{\beta}_1 l\cos\theta} \tag{34}$$

$$\gamma_1 = \frac{1}{\mathbf{n_1}\cdot\boldsymbol{\beta}_1}\ln\left(\frac{l\cos\theta}{l_0\cos\theta_0}\right) \tag{35}$$

The total shear strain is then:

$$\gamma = \frac{2}{\mathbf{n_1}\cdot\boldsymbol{\beta}_1}\ln\left(\frac{l\cos\theta}{l_0\cos\theta_0}\right) \tag{36}$$

Although it is the lattice that rotates the effect is that the loading axis rotates towards the direction $\boldsymbol{\beta} = \boldsymbol{\beta}_1 + \boldsymbol{\beta}_2$, and we introduce the angle between them as α. Hence:

$$\mathbf{r}'\cdot(\boldsymbol{\beta}_1+\boldsymbol{\beta}_2) = l|\boldsymbol{\beta}|\cos\alpha = 2l\cos\lambda \tag{37}$$

and similarly for α_0 so that:

$$\frac{\cos\alpha}{\cos\alpha_0} = \frac{\cos\lambda}{\cos\lambda_0} \tag{38}$$

From equation 32 and 33 it follows that:

$$|\boldsymbol{\beta}|d(l\cos\alpha) = (\boldsymbol{\beta}_1+\boldsymbol{\beta}_2)\cdot d\mathbf{r}' \tag{39}$$

$$= (\boldsymbol{\beta}_1+\boldsymbol{\beta}_2)\cdot[l\cos\theta d\gamma(\boldsymbol{\beta}_1+\boldsymbol{\beta}_2)] \tag{40}$$

$$= |\boldsymbol{\beta}|^2 l\cos\theta d\gamma \tag{41}$$

$$= \frac{|\boldsymbol{\beta}|^2}{\mathbf{n_1}\cdot\boldsymbol{\beta}_1} d(l\cos\theta) \tag{42}$$

then integrating gives:

$$l\cos\alpha - l_0\cos\alpha_0 = \frac{|\boldsymbol{\beta}|}{\mathbf{n_1}\cdot\boldsymbol{\beta}_1}(l\cos\theta - l_0\cos\theta_0) \tag{43}$$

$$\cos\theta = \frac{l_0}{l}\cos\theta_0 + \frac{\mathbf{n_1}\cdot\boldsymbol{\beta}_1}{l|\boldsymbol{\beta}|}(l\cos\alpha - l_0\cos\alpha_0) \tag{44}$$

$$\frac{\cos\theta}{\cos\theta_0} = \frac{l_0}{l} + \frac{\mathbf{n_1}\cdot\boldsymbol{\beta}_1}{|\boldsymbol{\beta}|}\left(\frac{\cos\alpha}{\cos\theta_0} - \frac{l_0}{l}\frac{\cos\alpha_0}{\cos\theta_0}\right) \tag{45}$$

The change in length is:

$$ldl = \mathbf{r}'\cdot d\mathbf{r}' = \frac{l|\boldsymbol{\beta}|}{\mathbf{n_1}\cdot\boldsymbol{\beta}_1}\cos\alpha d(l\cos\theta) \tag{46}$$

Integrating using equation 39 gives:

$$l^2 - l_0^2 = l^2\cos^2\alpha - l_0^2\cos^2\alpha_0 \tag{47}$$

Rearranging gives:

$$\frac{l_0}{l} = \frac{\sin\alpha}{\sin\alpha_0} \tag{48}$$

Substituting into 36 leads us to:

$$\gamma = \frac{2}{\mathbf{n_1}\cdot\boldsymbol{\beta}_1}\ln\left(1 + \frac{\mathbf{n_1}\cdot\boldsymbol{\beta}_1}{|\boldsymbol{\beta}|}\frac{\sin\alpha_0}{\cos\theta_0}(\cot\alpha - \cot\alpha_0)\right) \tag{49}$$

Double glide in compression

Using 22, for incremental compression:

$$d\mathbf{m}' = \frac{\cos\lambda}{l} d\gamma(\mathbf{n_1} + \mathbf{n_2}) \tag{50}$$

so the stress axis rotates towards $\mathbf{n} = \mathbf{n_1} + \mathbf{n_2}$.

$$d\left(\frac{\cos\lambda}{l}\right) = \boldsymbol{\beta}_1 \cdot d\mathbf{m}' = \boldsymbol{\beta}_1 \cdot \mathbf{n_2} \left(\frac{\cos\lambda}{l}\right) d\gamma_1 \tag{51}$$

After integration:

$$\gamma_1 = \frac{1}{\boldsymbol{\beta}_1 \cdot \mathbf{n_2}} \ln\left(\frac{l_0 \cos\lambda}{l \cos\lambda_0}\right) \tag{52}$$

so the combined shear strain is:

$$\gamma = \frac{2}{\boldsymbol{\beta}_1 \cdot \mathbf{n_2}} \ln\left(\frac{l_0 \cos\lambda}{l \cos\lambda_0}\right) \tag{53}$$

We name the angle between $\mathbf{m}'$ and $\mathbf{n} = \mathbf{n_1} + \mathbf{n_2}$ as α. Then similarly as for the tension case:

$$l\mathbf{m}' \cdot (\mathbf{n_1} + \mathbf{n_2}) = |\mathbf{n}| \cos\alpha = 2\cos\theta \tag{54}$$

and

$$\frac{\cos\alpha}{\cos\alpha_0} = \frac{\cos\theta}{\cos\theta_0} \tag{55}$$

then:

$$|\mathbf{n}|d\left(\frac{\cos\alpha}{l}\right) = (\mathbf{n_1} + \mathbf{n_2}) \cdot d\mathbf{m}' \tag{56}$$

$$= \frac{\cos\lambda}{l} d\gamma_1 |\mathbf{n}|^2 \tag{57}$$

$$= \frac{|\mathbf{n}|^2}{\boldsymbol{\beta}_1 \cdot \mathbf{n_2}} d\left(\frac{\cos\lambda}{l}\right) \tag{58}$$

Integrating gives:

$$\frac{\cos\alpha}{l} - \frac{\cos\alpha_0}{l_0} = \frac{|\mathbf{n}|}{\boldsymbol{\beta}_1 \cdot \mathbf{n_2}} \left(\frac{\cos\lambda}{l} - \frac{\cos\lambda_0}{l_0}\right) \tag{59}$$

$$\frac{\cos\lambda}{\cos\lambda_0} = \frac{l}{l_0} + \frac{\boldsymbol{\beta}_1 \cdot \mathbf{n_2}}{|\mathbf{n}|} \left(\frac{\cos\alpha}{\cos\lambda_0} - \frac{l\cos\alpha_0}{l_0\cos\lambda_0}\right) \tag{60}$$

The change in length is given by:

$$-ldl = \mathbf{m}' \cdot d\mathbf{m}' = \frac{\cos\alpha}{l} d\left(\frac{\cos\alpha}{l}\right) \tag{61}$$

and integrating gives:

$$l^2 - l_0^2 = \frac{\cos^2\alpha_0}{l_0^2} - \frac{\cos^2\alpha}{l^2} \tag{62}$$

and rearranging:

$$\frac{l}{l_0} = \frac{\sin\alpha}{\sin\alpha_0} \tag{63}$$

Substituting into equation 53 we arrive at the result:

$$\gamma = \frac{2}{\boldsymbol{\beta}_1 \cdot \mathbf{n_2}} \ln\left(1 + \frac{\boldsymbol{\beta}_1 \cdot \mathbf{n_2}}{|\mathbf{n}|} \frac{\sin\alpha_0}{\cos\lambda_0} (\cot\alpha - \cot\alpha_0)\right) \tag{64}$$

References

[1] W. J Macquorn Rankine. On the thermodynamic theory of waves of finite longitudinal disturbance. *Philosophical Transactions of the Royal Society of London*, 160(1870):277–288, 1870. 1, 38

[2] P. H. Hugoniot. Mémoire sur la propagation des mouvements dans les corps et spécialement dans les gaz parfaits (premier partie). *Journal de L'Ecole Polytechnique*, 57:3–97, 1887. 1, 38

[3] Ya. B. Zel'dovich and Yu. P. Raizer. *Physics of Shock Waves and High-Temperature Hydrodynamic Phenomena*. Dover Publications, 2002. 1

[4] J. M. Walsh. Metal Equation of State from Shock-wave Studies. *Bull. Am. Phys. Soc.*, 29(28), 1954. 2

[5] Dennison Bancroft, Eric L. Peterson, and Stanley Minshall. Polymorphism of Iron at High Pressure. *Journal of Applied Physics*, 27(3):291, 1956. 2

[6] John C. Jamieson and A. W. Lawson. X-Ray Diffraction Studies in the 100 Kilobar Pressure Range. *Journal of Applied Physics*, 33(3):776, 1962. 2

[7] D. H. Kalantar, J. F. Belak, G. W. Collins, J. D. Colvin, H. M. Davies, J. H. Eggert, T. C. Germann, J. Hawreliak, B. L. Holian, K. Kadau, P. S. Lomdahl, H. E. Lorenzana, M. A. Meyers, K. Rosolankova, M. S. Schneider, J. Sheppard, J. S. Stölken, and J. S. Wark. Direct Observation of the α-ϵ Transition in Shock-Compressed Iron via Nanosecond X-Ray Diffraction. *Physical Review Letters*, 95(7):075502, 2005. 2, 3, 54, 60, 120

[8] D. H. Kalantar, G. W. Collins, J. D. Colvin, J. H. Eggert, J. Hawreliak, H. E. Lorenzana, M. A. Meyers, R. W. Minich, K. Rosolankova, M. S. Schneider, J. S. Stölken, and J. S. Wark. In situ diffraction measurements of lattice response due to shock loading, including direct observation of the α-ϵ phase transition in iron. *International Journal of Impact Engineering*, 33(1-12):343–352, 2006. 2, 3

[9] Kai Kadau, Timothy C. Germann, Peter S. Lomdahl, and Brad Lee Holian. Microscopic View of Structural Phase Transitions Induced by Shock Waves. *Science*, 296(2002):1682–1684, 2002. 2, 4, 120, 139

[10] John M. Walsh, Melvin H. Rice, Robert G. McQueen, and Frederick L. Yarger. Shock-wave compressions of twenty-seven metals. Equations of state of metals. *Physical Review*, 108(2), 1957. 2

[11] L. M. Barker and R. E. Hollenbach. Laser interferometer for measuring high velocities of any reflecting surface. *Journal of Applied Physics*, 43(11):4669–4675, 1972. 2, 67

[12] Quintin Johnson, Arthur Mitchell, and L. Evans. X-ray Diffraction Evidence for Crystalline Order and Isotropic Compression during the Shock-wave Process. *Nature*, 231:310 – 311, 1971. 3, 51

[13] Quintin Johnson, Arthur C. Mitchell, and L. Evans. X-ray diffraction study of single crystals undergoing shock-wave compression. *Applied Physics Letters*, 21(1):29–30, 1972. 3

[14] J. S. Wark, R. R. Whitlock, A. Hauer, J. E. Swain, and P. J. Solone. Shock launching in silicon studied with use of pulsed x-ray diffraction. *Physical Review B*, 35(17):9391–9394, 1987. 3, 51

[15] Justin S. Wark, Robert R. Whitlock, Allan A. Hauer, James E. Swain, and Paul J. Salone. Subnanosecond x-ray diffraction from laser-shocked crystals. *Physical Review B*, 40(8):5705–5714, 1989. 3, 93

[16] M. A. Mogilevskii, V. V. Efremov, and I. O. Mynkin. Crystalline lattice behaviour under strong one-dimensional compression. *Combustion, Explosion and Shock Waves*, 13(5):637–640, 1977. 3

[17] B. L. Holian. Atomistic computer simulations of shock waves. *Shock Waves*, 5(3):149–157, 1995. 3

[18] E. Orowan. Problems of plastic gliding. *Proceedings of the Physical Society*, 52(1):8–22, 1940. 4, 18, 22

[19] W. J. Murphy, A. Higginbotham, G. Kimminau, B. Barbrel, E. M. Bringa, J. Hawreliak, R. Kodama, M. Koenig, W. McBarron, M. A. Meyers, B. Nagler, N. Ozaki, N. Park, B. Remington, S. Rothman, S. M. Vinko, T. Whitcher, and J. S. Wark. The strength of single crystal copper under uniaxial shock compression at 100 GPa. *Journal of Physics: Condensed Matter*, 22(6):065404, 2010. 4, 98

[20] Stefan J. Turneaure and Y. M. Gupta. Real-time microstructure of shock-compressed single crystals from X-ray diffraction line profiles. *Journal of Applied Crystallography*, 44(3):574–584, 2011. 4

[21] Stefan J. Turneaure, Y. M. Gupta, K. Zimmerman, K. Perkins, C. S. Yoo, and G. Shen. Real-time microstructure of shocked LiF crystals: Use of synchrotron x-rays. *Journal of Applied Physics*, 105(5):053520, 2009. 4

[22] Matthew Suggit, Giles Kimminau, James Hawreliak, Bruce Remington, Nigel Park, and Justin Wark. Nanosecond x-ray Laue diffraction apparatus suitable for laser shock compression experiments. *Review of Scientific Instruments*, 81(8):083902, 2010. 4, 52, 63

[23] Matthew J. Suggit, Andrew Higginbotham, James A. Hawreliak, Gabriele Mogni, Giles Kimminau, Patrick Dunne, Andrew J. Comley, Nigel Park, Bruce A. Remington, and Justin S. Wark. Nanosecond white-light Laue diffraction measurements of dislocation microstructure in shock-compressed single-crystal copper. *Nature communications*, 3:1224, 2012. 5, 65, 112, 113, 115

[24] B. E. Warren. *X-ray Diffraction*. Dover, New York, 1969. 6, 35, 52, 100

[25] G. I. Taylor. The mechanism of plastic deformation of crystals. Part I. Theoretical. *Proceedings of the Royal Society of London A*, 145:362–387, 1934. 18

[26] D. Hull and D. J. Bacon. *Introduction to Dislocations*. Butterworth-Heinemann, 4 edition, 2001. 19, 21, 22

[27] Anthony Kelly and Kevin M. Knowles. Glide and Texture. In *Crystallography and Crystal Defects*. John Wiley & Sons, Ltd, 2nd edition, 2012. 22, 24, 114, 120, 146

[28] J. W. Christian and S. Mahajan. Deformation Twinning. *Progress in Materials Science*, 39:1–157, 1995. 25, 134

[29] C. G. Darwin. The theory of X-ray reflexion. *Philosophical Magazine*, 6:315–333, 1914. 32

[30] P.P. Ewald. Zur Begründung der Kristalloptik; Teil I: Dispersionstheorie. *Ann. Phys.*, 49(1):117, 1916. 32

[31] Matthew S. Schneider, Bimal Kad, Daniel H. Kalantar, Bruce A. Remington, Edward Kenik, H. Jarmakani, and Marc A. Meyers. Laser shock compression of copper and copper-aluminum alloys. *International Journal of Impact Engineering*, 32:473–507, 2005. 33

[32] Marc A. Meyers. *Dynamic Behavior of Materials*. Wiley, New York, 1994. 36

[33] P. H. Hugoniot. Mémoire sur la propagation des mouvements dans les corps et spécialement dans les gaz parfaits (deuxième partie). *Journal de L'Ecole Polytechnique*, 59:1–125, 1889. 38

[34] M. H. Rice, R. G. McQueen, and J. M. Walsh. Compression of Solids by Strong Shock Waves. In *Solid State Physics, Vol 6*, pages 1–63. 1958. 39, 73

[35] W. C. Davis. Shock waves; rarefaction waves; equation of state. In J. A. Zukas and W. P. Walters, editors, *Explosive Effects and Applications*, pages 47–113. Springer, New York, 1998. 39

[36] R. A. Graham. *Solids under High-Pressure Shock Compression: Mechanics, Physics and Chemistry*. Springer, New York, 1993. 42

[37] C.S. Smith. Metallographic studies of metals after explosive shock. *Transactions of the Metallurgical Society of A.I.M.E.*, 212:574–89, 1958. 43

[38] E. Hornbogen. Shock-induced dislocations. *Acta Metallurgica*, 10:978–980, 1962. 43

[39] M. A. Meyers, H. Jarmakani, E. M. Bringa, and B. A. Remington. Dislocations in Shock Compression and Release. In *Dislocations in Solids*, volume 15, chapter 89, pages 91–197. Elsevier, 2009. 44

[40] M. A. Meyers. A Model for Dislocation Generation in Shock-wave Deformation. *Scripta Metallurgica*, 12(1):21 – 26, 1978. 43

[41] H. Gao, Y. Huang, A. J. Rosakis, and P. Gumbsch. On radiation-free transonic motion of cracks and dislocations. *Journal of the Mechanics and Physics of Solids*, 47(9):1941–1961, 1999. 44

[42] E. Zaretsky. Dislocation multiplication behind the shock front. *Journal of Applied Physics*, 78(6):3740–3747, 1995. 44

[43] M. A. Meyers, F. Gregori, B. K. Kad, M. S. Schneider, D. H. Kalantar, B. A. Remington, G. Ravichandran, T. Boehly, and J. S. Wark. Laser-induced shock compression of monocrystalline copper: characterization and analysis. *Acta Materialia*, 51(5):1211–1228, 2003. 44, 98

[44] B. J. Alder. Computer Dynamics. *Annual Review of Physical Chemistry*, 24(1):325–337, 1973. 45

[45] John A. White. Lennard-Jones as a model for argon and test of extended renormalization group calculations. *The Journal of Chemical Physics*, 111(20):9352, 1999. 47

[46] Murray S. Daw and M. I. Baskes. Semiempirical, quantum mechanical calculation of hydrogen embrittlement in metals. *Physical Review Letters*, 50(17):1285–1288, 1983. 47

[47] Y. Mishin, M. J. Mehl, D. A. Papaconstantopoulos, A. F. Voter, and J. D Kress. Structural stability and lattice defects in copper: *Ab initio*, tight-binding, and embedded-atom calculations. *Physical Review B*, 63(22):224106, 2001. 48, 109

[48] X. D. Dai, Y. Kong, J. H. Li, and B. X. Liu. Extended Finnis-Sinclair potential for bcc and fcc metals and alloys. *Journal of Physics: Condensed Matter*, 18(19):4527–4542, 2006. 48, 122

[49] Steve Plimpton. Fast Parallel Algorithms for Short-Range Molecular Dynamics. *Journal of Computational Physics*, 117(1):1–19, 1995. 48

[50] Loup Verlet. Computer "experiments" on classical fluids. I. Thermodynamical properties of Lennard-Jones molecules. *Physical Review*, 159(1):98–103, 1967. 48

[51] C. L. Kelchner, S. J. Plimpton, and J. C. Hamilton. Dislocation nucleation and defect structure during surface indentation. *Physical Review B*, 58(17):11085–11088, 1998. 50

[52] Giles Kimminau, Bob Nagler, Andrew Higginbotham, William J. Murphy, Nigel Park, James Hawreliak, Kai Kadau, Timothy C. Germann, Eduardo M. Bringa, Daniel H. Kalantar, Hector E. Lorenzana, Bruce A. Remington, and Justin S. Wark. Simulating picosecond x-ray diffraction from shocked crystals using post-processing molecular dynamics calculations. *Journal of Physics: Condensed Matter*, 20(50):505203, 2008. 50, 81

[53] P. A. Rigg and Y. M. Gupta. Real-time x-ray diffraction to examine elastic plastic deformation in shocked lithium fluoride crystals. *Applied Physics Letters*, 73(12):1655–1657, 1998. 51

[54] Daniel H. Kalantar, E. Bringa, M. Caturla, J. Colvin, K. T. Lorenz, M. Kumar, J. Stölken, A. M. Allen, K. Rosolankova, J. S. Wark, M. A. Meyers, M. Schneider, and T. R. Boehly. Multiple film plane diagnostic for shocked lattice measurements (invited). *Review of Scientific Instruments*, 74(3):1929–1934, 2003. 51, 52, 54

[55] James Hawreliak, Martin Butterfield, Huw Davies, Bassem El-Dasher, Andrew Higginbotham, Daniel Kalantar, Giles Kimminau, James McNaney, Despina Milathianaki, William Murphy, Bob Nagler, Nigel Park, Bruce Remington, Lee Thorton, Thomas Whitcher, Justin Wark, and Hector

Lorenzana. *In-situ* probing of lattice response in shock compressed materials using x-ray diffraction. *AIP Conference Proceedings*, 955:1327–1332, 2007. 51

[56] J. Hawreliak, H. E. Lorenzana, B. A. Remington, S. Lukezic, and J. S. Wark. Nanosecond x-ray diffraction from polycrystalline and amorphous materials in a pinhole camera geometry suitable for laser shock compression experiments. *The Review of Scientific Instruments*, 78(8):083908, 2007. 52, 54, 62

[57] Kouhei Ichiyanagi, Shin-ichi Adachi, Shunsuke Nozawa, Yoichiro Hironaka, Kazutaka G. Nakamura, Tokushi Sato, Ayana Tomita, and Shin-ya Koshihara. Shock-induced lattice deformation of CdS single crystal by nanosecond time-resolved Laue diffraction. *Applied Physics Letters*, 91(23):231918, 2007. 52

[58] M. S. Paterson. X-Ray Diffraction by Face-Centered Cubic Crystals with Deformation Faults. *Journal of Applied Physics*, 23(8):805–811, 1952. 52

[59] P. Ehrhart, H. Trinkaus, and B. Larson. Diffuse scattering from dislocation loops. *Physical Review B*, 25(2):834–848, 1982. 52

[60] R. I. Barabash, G. E. Ice, B. C. Larson, and Wenge Yang. Application of white x-ray microbeams for the analysis of dislocation structures. *Review of Scientific Instruments*, 73(3):1652–1654, 2002. 52

[61] R. I. Barabash, G. E. Ice, and J. W. L. Pang. Gradients of geometrically necessary dislocations from white beam microdiffraction. *Materials Science and Engineering A*, 400-401:125–131, 2005. 52

[62] Giles Kimminau. *Studies of Shock-Induced Plasticity by use of Molecular Dynamics and X-ray Diffraction*. D.Phil, University of Oxford, 2009. 52, 56

[63] A. Loveridge-Smith, A. Allen, J. Belak, T. Boehly, A. Hauer, B. Holian, D. Kalantar, G. Kyrala, R. W. Lee, P. Lomdahl, M. A. Meyers, D. Paisley, S. Pollaine, B. Remington, D. C. Swift, S. Weber, and J. S. Wark. Anomalous Elastic Response of Silicon to Uniaxial Shock Compression on Nanosecond Time Scales. *Physical Review Letters*, 86(11):2349–2352, 2001. 54, 93

[64] D. W. Phillion and C. J. Hailey. Brightness and duration of x-ray line sources irradiated with intense 0.53-μm laser light at 60 and 120 ps pulse width. *Physical Review A*, 34(6):4886–4896, 1986. 54, 85

[65] I. J. Paterson, R. J. Clarke, N. C. Woolsey, and G. Gregori. Image plate response for conditions relevant to laser-plasma interaction experiments. *Measurement Science and Technology*, 19(9):095301, 2008. 61

[66] B. R. Maddox, H. S. Park, B. A. Remington, N. Izumi, S. Chen, C. Chen, G. Kimminau, Z Ali, M. J. Haugh, and Q. Ma. High-energy x-ray backlighter spectrum measurements using calibrated image plates. *Review of Scientific Instruments*, 82(2):023111, 2011. 61, 91

[67] James A. Hawreliak, Bassem El-Dasher, Hector Lorenzana, Giles Kimminau, Andrew Higginbotham, Bob Nagler, Sam M. Vinko, William J. Murphy, Thomas Whitcher, Justin S. Wark, Steve Rothman, and Nigel Park. *In situ* x-ray diffraction measurements of the c/a ratio in the high-pressure ϵ phase of shock-compressed polycrystalline iron. *Physical Review B*, 83(14):144114, 2011. 62, 121

[68] N. L. Coleburn. Compressibility of Pyrolytic Graphite. *The Journal of Chemical Physics*, 40(1):71, 1964. 67

[69] D. G. Doran. Hugoniot Equation of State of Pyrolytic Graphite to 300 kbars. *Journal of Applied Physics*, 34(4):844–851, 1963. 67

[70] L. M. Barker and R. E Hollenbach. Shock-Wave Studies of PMMA, Fused Silica, and Sapphire. *Journal of Applied Physics*, 41(10):4208–4226, 1970. 67

[71] Willard F. Hemsing. Velocity sensing interferometer (VISAR) modification. *Review of Scientific Instruments*, 50(1):73–78, 1979. 67

[72] D. R. Goosman. Analysis of the laser velocity interferometer. *Journal of Applied Physics*, 46(8):3516, 1975. 67

[73] Daniel H. Dolan. Foundations of VISAR analysis. Technical report, Sandia National Laboratories, 2006. 67

[74] P. M. Celliers, D. K. Bradley, G. W. Collins, D. G. Hicks, T. R. Boehly, and W. J. Armstrong. Line-imaging velocimeter for shock diagnostics at the OMEGA laser facility. *Review of scientific instruments*, 75(11):4916–4929, 2004. 67, 70, 73

[75] L. M. Barker and K. W. Schuler. Correction to the velocity-per-fringe relationship for the VISAR interferometer. *Journal of Applied Physics*, 45(8):3692–3693, 1974. 69, 70

[76] Claude Roddier and François Roddier. Interferogram analysis using Fourier transform techniques. *Applied Optics*, 26(9):1668, 1987. 73

[77] Jerry Wackerle and H. L. Stacy. Refractive Index of Shocked Alkali Halides. In S.C. Schmidt and N.C. Holmes, editors, *Shock Waves in Condensed Matter*, pages 699–702. Elsevier, 1988. 73

[78] Jerry Wackerle and H. L. Stacy. Shock-induced Heating, Phase Transitions, and Opacity in Alkali Halides. In S.C. Schmidt, J.N. Johnson, and L.W. Davison, editors, *Shock Waves in Condensed Matter 1989*, pages 151–154. Elsevier, 1990. 73

[79] Gerald I Kerley. Calculation of Release Adiabats and Shock Impedance Matching A Kerley Technical Services Research Report. Technical Report March, 2008. 75

[80] A. Sollier, V. Bouyer, J.-B. Maillet, and C. Voltz. A high-explosive driven experiment to compare the reflected Hugoniot and the release adiabat curves of Ti-6Al-4V alloy from a 52 GPa shock state. *DYMAT International Conferences*, pages 207–211, 2009. 75

[81] P. M. Celliers, G. W. Collins, D. G. Hicks, and J. H. Eggert. Systematic uncertainties in shock-wave impedance-match analysis and the high-pressure equation of state of Al. *Journal of Applied Physics*, 98(11):113529, 2005. 75

[82] Andrew Higginbotham. *Shock Induced Phase Transitions In Iron: Studies via EXAFS and X-ray Diffraction.* D.Phil, University of Oxford, 2009. 81

[83] Yu. Ralchenko, A.E. Kramida, J. Reader, and NIST ASD Team. NIST Atomic Spectra Database (version 3.1.5), 2010. 85

[84] L. E. Ruggles, J. L. Porter, P. K. Rambo, W. W. Simpson, M. F. Vargas, G. R. Bennett, and I. C. Smith. Measurements of 4-10 keV x-ray production with the Z-Beamlet laser. *Review of Scientific Instruments*, 74(3):2206–2210, 2003. 85

[85] E. V. Aglitsky, E. Ya Golts, Yu. A Levykin, and A. M. Livshits. X-ray spectra of Ne-like ions of Ag, Cd, In and Sn. *Journal of Physics B: Atomic, Molecular and Optical Physics*, 14:1549–1552, 1981. 85

[86] C. Back, J. Grun, C. Decker, L. J. Suter, J. Davis, O. L. Landen, R. Wallace, W. W. Hsing, J. M Laming, U. Feldman, M. C. Miller, and C. Wuest. Efficient Multi-keV Underdense Laser-Produced Plasma Radiators. *Physical Review Letters*, 87(27):275003, 2001. 85

[87] K. M. Glibert, J. P. Anthes, M. A. Gusinow, M. A. Palmer, R. R. Whitlock, and D. J. Nagel. X-ray yields of plasmas heated by 8-nsec neodymium laser pulses. *Journal of Applied Physics*, 51(3):1449–1451, 1980. 88

[88] R. Kodama, T. Mochizuki, K. A. Tanaka, and C. Yamanaka. Enhancement of keV x-ray emission in laser-produced plasmas by a weak prepulse laser. *Applied Physics Letters*, 50(12):720, 1987. 88

[89] Paul A. Keiter, Andrew Comely, John Morton, Heidi Tierney, Jonathan Workman, and Mark Taylor. Conversion efficiency of high-Z backlighter materials. *The Review of scientific instruments*, 79(10):10E918, 2008. 88

[90] B. Yaakobi, T. Boehly, D. Meyerhofer, T. Collins, B. Remington, P. Allen, S. Pollaine, H. Lorenzana, and J. Eggert. EXAFS Measurement of Iron bcc-to-hcp Phase Transformation in Nanosecond-Laser Shocks. *Physical Review Letters*, 95(7):1–4, 2005. 92

[91] B. L. Henke, E. M. Gullikson, and J. C. Davis. X-ray Interactions: Photoabsorption, Scattering, Transmission, and Reflection at E= 50-30,000 eV, Z= 1-92. *Atomic data and nuclear data tables*, 54:181–342, 1993. 93

[92] W. H. Gust and E. B. Royce. Axial Yield Strengths and Two Successive Phase Transition Stresses for Crystalline Silicon. *Journal of Applied Physics*, 42(5):1897–1905, 1971. 93, 96, 97

[93] Tsuneaki Goto, Toshiyuki Sato, and Yasuhiko Syono. Reduction of Shear Strength and Phase-Transition in Shock-Loaded Silicon. *Japanese Journal of Applied Physics*, 21(6):pp. L369–L371, 1982. 93, 97

[94] Stefan J. Turneaure and Y. M. Gupta. X-ray diffraction and continuum measurements in silicon crystals shocked below the elastic limit. *Applied Physics Letters*, 90(5):051905, 2007. 93

[95] Buyang Cao, David H. Lassila, Chongxiang Huang, Yongbo Xu, and Marc André Meyers. Shock compression of monocrystalline copper: Experiments, characterization, and analysis. *Materials Science and Engineering: A*, 527(3):424–434, 2010. 98

[96] E. M. Bringa, K. Rosolankova, R. E. Rudd, B. A. Remington, J. S. Wark, M. Duchaineau, D. H. Kalantar, J. Hawreliak, and J. Belak. Shock deformation of face-centred-cubic metals on subnanosecond timescales. *Nature Materials*, 5:805–809, 2006. 98, 99, 117

[97] L. E. Murr. Work hardening and the pressure dependence of dislocation density and arrangements in shock loaded nickel and copper. *Scripta Metallurgica*, 12:201–206, 1978. 98

[98] Timothy C. Germann, Döme Tanguy, Brad Lee Holian, Peter S. Lomdahl, Michel Mareschal, and Ramon Ravelo. Dislocation Structure behind a Shock Front in Fcc Perfect Crystals: Atomistic Simulation Results. *Metallurgical and Materials Transactions A*, 35(9):2609–2615, 2004. 99

[99] L. Velterop, R. Delhez, Th. H. de Keijser, E. J. Mittemeijer, and D Reefman. X-ray diffraction analysis of stacking and twin faults in f.c.c. metals: a revision and allowance for texture and non-uniform fault probabilities. *Journal of Applied Crystallography*, 33:296–306, 2000. 100

[100] John Lindl. Development of the indirect-drive approach to inertial confinement fusion and the target physics basis for ignition and gain. *Physics of Plasmas*, 2(11):3933–4024, 1995. 101, 102

[101] O. E. Jones and J. D. Mote. Shock-Induced Dynamic Yielding in Copper Single Crystals. *Journal of Applied Physics*, 40(12):4920–4928, 1969. 102

[102] Katarina K. Rosolankova. *Picosecond X-ray Diffraction from Shock-Compressed Metals: Experiments and Computational Analysis of Molecular Dynamics Simulations*. D.Phil, University of Oxford, 2005. 109

[103] W. F. Hosford. On Orientation Changes Accompanying Slip and Twinning. *Texture of Crystalline Solids*, 2(3):175–182, 1977. 109, 114

[104] E. Zaretsky. Multipeak pulse x-ray diffraction study of shocked single crystals. *Journal of Applied Physics*, 93(5):2496–2506, 2003. 114, 115

[105] A. H. Shalaby and K. S. Havner. A general kinematical analysis of double slip. *Journal of the Mechanics and Physics of Solids*, 26(2):79–92, 1978. 116

[106] E. Loomis, P. Peralta, D. Swift, C. H. Lim, R. Dickerson, and P. Dickerson. Cross-sectional TEM studies of plastic wave attenuation in shock loaded NiAl. *Materials Science and Engineering: A*, 437(2):212–221, 2006. 116

[107] Mutasem Shehadeh. Modeling Shock Induced Plasticity in Copper Single Crystal: Numerical and Strain Localization Issues. *Advanced Materials Research*, 324:193–196, 2011. 116

[108] Mutasem A. Shehadeh. Multiscale dislocation dynamics simulations of shock-induced plasticity in small volumes. *Philosophical Magazine*, 92(10):1173–1197, 2012. 116

[109] D. K. Bowen and J. W. Christian. The calculation of shear stress and shear strain for double glide in tension and compression. *Philosophical Magazine*, 12(116):369–378, 1965. 116, 146

[110] J. W. Swegle and D. E. Grady. Shock viscosity and the prediction of shock wave rise times. *Journal of Applied Physics*, 58(2):692–701, 1985. 117

[111] K. Rosolankova, J. S. Wark, E. M. Bringa, and J. Hawreliak. Measuring stacking fault densities in shock-compressed FCC crystals using *in situ* x-ray diffraction. *Journal of Physics: Condensed Matter*, 18(29):6749–6757, 2006. 117

[112] Buyang Cao, Eduardo M. Bringa, and Marc André Meyers. Shock Compression of Monocrystalline Copper: Atomistic Simulations. *Metallurgical and Materials Transactions A*, 38(11):2681–2688, 2007. 117

[113] J. Hawreliak, J. D. Colvin, J. H. Eggert, D. H. Kalantar, H. E. Lorenzana, J. S. Stölken, H. M. Davies, T. C. Germann, B. L. Holian, K. Kadau, P. S. Lomdahl, A. Higginbotham, K. Rosolankova, J. Sheppard, and J. S. Wark. Analysis of the x-ray diffraction signal for the α-ϵ transition in shock-compressed iron: Simulation and experiment. *Physical Review B*, 74(18):184107, 2006. 120

[114] A. J. Comley, B. R. Maddox, R. E. Rudd, S. T. Prisbrey, J. A. Hawreliak, D. A. Orlikowski, S. C. Peterson, J. H. Satcher, A. J. Elsholz, H.-S. Park, B. A. Remington, N. Bazin, J. M. Foster, P. Graham, N. Park, P. A. Rosen, S. R. Rothman, A. Higginbotham, M. Suggit, and J. S. Wark. Strength of Shock-Loaded Single-Crystal Tantalum Determined using *In-Situ* Broadband X-ray Laue Diffraction. *Physical Review Letters*, 110(11):115501, 2013. 121, 140

[115] J. M. McNaney, L. M. Hsiung, N. R. Barton, and M Kumar. Shock Driven Twinning in Tantalum Single Crystals. *AIP Conference Proceedings*, 1195:1127–1130, 2009. 121

[116] L. M. Hsiung and D. H. Lassila. Shock-induced deformation twinning and omega transformation in tantalum and tantalum-tungsten alloys. *Acta Materialia*, 48:4851–4865, 2000. 121, 130

[117] J. A. Moriarty, L. X. Benedict, J. N. Glosli, R. Q. Hood, D. A. Orlikowski, M. V. Patel, P. Soderlind, F. H. Streitz, M. Tang, and L. H. Yang. Quantum-based atomistic simulation of materials properties in transition metals. *Journal of Physics: Condensed Matter*, 14:2825, 2002. 122

[118] R. G. McQueen and S. P. Marsh. GMX-6-566. Technical report, Los Alamos Science Laboratory, 1964. 123, 124

[119] A. C. Mitchell and W. J. Nellis. Shock compression of aluminum, copper, and tantalum. *Journal of Applied Physics*, 52(5):3363–3374, 1981. 123, 124

[120] R. F. Zhang, J. Wang, I. J. Beyerlein, and T. C. Germann. Twinning in bcc metals under shock loading: a challenge to empirical potentials. *Philosophical Magazine Letters*, 91(12):731–740, 2011. 130